A 3D Glacial Isostatic Adjustment model for Northwestern Europe

R.A.C.M. van Casteren

TUDelft

A 3D Glacial Isostatic Adjustment model for Northwestern Europe

by

R.A.C.M. van Casteren

to partially obtain the degree of Master of Science
at the Delft University of Technology,
to be defended on July 26th, 2019 at 10:00 AM.

Student number: 4215966
Thesis committee: Prof. Dr. Ir. P.N.A.M. Visser,   TU Delft, chair
                    Dr. Ir. W. van der Wal,   TU Delft, supervisor
                    Dr. Ir. H. van der Marel,   TU Delft

TU Delft

Preface

Through this thesis, I conclude my time as an aerospace engineering student at Delft University of Technology. Ever since I can remember, I have been fascinated by the workings of the universe: according to my parents my first ever word was "Moon". As such, it is no wonder I elected to specialise in space exploration, and interplanetary sciences in particular. I have thoroughly enjoyed gaining a better understanding of our Earth, and have grown more passionate about finding ways to protect our only home from excessive human interference. I hope this work adds to the understanding of the dynamics of the Earth, in the past, present and future to come.

First off, I would like to thank my supervisor Wouter van der Wal for his guidance and advice. Our regular meetings have helped me in keeping on track, and in realising the scientific potential of my work at times when I felt like I had not even started "doing science" yet. And while I formally only had one daily supervisor, a big word of thanks goes out to PhD candidate Bas Blank. Thank you for your patience and help in understanding your model and glacial isostatic adjustment in general. Additionally, I highly appreciate the contributions of Marc Hijma, Sarah Bradley, and Norman Teferle to this research. I thank you for sharing your own data, insights, and feedback.

Next, I would like to thank my fellow MSc flex-room occupants for their support. I feel like a part of our own little thesis-community, and highly value the time we spent discussing each others work. I am especially grateful for the help of Maaike, and I am sure that our combined efforts will eventually materialise into a most comprehensive GIA model.

To conclude, I would like to express my sincere gratitude towards my family and friends. I thank my parents for their unconditional love and support. My siblings I thank for putting up with me. I wish you both all the best, and hope you'll have as least as much fun during your studies as I have had during mine. I would not have been able to do so without all the people I have met over the last seven years. Lastly, I would like to thank Martijn and our very cute cat Toulouse for sharing my highs and lows during this project.

Rosalie van Casteren
Delft, June, 2019

Summary

The Earth is subjected to 100,000 year cycles of glaciation and deglaciation. The deformations induced by glacial and oceanic loading and the continuous attempt at recovery of the isostatic equilibrium within the solid Earth, are referred to as Glacial Isostatic Adjustment (GIA). This process is ongoing still and yields a large contribution to present day surface deformation and sea level change in formerly glaciated areas. In order to accurately model GIA, the lateral viscosity variations within the interior of the Earth are accounted for (Kaufmann et al., 2000; Steffen et al., 2006; Wu and van der Wal, 2003). Additionally, an increased level of accuracy is obtained by adopting a combination of linear and non-linear viscoelasticity as demonstrated by Barnhoorn et al. (2011); Forno and Gasperini (2007); van der Wal et al. (2013); Wu and Wang (2008).

During the Last Glacial Maximum, the British-Irish and Fennoscandian Ice Sheets covered large parts of Northwestern Europe. The interior of the Earth in this area is known to consist of material of very heterogeneous tectonic origin (Artemieva et al., 2006). Additionally, research in this area is promoted by the availability of the independent regional ice model Bradley2018 (Bradley, personal communication), an RSL observation database for the Rhine-Meuse Delta (Hijma and Cohen, 2019), and a collection of GPS derived uplift rates throughout Europe (Teferle, personal communication).

At the Astrodynamics and Space Missions research group of Delft University of Technology, a 3D GIA FEM model has been developed to model GIA in Antarctica (Blank et al., 2017). This model follows the work by Wu (2004) and van der Wal et al. (2013), and is complemented with an iterative algorithm to solve the sea level equation in accordance with Kendall et al. (2005). This research aims to provide a single GIA model best suited for the prediction of GIA induced vertical surface deformation in Northwestern Europe, by adapting the existing model. In doing so, a better understanding of the interior of the Earth in Northwestern Europe can be achieved.

The response of the Earth is dictated by the composite rheology creep flow laws for olivine (Hirth and Kohlstedt, 2003). By varying the grain size as well as the water content of the mantle material, and by implementing a global temperature model of the Earth's interior, four 3D composite rheology Earth models are obtained. The fifth Earth model considered is the radially symmetric VM5a viscosity profile developed by Peltier et al. (2015) in conjunction with the global ice model ICE-6G_C. The performance of all five Earth model configurations in combination with both the ICE-6G_C model and the Bradley2018 model is analysed in terms of relative sea level and uplift rates.

It is found that the Bradley2018 model is the preferred ice model for GIA modelling in Northwestern Europe. The ICE-6G_C model outperforms the Bradley2018 model at far-field RSL sites, which is attributed to its superior representation of global eustatic sea level rise. The 3D composite rheologies lead to improved fits to RSL observations for the majority of the investigated measurement sites compared to the 1D scenario. The dry 4 mm grain size rheology yields the best overall performance out of all rheological configurations considered. A preference towards wet rheology exists in regions of Sveco-Norwegian tectonic origin. The strongest rheology is preferred in the mid-west of Scotland. No definitive connection is found between the local tectonic origin and preferred rheology from RSL simulations. It is believed that this analysis may benefit from the inclusion of laterally varying grain sizes and water content inferred from geophysical observations, as well as the extension of the variable space for the water content.

For both ice models, an improved fit to observed uplift rates can be obtained through the application of a 3D composite rheology. The GPS derived uplift rates can be reproduced best using the dry 10 mm grain size rheology in combination with the Bradley2018 ice history. This model is deemed to be best suited for simulation of GIA induced uplift rates in Northwestern Europe. The second best performance in terms of uplift rate is found using the 1D Earth model. In Scandinavia the 4 mm dry rheology yields uplift rates equal to roughly half the observed uplift rates, while the uplift rates for the 10 mm and 4 mm wet rheologies are near-zero. In the far-field, where other surface deformation mechanisms may infer a larger deformation rate than GIA (Fokker et al., 2018), no model could reproduce the observed uplift rates.

The presence of a high viscosity anomaly beneath Eastern Fennoscandia is captured by the 3D rheologies and results in a shift of the centre of positive and negative uplift rates. As the spatial distribution of minima and maxima in both uplift rates and RSL change rates is sensitive to the inclusion of a 3D rheology, this should be accounted for in future regional sea level change and surface deformation projections.

List of Abbreviations

List of Figures

ix

List of Tables

Contents

<div style="text-align: right; font-size: 3em;">1</div>

Introduction

In this chapter, an introduction on Glacial Isostatic Adjustment in Northwestern Europe is provided. To this extent, the most recent episode of global periodic glaciation and deglaciation is detailed in section 1.1. Next, a definition of Glacial Isostatic Adjustment is provided in section 1.2. In section 1.3, the selection of Northwestern Europe as a focus area of this study is explained. Next, an insight is provided into the existing body of work on the inclusion of 3D viscosity and a composite rheology in GIA modelling in section 1.4. The state-of-the-art model available within the research group that has successfully implemented a 3D composite rheology as well a realistic sea level module is discussed in section 1.5. The aim and research questions arising from the status quo in GIA modelling in Northwestern Europe are introduced in section 1.6. This chapter concludes with an outline of the remainder of the report in section 1.7.

1.1. The latest glacial cycle

The Earth has been subjected to periodic glaciation and deglaciation throughout the most recent geological period. This period is referred to as the Quaternary, and spans from roughly 2.6 million years ago to the present day. The pacing of each of the Quaternary glacial cycles can be attributed to changes in the Earth's orbital configuration (Maslin, 2016). The combined effects of these changes in eccentricity, obliquity, and precession, are captured by so-called Milankovitch cycles. The 8 most recent glaciation cycles adhere to a 100,000 year periodicity. During the latest cycle, the maximum ice volume was attained approximately 21,000 years ago, or 21 kilo annum (ka) before present (BP). This moment in time is known as the Last Glacial Maximum, or LGM (Whitehouse, 2018).

The LGM has been preceded by nearly 90,000 years of steady glaciation. The deglaciation, conversely, took place within circa 10,000 years after the LGM. Due to this rapid melting process, a significant global rise in sea level was attained, believed to amount to approximately 130 m (Whitehouse, 2018).

1.2. Glacial Isostatic Adjustment

As the loading of the Earth's surface changes over time, the Earth deforms. The deformations induced by glacial and oceanic loading and the continuous attempt at recovery of the isostatic equilibrium, is called Glacial Isostatic Adjustment (GIA). Here isostasy refers to the buoyancy of the crust on the mantle, which is dependent on the crust's density profile and thickness.

The resulting deformation of the Earth during loading and unloading, is displayed in figures 1.1a and 1.1b respectively. The presence of water in either a liquid or solid state introduces a loading of the Earth's surface. Here it can be seen how material in the mantle during loading is pushed away, resulting in subsidence of the crust beneath the ice sheets and the creation of a peripheral forebulge outside the margins of the ice sheet. Once the ice sheet melts, global sea-levels rise due to meltwater. The forebulges collapses and previously ice covered areas experience crustal uplift.

GIA is governed by both the spatial and temporal evolution of the surface loads as well as by the internal characteristics of the crust and mantle such as thickness and viscosity. It is important to understand that the redistribution of melted ice over the Earth is not uniform. This is due to the continuous change of the shape of the geoid, which dictates the distribution of water. Though most ice sheets that were present during the LGM have melted since, the isostatic deformation of the Earth is an ongoing process still.

<div style="text-align: center;">1</div>

Given the relaxation time of the mantle, the Earth's GIA response would require multiple tens of thousands of years to reach isostatic equilibrium. This equilibrium is however never reached. Since the glaciation time significantly exceeds the rapid deglaciation at the end of a glacial cycle, newly applied glacial loads of the next glacial cycle disturb the system once more. Therefore even today's observed deformation is the result of multiple glacial loading cycles of the Earth (Whitehouse, 2009).

(a) Growth of peripheral forebulge, subsidence of surface underneath glacial load.

(b) Subsidence of peripheral forebulge, uplift of surface underneath former ice sheet.
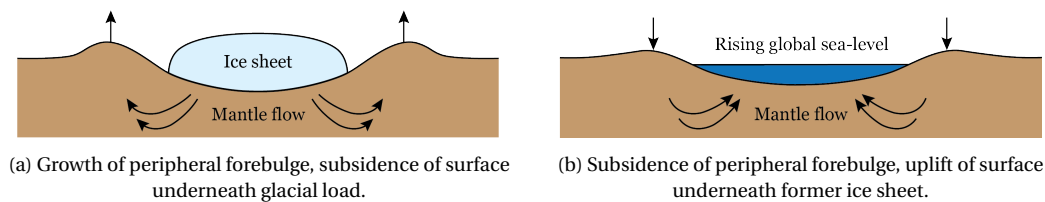
Figure 1.1: The response of the solid Earth to glacial loading and unloading. After Whitehouse (2009), figure 3.5.

The present day uplift of the Earth's surface can be measured using GPS, providing a record of some 20 years of uplift on a global scale. Different space-based techniques can also offer insights into the deformation of the Earth. The Gravity Recovery and Climate Experiment (GRACE) mission can provide mass flow data through gravimetric measurements of the Earth. These space-geodetic observables are however limited in temporal resolution, as such measurements are available for the last decades only. A commonly used way to asses both the change of ocean volume and change in shape of the geoid over the past 20,000 years, is through Relative Sea Level (RSL). This is a measure of the difference between the ocean-height and geoid-height. This type of data can be obtained from both tide gauges and dated geological or biological markers, the latter of which can lead to collections of data that go back to the LGM. The combination of both present-day uplift measurements and historic RSL observations allow for constraining GIA effects modelled for both the past and the present.

Glacial isostatic adjustment is however not the only deformation process that affects the rise and fall of land and sea. By modelling the GIA induced deformation of the Earth, GRACE observations can be filtered in order to investigate present day ice sheet mass loss or gain (van der Wal et al., 2015). Similarly, the contribution of other natural and anthropogenic deformation processes to local land rise and fall and sea level change and can be identified when knowing the contribution of GIA (Fokker et al., 2018). Aside from these two examples, GIA modelling can contribute to many other fields of study including but not limited to glaciology, climatology, geomorphology, and geodynamics (Whitehouse, 2018).

1.3. A focus on Northwestern Europe

In this research, Northwestern Europe, is defined to comprise of the geographic regions in close proximity to the North Sea, e.g. the British Isles, the Benelux, Germany and Fennoscandia. At LGM, three major ice sheets covered large parts of Northwestern-Europe and areas in its vicinity, being the British-Irish Ice Sheet (BIIS), Fennoscandian Ice Sheet (FIS), and Barents Sea Ice Sheet (BSIS). All three ice sheets are depicted in figure 1.2.

The implications of GIA in Northwestern Europe are still relevant today. This is especially true in coastal regions that are located at, or below, present day sea level, and are expected to subside rather than rise. The presence of not one, but two large and mostly separated ice sheets leads to a great interest in the modelling of vertical and horizontal deformation of the crust and changes in sea level in Northwestern Europe. Said process forms a major source of uncertainty in European sea-level rise projections (Grinsted et al., 2015). It is of significant interest to identify the contribution of this glacial process to land fall and rise in this area in general, which is affected by other deformations mechanism not discussed in this research (Fokker et al., 2018). Additionally, the analysis of past and present deformation and sea-level change enables a better understanding of both ice loading histories and oceanic loading, as well as the Earths interior. The lessons learnt in this specific region may also contribute to research performed in other regions or even on a global scale. The effects of GIA in specific parts of Northwestern Europe have been investigated previously, focusing on the Northwestern part of the European mainland (Vink et al., 2007), the British Isles (Bradley et al., 2011), and Fennoscandia respectively (Barnhoorn et al., 2011; van der Wal et al., 2013).

Aside from the interest into accurate GIA modelling for the densely populated Northwestern Europe, researching GIA in this region is promoted by the availability of a detailed regional ice sheet model and two databases of GIA constraints supplied through personal communication prior to publication. These constraints are captured in a collection of GPS derived uplift rates throughout Europe (Teferle, personal commu-
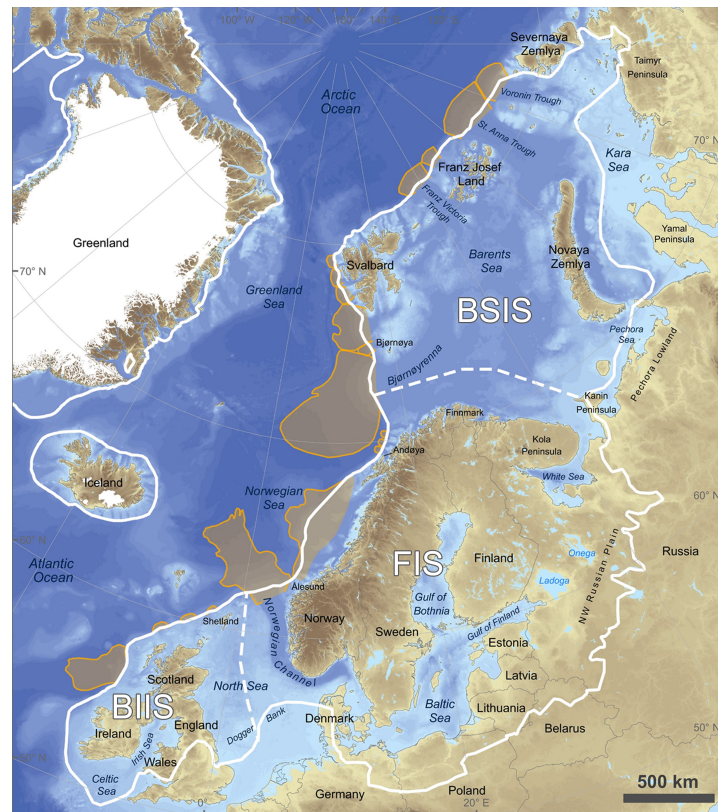
Figure 1.2: An overview of the maximum extent of the three major ice sheets, BIIS, FIS, and BSIS. The outer boundaries of the ice sheets are indicated with the white line, the approximate inner boundaries are indicated with the dashed white line. After Hughes et al. (2015), figure 1.

nication, 06/06/2018), and an RSL database focusing on the Dutch Rhine-Meuse Delta (Hijma and Cohen, 2019). The ice loading history for the European ice sheets, as developed by Bradley (personal communication, 2018), is mainly constraint by geomorphological and geochronical data. While often times global ice models as well as models of the Earth's interior are constraint using RSL observations, the model by Bradley is expected to suffer less from such a bias towards specific RSL constraints.

1.4. Three-dimensional non-linear viscoelasticity

While early research into GIA induced surface deformation relied on the assumption that the viscosity distribution of the Earth's interior is radially symmetric (Lambeck et al., 1998; Steffen and Kaufmann, 2005; Tushingham and Peltier, 1991), more recent efforts have focused on the inclusion of lateral viscosity variations (Ivins and Sammis, 1995; Kaufmann et al., 1997; Whitehouse et al., 2006; Wu and van der Wal, 2003). These flat-Earth and spherical-Earth based investigations into three-dimensional viscosities, concluded that the implementation of a laterally varying viscosity profile results in significantly altered GIA predictions than the more simple radially symmetric profiles. These observations justify the inclusion of 3D viscosity variations for accurate GIA modelling.

Aside from a simplified representation of the viscosity distribution of the Earth's mantle, a multitude of past studies on GIA have assumed a purely linear Maxwell rheology. Rheology is defined as the "study of the deformation and flow of matter" (Barnes et al., 1989). The linear Maxwell rheology is a combination of an elastic and a viscous component (Karato, 2012). Evidence however suggests that the GIA response of the solid Earth is not purely linear, but rather also includes a non-linear component. The combination of these two types of flow mechanisms, called composite rheology, is believed to provide a more accurate approximation of the solid Earth's behaviour when compared to models applying either linear or non-linear deformation mechanism individually (van der Wal et al., 2013). The flow laws and rheological parameters that are used to describe the relation between stress and strain of a non-linear, or power-law rheology, have been examined through experimental research by Hirth and Kohlstedt (2003).

It is believed that the inclusion of both lateral heterogeneity in Northwestern Europe is warranted due to its diverse tectonical origin (Artemieva et al., 2006). Accounting for such tectonical differences through the usage of seismically derived temperature inputs and a composite rheology, has shown to improve the performance of a GIA model for Fennoscandia with respect to a 1D scenario (van der Wal et al., 2013). Additionally, upper mantle viscosity modelling indicates that a composite rheology should be accounted for in Scandinavia (Barnhoorn et al., 2011). While this illustrates the importance of using a 3D composite rheology in GIA modelling of Fennoscandia, this approach has not yet been applied to Northwestern Europe as a whole.

1.5. The 3D GIA FEM model

The linearly viscoelastic GIA response of a radially symmetric solid Earth can be modelled using the spectral method (Martinec and Wolf, 2005). The inclusion of a 3D composite rheology can however only be achieved through numerical simulation. The usage of commercial finite element analysis packages is well suited for the modelling of GIA for a 3D Earth, as the viscoelastic characteristics of all elements can be determined individually (Wu, 2004).

Within the Astrodynamics and Space Missions research group at Delft University of Technology, a 3D GIA FEM model has been developed (Blank, to be published). This model includes an extensive sea level module that analyses the impact on the distribution of oceanic loads and its subsequent effect on deformation of the Earth. Using the commercially available Abaqus FEM software, the 3D GIA FEM model has initially been developed to model GIA in Antarctica. This research will add to the body of work related to this 3D GIA FEM model, by adapting it for the application of 3D composite rheologies in Northwestern Europe. Efforts are ongoing to adapt the model to account for both a laterally varying composite rheology and true polar wander simultaneously.

The two main inputs to the 3D GIA FEM model that will be used in this research, are the glacial surface loads and the characteristics of the solid Earth. A general conceptual overview of the 3D GIA FEM model developed by Blank (to be published), is included in figure 1.3.
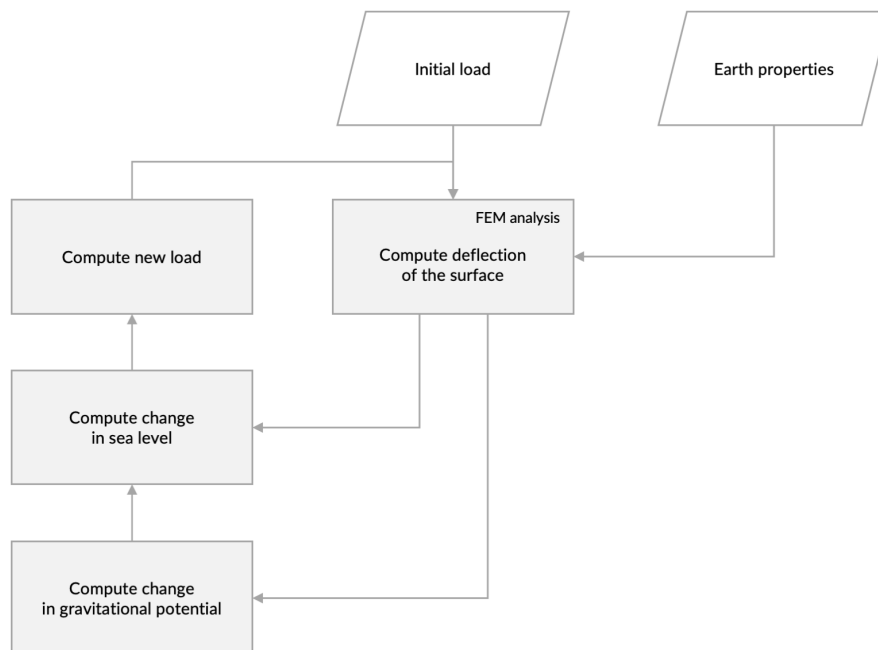
Figure 1.3: High-level overview of the 3D GIA FEM model used in this study, developed by Blank (personal communication).

1.6. Research questions

The goal of this research is two-fold. On the one hand, this research aims to provide a single GIA FEM model best suited for the prediction of GIA induced vertical surface deformation in Northwestern Europe. To this extent, a range of combinations between ice model inputs and rheological parameters will be assessed. This assessment will be performed using multiple RSL databases and a collection of uplift rate data. On the other

hand, this research is performed in order to gain a better understanding of the uppermost interior of the Earth in Northwestern Europe.

The research questions posed below, are believed to provide the scientific framework required to fulfil both of the previously introduced research objectives.

1. To what extent does the GIA model performance improve upon the usage of a 3D composite rheology viscosity profile, rather than a radially symmetric viscosity profile?

    (a) In terms of uplift rate?
    (b) In terms of relative sea level?

2. What 3D composite rheology GIA FEM model is best suited to model the GIA induced vertical surface deformation of Northwestern Europe?

3. What can be inferred about the Earth's interior in Northwestern Europe from the performance of various rheological configurations of the GIA FEM model?

1.7. Report outline

In this section a short outline of the remainder of this report is provided. Having briefly introduced the main inputs of a GIA model, a more extensive theoretical basis on the interior of the Earth and its viscoelastic response to glacial loading is provided in chapter 2. The interaction between glacial and oceanic surface loads, and the resulting deformation of the solid Earth can be captured by the sea level equation, which is is elaborated on in chapter 3. Furthermore, a conceptual overview of the behaviour of historic sea level is provided. In chapter 4, the various procedures that together form the 3D GIA FEM model used in this research are introduced. The main steps taken include generation of the FEM model, execution of the FEM analysis, iteratively solving the sea level equation, and implementing a revision of the surface loads. Moreover, the methods applied to analyse the modelling outputs are described. Having documented the theory and methodology behind the 3D GIA FEM model, the experimental framework of this research is explained in chapter 5. This framework consists of the range of input combinations and model settings to be tested. Included in this section as well are a discussion of the GIA observations used to analyse the RSL and uplift rate as simulated by the model. The results of the performed GIA simulations are presented and assessed in chapter 6. Through this assessment a preferred ice model and rheological configuration for GIA modelling in Northwestern Europe can be selected. The discussion of the results will ultimately lead to the formulation of the answers to the questions posed in this research. These conclusions are presented in chapter 7. This thesis is finalised through the recommendations for future research included in chapter 8.

Deformation properties of the Earth

In order to model the response of the Solid Earth to glacial and oceanic loading, it is important to gain an understanding of the relevant internal and external dynamics of the Earth. To this extent, an overview of the interior of the Earth is provided in section 2.1. This global overview is complemented by a discussion of the tectonic properties of Northwestern Europe. Next, the rheology of the Earth is elaborated on in section 2.2.3. Rheology is the "study of the deformation and flow of matter" (Barnes et al., 1989). The viscoelastic rheological properties of the solid Earth define its response to time varying loads. In section 2.3, the modified stiffness equation is discussed. This equation facilitates the application of viscoelasticity in FEM models required to model GIA.

2.1. Interior of the Earth

This section aims to provide a basic understanding of the interior of the Earth and its characteristics. To this extent, first a global overview is provided in section 2.1.1, after which a focus is applied to the interior of the Earth in Northwestern Europe in section 2.1.2.

2.1.1. Global overview

The internal structure of the Earth consists of multiple spherical shells that can be distinguished by either their chemical or their physical characteristics. The major chemical constituents are the core, the mantle and the crust. A graphical representation of the Earth's radial structure is displayed in Figure 2.1.
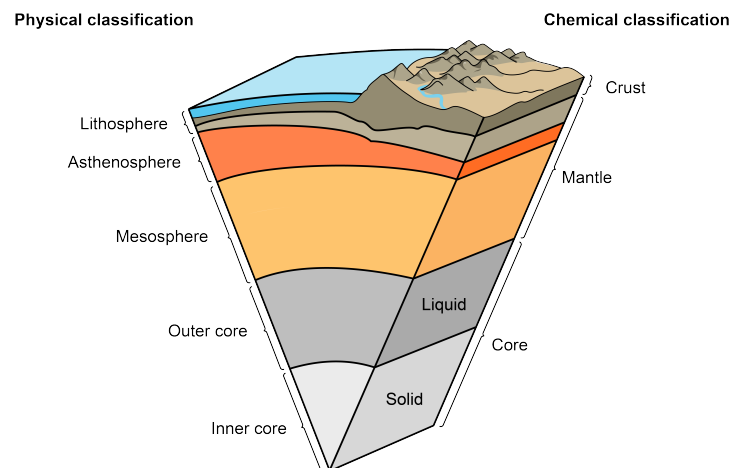
Figure 2.1: The chemical and physical classification of the Earth's layers, after Kious and Tilling (1996).

2.1.1.1. Crust

The silicate crust extends along all of the Earth's surface, thereby including any oceanic areas. The crust displays various lateral differences between the oceanic and continental zones. While the continental crust's

thickness ranges anywhere between 25 and 70 km thick, the oceanic crust is generally less than 5 km thick (Hawkesworth et al., 2010). The oceanic crust is dense and homogeneous, whereas the continental crust is less dense and very heterogeneous. The oceanic crust renews itself through subduction: the continental crust, and thereby its tectonic plates, are more buoyant than the oceanic crust, forcing the oceanic crust to subduct. This process causes the transportation of water from the oceanic crust in to the mantle. The continental crust can be divided into three crustal types, being cratons, orogens, and extensional areas (Meissner and Kern, 2011). The mean thickness and seismic signature differ for each of these types.

The upper mantle and the crust are separated by the Mohorovičić discontinuity (Moho in short). This seismic transition separates the heterogeneous and rigid crust from the more ductile and homogeneous upper mantle. The Moho is characterised by an increase in the seismic wave velocity and indicates a region of higher density in the region underneath (Prodehl et al., 2013).

2.1.1.2. Mantle

The mantle's composition can be inferred from the study of surfaced rocky material, xenoliths. Most of the material from the mantle is brought up to the surface by tectonic processes and originates from the upper mantle (McDonough and s. Sun, 1995). The majority of this layer behaves viscoelastically within the GIA time-scale.

The crust and the uppermost part of mantle together form the lithosphere. The lithosphere is characterised as mechanically strong and primarily elastic. Its definition relies on many differentiating properties, e.g. seismic, magnetic/electric, thermal, and rheological (Martinec and Wolf, 2005), each relevant for varying areas of expertise. The lithosphere is divided into tectonic plates in a lateral sense. New lithospheric matter is formed at mid-oceanic ridges where plates diverge, and thickens as it ages due to the associated cooling processes. The seismically defined lithosphere ceases at the Lithosphere-Asthenosphere Boundary (LAB), which can be found at 80 - 90 km depth beneath continental regions and at 70 km depth beneath oceanic regions. This transition can be recognised by a sharp decrease in seismic velocities (Rychert and Shearer, 2009).

Beneath the lithosphere lies the asthenosphere, which is characterised as mechanically weak. The viscosity of this layer in particular is believed to be of the order of 10^{20} or 10^{21} in magnitude on a global scale (Lambeck et al., 1998; Mitrovica and Forte, 1997). At circa 410 km a discontinuity is encountered. This marks the start of a zone which is poorly understood and hard to evaluate on a global level due to the limited sensitivity of different seismic waves in this area Ritsema et al. (2004). Another major discontinuity, can be found at a depth of circa 670 km (Mitrovica and Forte, 1997; Ritsema et al., 2011). It is at this continuity that the asthenosphere ends and the upper mantle transitions into the lower mantle. The lower mantle is believed to be of a higher viscosity than the upper mantle, by 1 or 2 orders of magnitude (Lambeck et al., 1998; Mitrovica and Forte, 1997).

The mantle transitions into the Earth's core at the Core-Mantle Boundary (CMB). The core is believed to consist of an outer liquid shell and a solid iron centre (Montagner, 2011). Our knowledge of the Earth's beyond the upper mantle is however limited. While the existence of the CMB could yield a large upward buoyancy response to glacial loading, this is only the case for very large ice sheets. As this does not apply in Northwestern Europe, it is reasoned that the crust and mantle are of primary interest to GIA research in this area.

2.1.2. Tectonic properties of Northwestern Europe

Europe can be divided into geological regions based on the origin of the various parts of its continental landmass. This distribution of tectonic origin is depicted in figure 2.2. The continent's two main constituents are a Precambrian craton, called the East European Craton (EEC), in the North and East, and a collection of blocks of Proterozoic-Palaeozoic origin along the West and South (Plant et al., 2003). These two sections are divided by the Trans-European Suture Zone (TESZ), or Tornquist-Tesseyre Suture Zone (TTSZ) (Zhu et al., 2015), which runs from the North Sea to the Black Sea in NW-SE direction. The least uniform of the two regions is composed of former micro continents which moved towards the Southwestern margin of the EEC over the course of many years (Plant et al., 2003). A small part of the continent located beneath Northern Scotland has a late Proterozoic signature and is believed to be a fragment of the North American-Greenland landmass. The assembly of material of varying origins is sometimes referred to as accretion and can lead to tectonic collision and subduction. A signature of a divergent motion is present beneath the North Sea. This rift valley is characterised by the Central Graben, which originates near the Dutch coast and runs northwards. Near the Scottish coast, the Central Graben transitions in to the Viking Graben, which runs along the south-east coast of Norway.

Through seismic studies, an insight into the properties of the Earth's interior can be obtained. In a surface wave study conducted by Nita et al. (2016), a significant differentiation between the continents main geological regions along the TESZ was found: whereas the thickness of the seismically defined lithosphere beneath the older cratonic region is 200-220 km, that of the younger region in the South-West is about 80 km. This conclusion bears similarities to that of Steffen and Kaufmann (2005), who researched the viscosity structure in Northwestern Europe through the application of a different technique. Using paleoshoreline data combined with radial GPS deformation rates from the BIFROST GPS project, evidence was found for a large differentiation between the lithospheric thickness in the area. This thickness ranged between 60 to 70 km underneath Northwestern Europe and the Barents Sea, and over 120 km underneath Scandinavia. Also, a low viscosity zone was found underneath the Barents Sea at 160 to 200 km depth, where viscosities range between 10^{19} and 10^{20} Pa s.
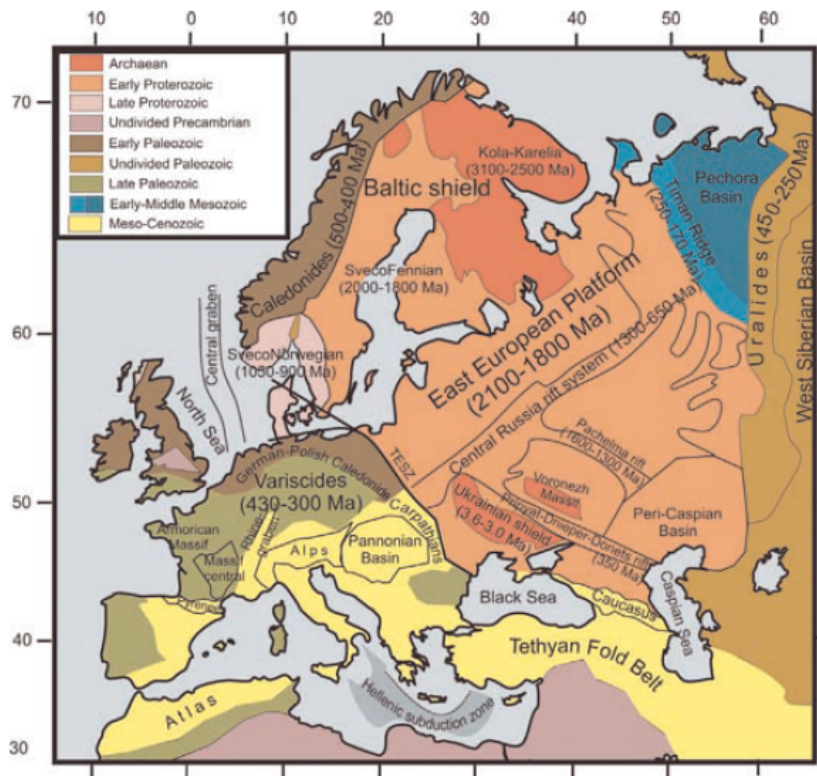
Figure 2.2: Tectonic origins of various parts of Northwestern Europe. From Artemieva et al. (2006), figure 1.

Seismic observations can also be used to generate a thermal model of the interior of the Earth. This research aims to use such a seismically derived thermal model in order to define a 3D viscosity distribution for Northwestern Europe. In this way, seismic observations are used to study the effects of the inclusion of 3D heterogeneity in a GIA model. How the viscosity distribution used in this research is obtained, will be detailed in section 5.2 later on.

2.2. Composite rheology

Rheology is the study of the deformation and flow of matter, and here the theoretical concepts behind the combination of linear and non-linear rheology are discussed. Firstly, an insight into linear viscoelasticity is provided in section 2.2.1. Afterwards, the two dominant non-linear creep mechanisms that are part of a composite rheology are detailed in section 2.2.2. This section is concluded with an overview of the composite rheology flow laws defining the relation between stress and strain in section 2.2.3, and a description of how this relation is implemented in FEM models to model deformation behaviour of the Earth in section 2.3.

2.2.1. Linear viscoelasticity

Materials that combine both the mechanical properties of an elastic solid and a viscous fluid are called viscoelastic. The behaviour of elastic solids, viscous fluids, or a combination of the two, can be identified by their unique response under external loading in terms of stress, strain, and deformation. An elastic material is known to deform linearly and instantaneously with the force applied, and will return back to its original shape once this force is removed as captured by Hooke's Law. In contrast to elastic materials, viscous materials will continue to strain over time whilst a constant external force is applied. Also, part of the deformation experienced by a viscous material will remain even after the force has been removed.

The viscoelastic response of the solid Earth to surface loads that change over time, is commonly modelled using a linear Maxwell rheology. This rheology follows the behaviour of a spring to represent elasticity, and a dashpot to represent a purely viscous Newtonian fluid, placed in series. The Maxwell model has often been applied to study the response of the Earth to deglaciation. Extensively studied in the past (Han and Wahr, 1995; Kaufmann and Wu, 1998; Peltier, 1974; Wu and Peltier, 1982), the model is also used frequently in more recent research (Paulson et al., 2005; Wang and Wu, 2006).

The constitutive relation for a Maxwell rheology is included in equation 2.1 (Peltier, 1974). In this equation no initial stress is applied. Since the elastic and viscous components of a Maxwell body operate in series, this equation follows from the summation of their respective strain rates whilst the stress in both components is equal.

$$\dot{\sigma}_{ij} + \frac{\mu}{\eta}(\sigma_{ij} - \frac{1}{3}\sigma_{kk}\delta_{ij}) = 2\mu\dot{\epsilon}_{ij} + \lambda\dot{\epsilon}_{kk}\delta_{ij} \tag{2.1}$$

Here σ and ϵ denote stress and strain, δ_{ij} is the Kronecker delta, λ and μ are the Lamé elastic constants (Malvern, 1969), and η is the viscosity.

2.2.2. Composite rheology

Maxwell viscoelasticity displays characteristics of elastic and viscous materials, which are both considered linear. However, as concluded from rheological experiments at mantle-like conditions (Hirth and Kohlstedt, 2003; Karato and Wu, 1993), non-linear viscous behaviour is also believed to be present within the Solid Earth. The combination of linear and non-linear viscoelastic behaviour is called composite rheology. In order to understand the rheological response of the solid Earth to glacial and oceanic loading, the next sections will detail both the linear and non-linear (power-law) components of composite rheology, and the parameters required to define the composite rheology behaviour of the Earth.

2.2.2.1. Diffusion creep

Diffusion creep corresponds to linear viscoelasticity and may consist of two components, Herring-Nabarro creep and Coble creep. The Herring-Naborro response originates from the migration of molecular or atomic vacancies through a crystal lattice due to an applied stress in a thermally activated medium (Gordon, 1965). A graphic representation of this process is provided in Figure 2.3a. Here a number of crystallites, or grains, subjected to stress σ are depicted. A single grain is highlighted in grey, its boundaries and that of neighbouring grains are shown in solid black lines. It can be seen that various vacancies exist within the original crystal lattice on the left. Given stress σ, the vacancies migrate from their sources to so-called vacancy sinks. In the specific case depicted, this allows for elongation of the grain in the direction of the stress applied. For a material consisting of various atoms, the diffusion creep is governed by the effective diffusivity. The atomic species with the lowest diffusion rate is used to determine this variable (Gordon, 1965).

Coble creep is predominant in the lower temperature regions in which diffusion creep applies (Ranalli, 1995). In figure 2.3b the effect of Coble creep is depicted. It can be observed that grain boundary diffusion allows for mass transport along the grain boundaries themselves. The resulting elongation of the grain is demonstrated by the displacement of the reference marking, a hypothetical scratch made along three neighbouring grains prior to loading. Since diffusion can occur within the crystal lattice (Herring-Nabarro creep) but also along the grain boundaries (Coble creep) simultaneously, the effective diffusion coefficient consists of the sum of their respective diffusion coefficients.

2.2.2.2. Dislocation creep

Dislocation creep, or power-law creep, corresponds to the non-linear relation between shear stress and strain-rate. Thus, the strain rate is proportional to the stress applied to the power $n > 1$. Dislocation creep corresponds to the process of a consecutive slipping motion of rows of atoms within a crystal lattice (Ranalli, 1995).

(a) Nabarro-Herring creep

(b) Coble creep
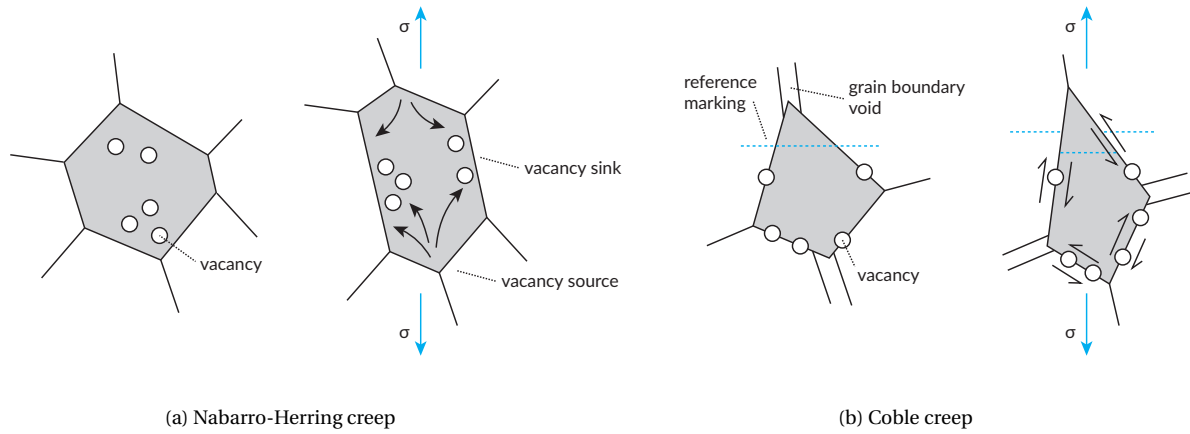
Figure 2.3: Effects of two types of diffusion creep.

As a dislocation migrates to the boundary, the entire crystal is subjected to a shearing effect. This is shown in figure 2.4. Here the lower half of the crystal lattice shown is shifted to the left-hand side. It can be seen that the lattice connections in the proximity of the dislocation, indicated by the coloured dashed lines, are altered, allowing for the lattice to change shape without brittle failure.
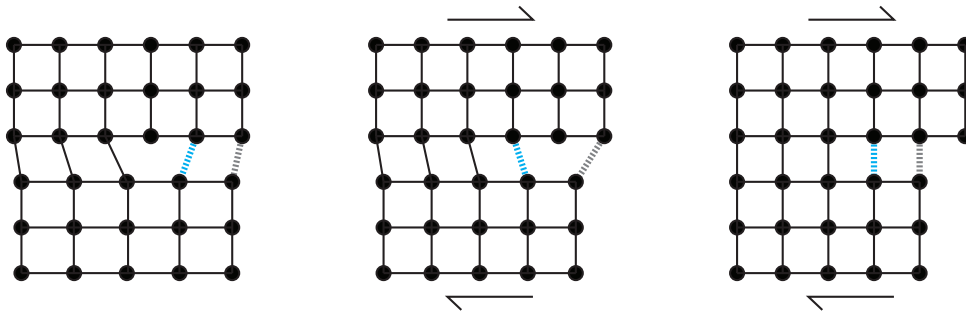
Figure 2.4: Dislocation creep within a crystal lattice.

2.2.3. Flow laws and creep parameters

Through mainly experimental research as described by Ranalli (1995) multiple rheological flow laws have been defined. The flow law that is applied in this research has been formulated by Hirth and Kohlstedt (2003). Equation 2.2 displays this power-law relation between the strain rate $\dot{\epsilon}$ and stress σ for the material olivine, the main constituent of both the lithosphere and asthenosphere (Karato et al., 1986).

$$\dot{\epsilon} = A\sigma^n d^{-p} f_{H_2O}{}^r \exp\left(\alpha\varphi\right) \exp\left(-\frac{E+PV}{RT}\right) \tag{2.2}$$

Here A and α are constants, n is the stress exponent, d is the grain size and p its exponent, f_{H_2O} is water fugacity, r the water fugacity exponent, φ is the melt fraction, E is the activation energy, P is pressure, V is the activation volume, R is the gas constant, and T is the absolute temperature. With these variables many rheological concepts are introduced, such as the difference between dry and wet rheology and partial melt, which will be touched upon later in this section. Both diffusion and dislocation creep parameters can be computed using the above flow law, as shown in equation 2.3 (van der Wal et al., 2013):

$$B = A d^{-p} f_{H_2O}{}^r \exp\left(\alpha\varphi\right) \exp\left(\frac{E+PV}{RT}\right) \tag{2.3}$$

It can be seen that by setting $n = 1$ and $p = 3$, as done by Hirth and Kohlstedt (2003), the flow law in equation 2.2 reduces to a linear stress-strain rate relation. These values for n and p followed from experimental data for both dry and wet rheology. Using this configuration, the creep parameter B_{diff} can be determined. For dislocation creep and its corresponding creep parameter B_{disl}, these values in dry conditions were found to be equal to $n = 3.5$ and $p = 0$ respectively. This supports the notion that dislocation creep is independent of grain size and dominates in areas of high stress, whereas diffusion creep dominates in areas of low stress that contain grains of a small size (Hirth and Kohlstedt, 2003; van der Wal et al., 2013).

As mentioned previously, the strain (rate) in a composite rheology setup consists of the summation of its two constituents, dislocation and diffusion creep. In composite rheology a relation exists between viscosity and stress. This relation, given by (Ranalli, 1995), is depicted in equation 2.4 below, and contains the combined strain rate $\dot{\epsilon}_{ij}$ (van der Wal, 2009).

$$\eta_{eff} = \frac{\sigma'_{ij}}{2\dot{\epsilon}_{ij}} \tag{2.4}$$

The combined strain rate itself is computed using the individual contributions of the two types of creep.

$$\dot{\epsilon}_{ij} = \dot{\epsilon}_{ij,\text{diff}} + \dot{\epsilon}_{ij,\text{disl}} \tag{2.5}$$

$$\dot{\epsilon}_{ij,\text{diff}} = \frac{3}{2} B_{\text{diff}} \sigma'_{ij}$$
$$\dot{\epsilon}_{ij,\text{disl}} = \frac{3}{2} B_{\text{disl}} q^{n-1} \sigma'_{ij} \tag{2.6}$$

Here q is the von Mises stress, being $q = \sqrt{\frac{3}{2}\sigma'_{ij}\sigma'_{ij}}$ (van der Wal et al., 2013). The above leads to a rearranged definition for the effective viscosity:

$$\eta_{eff} = \frac{1}{3B_{\text{diff}} + 3B_{\text{disl}}q^{n-1}} \tag{2.7}$$

This definition of effective viscosity is used to assign the appropriate viscosity to all individual elements in the Abaqus model, based on their specific material properties. The exact procedure followed and the (experimental) input data used will be covered in sections 4.3 and 5.2. The concepts of dry versus wet rheology, grain size change, and partial melt within Northwestern Europe are briefly discussed below.

2.2.3.1. Water content

Subduction of oceanic plates leads to the transportation of water in to the upper mantle. Experimental research on olivine aggregates has shown that the consequent presence of water in this part of the mantle, enhances the creep rate for both diffusion and dislocation creep (Karato et al., 1986). It is suggested that for diffusion creep water enhances the rates at which diffusion occurs, whereas for dislocation creep the water weakening is mainly caused by inter-granular effects. When analysing the strain rate using the power law in equation 2.2, one can evaluate for a dry of wet rheology by altering the flow law parameters affected by the dry or wet state of the material in accordance with table 2.1.

Table 2.1: Rheological flow law parameters for different configurations of creep type and water content. From Hirth and Kohlstedt (2003), tables 1 and 2.

		p	r	A	E [kJ/mol]	V [m^3/mol]
Wet	diffusion	3	1	1.0E6	335	4.00E-6
Dry	diffusion	3	–	1.5E9	375	5.00E-6
Wet	disclocation	0	1.2	9.0E1	480	1.10E-5
Dry	dislocation	0	–	1.1E5	530	2.30E-5

As was described in section 2.1.2, the tectonic heterogeinity of Northwestern Europe is caused by the accretion of material of varying origin. It is possible that these tectonic collisions have enabled the transportation of water in to the upper mantle of Northwestern Europe. It is however uncertain in what specific regions within the mantle contain water, and how the water content in the mantle changes over time. Dixon

et al. (2004) suggest that the interior of the Earth can retain its water content for tens to hundreds of millions years in the absence of significant tectonic or thermal activity. The aforementioned leads to believe that it is of importance to account for the presence of water in the mantle beneath Northwestern Europe. This importance is supported by the suggestion of Barnhoorn et al. (2011) that the mantle beneath Scandinavia should be characterised as wet.

2.2.3.2. Grain size

As was mentioned previously, the composition of the interior of the Earth beneath Northwestern Europe in terms of water content may have been influenced by tectonic accretion. Such tectonic processes may also affect the composition in terms of grain size. Annealing due to high temperatures could lead to grain size growth, whereas high stresses could lead to grain size reduction (Barnhoorn et al., 2011). These circumstances may have existed during the formation of the European continent, and as such it is believed that the grain size within Northwestern Europe could be dependent on tectonic origin. Additionally, it should be noted that the grain size may increase with depth by an order of 1 between the uppermost mantle and the transition zone (Faul and Jackson, 2005).

2.2.3.3. Partial melt

Partial melt of olivine can cause severe deterioration of the strength of an aggregate as its value exceeds 4% (Dijkstra et al., 2002). At significantly higher values for melt fraction φ the material's response to stress is equal to that of the viscous flow of the molten aggregate (Renner et al., 2000). However, partial melt is mostly associated with regions within the mantle and crust that experience severe pressure or heat, such as in tectonically active regions. It is believed that the threshold of $\varphi > 4\%$ is not met in the relatively inactive and cold Northwestern Europe, rendering partial melt negligible at this time (van der Wal et al., 2013).

2.3. Modelling the Earth using FEM software

In the previous sections, the viscoelastic rheology of the Earth has been characterised. Here, this material-specific behaviour is incorporated in the modifications that are required for the usage of commercial FEM software for the purpose of GIA modelling (Wu, 2004). Also, a brief discussion of the rotational behaviour of the Earth is provided.

2.3.1. Modified stiffness equation

In FEM software packages the governing equation solved is the stiffness equation. This stiffness equation is set equivalent to the equation of motion, in accordance with the principle of virtual work. Hence the external and internal work done by a force are in equilibrium, which gives rise to equation 2.8 (Wu, 2004):

$$\nabla \cdot \sigma_{ij} = 0 \tag{2.8}$$

Here σ_{ij} is the Maxwell viscoelasticity stress tensor, which has been introduced in section 2.2.1. Note that the notation from Wu (2004) has been slightly adapted to match that of viscoelasticity as introduced in section 2.2.1. For geophysical applications, equation 2.8 can be extended resulting in the linearised elastic equation of motion, or modified stiffness equation, in equation 2.9 (Wu, 2004). It should be noted that the solution for a viscoelastic problem, is obtained from the solution of its so-called associated elastic problem.

$$\nabla \cdot \sigma_{ij} - \nabla(u \cdot \rho_0 g_0 \hat{r}) - \rho_1 g_0 \hat{r} - \rho_0 \nabla \phi_1 = 0 \tag{2.9}$$

Here u is the displacement vector, $\hat{r}$ the unit vector in radial direction, ρ the density, g the gravitational acceleration, and ϕ the gravitational potential. The subscript 0 indicates the unperturbed background state, and subscript 1 indicates the perturbed state. The first term, also visible in equation 2.8, is the divergence of stress. In equation 2.9, terms are added that - from left to right - represent the restoring force of isostasy, internal buoyancy, and self-gravitation. Thereby, this equation is valid for a spherical, self-gravitating, compressible Earth. In order to apply equation 2.9 in FEM, the stress tensor must be redefined such that it includes all added terms and matches the notation of equation 2.8 (Wu, 2004). The boundary conditions must be transformed in a similar fashion in accordance with the newly defined stress tensor. Finally, it should be noted that while compressibility is included in this modified stiffness equation, compressibility effects are not taken into account in FEM GIA models. Similarly, this research does not account for compaction, nor the rotational behaviour of the Earth.

2.3.2. Rotational behaviour of the Earth

The rotational behaviour of the Earth is affected by the redistribution of mass both on the surface and within the interior of the Earth. Such GIA induced mass redistribution gives rise to a drift of the Earth's rotational axis, known as True Polar Wander (TPW) (Wu and Peltier, 1984). The change of the rotational axis and rotational potential of the Earth, results in a deformation of both the geoid and the solid surface. This in turn leads to a rotation-induced component of sea level change. These deformations and the induced sea level change are characterised by a spherical harmonic of degree two, order zero (Milne and Mitrovica, 1998). Present day uplift rates due to TPW can exceed 0.5 mm per year (Mitrovica et al., 2001). The signature of this TPW-induced effect is however of very long wavelength, meaning that it is unlikely that large relative differences will arise in the deformation of the solid surface or sea level change within Northwestern Europe.

While it is preferred to include the effect of TPW in global GIA models specifically, the rotational behaviour of the Earth is not accounted for in this study. In the future, this could be achieved by substituting the spherical harmonic coefficients affected by TPW with those coefficients obtained from a GIA model of a rotating Earth. Alternatively, the 3D GIA FEM model should be adjusted such that both 3D composite rheology as well as the rotational behaviour of the Earth can be accounted for. Efforts to do so are currently ongoing within the research group (Weerdesteijn, 2019).

3

Glacial and oceanic interaction

In this chapter, a theoretical overview of the interaction between glacial and oceanic loading is provided. While the glacial loading is a direct input of the 3D GIA FEM model, the oceanic loading is computed from the ice mass loss or gain over time. The sea level equation, described in section 3.1, is used to determine how the oceanic load is distributed over the deformed surface of the Earth. This deformation is the result of the FEM analysis. Having dealt with the mathematical background of sea level computations, section 3.2 discusses how past sea level change can be observed. Additionally, this section will provide an insight into how such observations are used in this research.

3.1. Definition of the sea level equation

Farrell and Clark (1976) were the first to derive a mathematical expression of an equation that describes the change in sea level due to a rearrangement of water and ice on the surface of the Earth. Their theory applies to an elastic or Maxwell viscoelastic, spherically symmetric, self-gravitating, non-rotating Earth. An extension of the classical sea level equation (SLE) has been proposed by Kendall et al. (2005). This extension includes the effect of shoreline evolution over time and is valid for any Earth model. As such, this extended sea level equation has been used in the development of the 3D GIA FEM model that is employed in this research. A more detailed explanation of the sea level equation as proposed by Kendall et al. (2005) and implemented by Blank (to be published, personal communication) follows in this section. Note that due to added complexity, the spatial and temporal effects of the rotational behaviour of the Earth and tidal dynamics are not taken into account in this procedure.

The sea level is defined as the difference between the radial position of the geoid and solid surface G and R respectively. Coincidentally, the topography is equal to the inverse of the sea level. This relation is captured in equation 3.1. The spatial and temporal dependence of all terms in this equation are represented by colatitude θ, longitude ψ and time within the glacial cycle t_j.

$$SL(\theta, \psi, t_j) = G(\theta, \psi, t_j) - R(\theta, \psi, t_j) = -T(\theta, \psi, t_j) \tag{3.1}$$

The sea level at time t_j follows from the sea level at the onset of the simulation t_0, and the GIA-induced change in sea level since time t_0:

$$SL(\theta, \psi, t_j) = SL(\theta, \psi, t_0) + \Delta SL(\theta, \psi, t_j) \tag{3.2}$$

When expressed with respect to the present day, the change in sea level may be referred to as the relative sea level (RSL). The change in sea level consists of the summation of the change of the solid surface and the geoid anomaly as described in equation 3.3. The latter can be split into a spatially varying component $\Delta\mathcal{G}(\theta, \psi, t_j)$ and a spatially uniform shift in the geoid $\Delta\Phi(t_j)/g$:

$$\Delta SL(\theta, \psi, t_j) = \Delta G(\theta, \psi, t_j) - \Delta R(\theta, \psi, t_j) \tag{3.3}$$

$$\Delta G(\theta, \psi, t_j) = \Delta\mathcal{G}(\theta, \psi, t_j) + \frac{\Delta\Phi(t_j)}{g} \tag{3.4}$$

Using equations 3.3 and 3.4, the total change in sea level can be rewritten in terms of a spatially uniform and spatially variant term as is shown below. This spatially uniform geoid anomaly ultimately follows from the conservation of mass in the oceanic and glacial surface loads, and is thereby equal to the eustatic rise in global sea level. In this application of the conservation of mass, it is assumed that both the ice masses and oceanic masses have a constant density. Hence, the influence of temperature variations within these masses over time is neglected. Additionally, sediment deposition is not accounted for.

$$\Delta \mathcal{SL}(\theta, \psi, t_j) = \Delta \mathcal{G}(\theta, \psi, t_j) - \Delta R(\theta, \psi, t_j) \tag{3.5}$$

$$\Delta SL(\theta, \psi, t_j) = \Delta \mathcal{SL}(\theta, \psi, t_j) + \frac{\Delta \Phi(t_j)}{g} \tag{3.6}$$

In addition to the sea level, the ocean height S is defined in equation 3.7:

$$S(\theta, \psi, t_j) = SL(\theta, \psi, t_j) \cdot C(\theta, \psi, t_j) \beta(\theta, \psi, t_j) \tag{3.7}$$

Here the ocean function is defined by

$$C(\theta, \psi, t_j) = \begin{cases} 1 & \text{if } SL(\theta, \psi, t_j) > 0 \\ 0 & \text{if } SL(\theta, \psi, t_j) \le 0 \end{cases}$$

And the β-field assumes the following value

$$\beta(\theta, \psi, t_j) = \begin{cases} 1 & \text{where there is no grounded ice} \\ 0 & \text{where there is grounded ice} \end{cases}$$

A graphical representation of the meaning of the ocean function and the β-field is included in figure 3.1. Note that these definitions imply that the ocean height $S(\theta, \psi, t)$ is only non-zero for oceanic regions. This opposed to the sea level $SL(\theta, \psi, t)$, which assumes a non-zero value for both oceanic and continental regions.
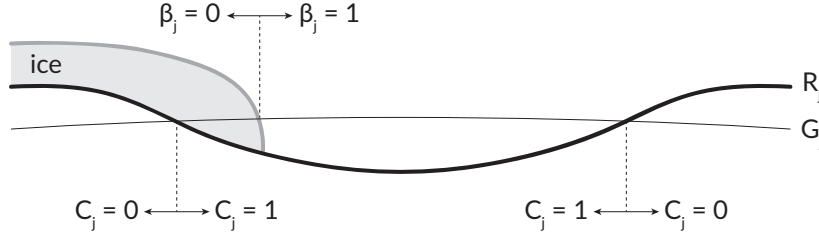
Figure 3.1: Schematic overview of the ocean function and the β-field. Note that the sea level SL_j is positive where $G > R$ and negative where $G < R$. The short form notation C_j is adopted as a substitute for $C(\theta, \psi, t_j)$ and all other variables accordingly. After Kendall et al. (2005), figure 2.

Using the aforementioned equations, it is now possible to define the generalised sea level equation (GSLE) (Kendall et al., 2005) in equation 3.8. The physical meaning of shoreline evolution that is captured by this equation will be detailed in the next section.

$$\begin{aligned} \Delta S(\theta, \psi, t_j) = & \Delta SL(\theta, \psi, t_j) C(\theta, \psi, t_j) \beta(\theta, \psi, t_j) \\ & - T(\theta, \psi, t_0) \left[C(\theta, \psi, t_j) \beta(\theta, \psi, t_j) - C(\theta, \psi, t_0) \beta(\theta, \psi, t_0) \right] \end{aligned} \tag{3.8}$$

3.1.1. Shoreline evolution

While early definitions of the sea level equation assumed that the location of shorelines, and thereby the ocean function, is independent of time, GIA-induced shoreline migration is accounted for in the GSLE defined by Kendall et al. (2005). This migration can be divided into the two categories discussed here. In figure 3.2 a schematic overview of shoreline migration due to a local sea level change is depicted. Onlap corresponds to rising sea level, whereas offlap corresponds to a falling sea level. This type of shoreline migration does not account for the presence of grounded marine ice. The effect of changes in said ice mass is included in figure

3.3. As the grounded marine ice melts and retreats, the sea level rises due to an influx of water. This process is also known as water dumping.
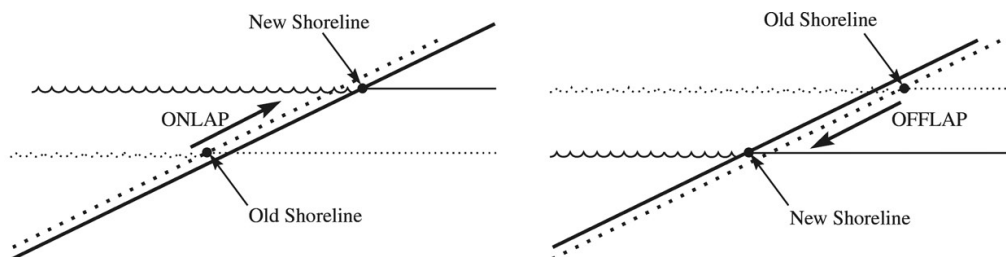
Figure 3.2: Shore-line migration in the case of ocean onlap (left) and offlap (right) respectively. After Mitrovica (2003), figure 2.
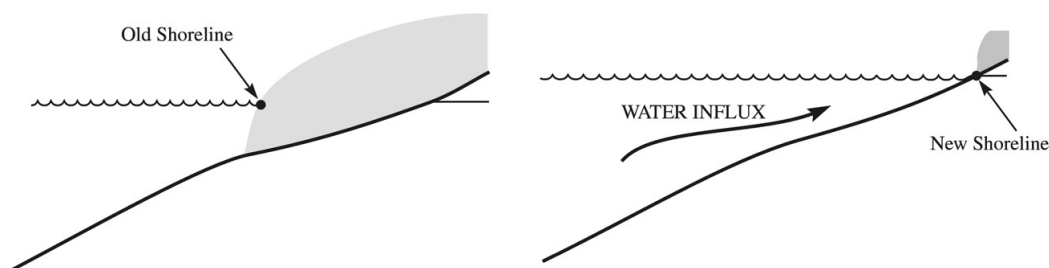
Figure 3.3: Influx of water into a region previously occupied by a grounded marine-based ice mass. After Mitrovica (2003), figure 2.

3.2. RSL observations

In this section, a brief theoretical discussion on RSL observations is included. Such historical sea level records will be used to analyse to what extent the 3D GIA FEM model in this research can reproduce the observations. An insight into how such observations are acquired, is provided in section 3.2.1. Next, section 3.2.2 details how such RSL observations can be interpreted based on common RSL behaviour.

3.2.1. Measurement techniques

Sea level data can be recorded in a so called sea level index point (SLIP), which document an estimate of the RSL at a certain time and place, as well as the associated uncertainty (Hijma et al., 2015). Past changes in sea level can be identified from the dating of paleoshorelines or other sea level indicators. Traditionally paleoshorelines can be identified through carbon-dated geomorphological or biological markers. These markers are recovered from so-called cores, and may contain for example organic material which can only be found in salt-water environments. The diversity of markers that can be used to estimate RSL, allows for the definition of so called upper (terrestrial) and lower (marine) limiting data points (Hijma et al., 2015). More contemporary sea level data can be obtained from satellite altimetry or tidal gauges, the latter of which may provide RSL records spanning the last 100 years (Whitehouse, 2009, 2018). Most SLIP's can be found in close proximity of present-day shorelines.

3.2.2. Common RSL behaviour

Three interacting factors contribute to the magnitude and sign of RSL change. Aside from the eustatic increase or decrease in global ocean volume, both vertical tectonic movement and vertical movement of glacio- or hydro-isostatic origin alter RSL (Steffen and Wu, 2011). Since these factors differ on a regional scale, RSL curves are a reflection of the distance to a historic ice sheet. This implies that RSL data can be divided into far-field and near-field data (Whitehouse, 2009). These differences, depending on distance from the former ice sheet centre, are illustrated in figure 3.4. Here three types of behaviour can be recognised, which are discussed below (Steffen and Wu, 2011). The figure also includes the periods for which no RSL observations can be made; historic sea level cannot be recorded until ice covered areas become flooded by oceans instead.

The initial value for relative sea level near the centre of the ice sheet is very high. This is due to a combination of the gravitational attraction of the large body of ice, and the relatively low position of the solid surface

beneath the ice. During deglaciation, uplift of this surface occurred rapidly as the ice load diminished. This response is slowed once deglactiation is complete. When compared to the near-field region, the mid-field region initially displays similar behaviour. Near the margins of the ice sheet, rapid uplift may cause the RSL to attain a negative value. This region however becomes ice-free at an earlier point in time, and is quickly flooded by the resulting melt water. After this sea level rise, a drop in RSL can be observed due to forebulge migration. In the far field, subsidence of the land and eustatic sea level rise infer an overall sea level rise beyond present-day sea level values. Far field observations can be used to infer constraints on the eustatic component of sea level rise.
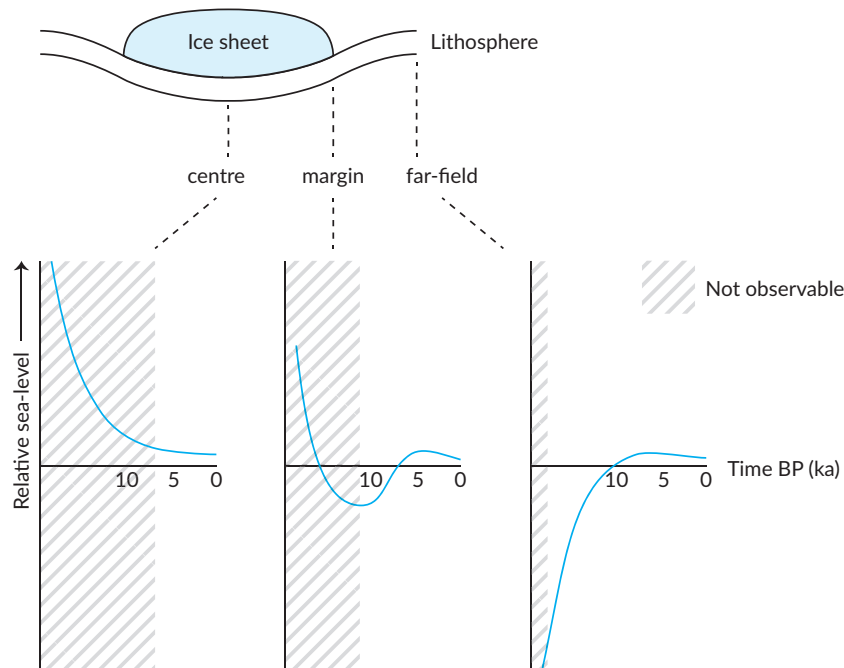
Figure 3.4: General appearance of RSL records related to the distance from the former ice sheet. After Steffen and Wu (2011), figure 4.
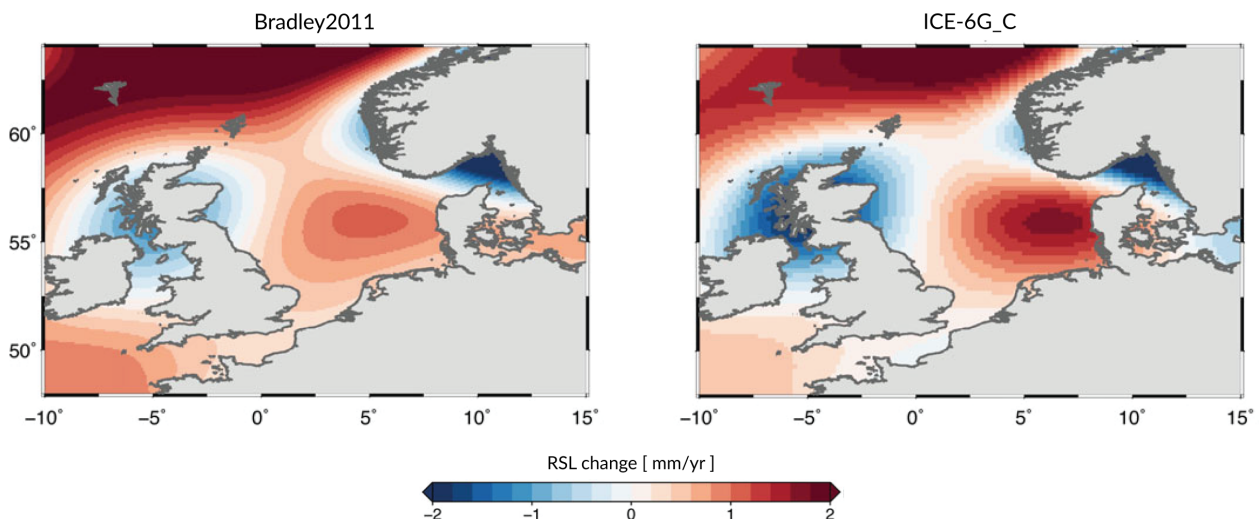
Figure 3.5: Present-day relative sea level change as predicted by the Bradley2011 model (Bradley et al., 2011) and ICE-6G_C VM5a model (Peltier et al., 2015). After Vermeersen et al. (2018), figure 6.

It is expected that within Northwestern-Europe, near-field RSL behaviour will be encountered near the centres of the former ice sheets, i.e. in Central Scotland, Norway, Sweden, and Finland. The mid-field behaviour is most likely to be observed towards the margins of the BIIS and FIS, located along the Scottish and

Scandinavian coasts, but also in Northern England, Ireland, Denmark, and the Doggerbank. All other regions are expected to display primarily far-field RSL behaviour. This agrees with the expected signature of present day relative sea level change rates in the North Sea as captured in figure 3.5, where sea level rise is present in the far field and sea level fall is shown near the former ice sheets. Similar plots will be constructed for a selection of the best performing models, in sections 6.2 and 6.3.

4

The 3D GIA FEM model

Having defined the theory behind the distribution of loads on the Earth and its response to these temporal and spatially varying loads, this chapter details how these effects are modelled. Firstly, a high level overview of the existing model is provided in section 4.1. Following this overview, the generation of the model is discussed in sections 4.2. Next, the implementation of the previously discussed theory on 3D composite rheology as well as the sea level equation within the 3D GIA FEM model are elaborated on in sections 4.3 and 4.4.2 respectively. This chapter concludes with an insight into the further processing of the GIA induced deformation of the Earth required to determine present day uplift rates.

4.1. Model overview

A high level overview of the 3D GIA FEM model and the inputs, outputs, and scripts involved, is included in figure 4.1. It can be seen that the `Model_data.py` script is used to define all model settings and paths to relevant input files. This file is imported by every other processing script within the model, to ensure the same variables are used throughout the entirety of a single model run. The first processing script to do so is the `Model_gen.py` script. This script is executed in the Abaqus Python Development Environment (PDE), and is used to construct the Abaqus FEM model. The steps undertaken in this process are explained in section 4.2. After generation of the Abaqus FEM model, the `iter_ult.py` script is executed in the PDE. This script contains an iterative procedure to perform the FEM analysis, refine the subsequent output, and call on a nested script in order to solve the sea level equation as described in section 4.4.2. Each iteration ends with a revision of the surface loads in the Abaqus FEM model, thereby setting up the next iteration. The main outputs from the overall model are the radial deflection of the surface and the relative sea level for all time steps.

An overview of the files associated with this high level overview is given in table 4.1. Throughout the remainder of this chapter, individual parts of the model will be discussed in further detail. Any additional files discussed will be included in similar tables at the start of each subsection.
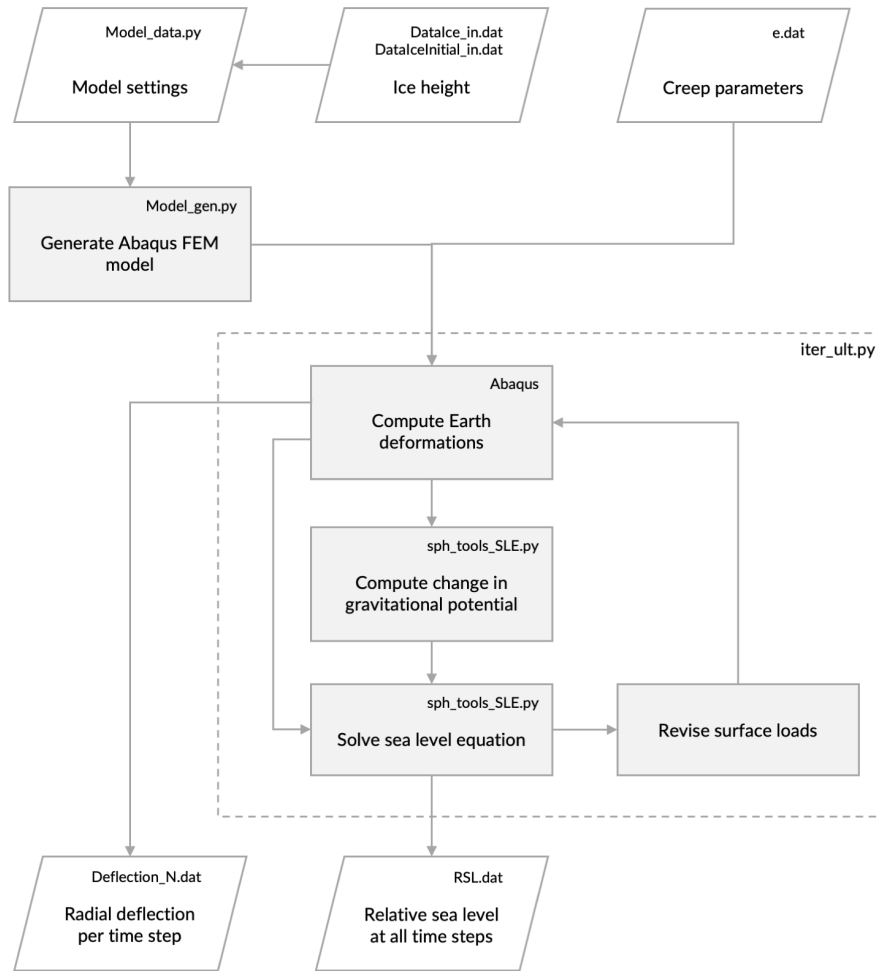
Figure 4.1: High level overview of the 3D GIA FEM model by Blank (to be published).

Table 4.1: Overview of main model files.

File	Type	Main function	Output
DataIce_in.dat	Input	Contains ice heights with respect to ice height at the initial time step.	N/A
DataIceInitial_in.dat	Input	Contains ice height at the initial time step.	N/A
e.dat	Input	Contains dislocation creep and diffusion creep parameters for each finite element.	N/A
Model_data.py	Input	Define all inputs and model settings.	N/A
Model_gen.py	Process	Build the Abaqus FEM model. Define layers, mesh, loads, and analysis.	Earth.cae model database
Iter_ult.py	Process	Perform Abaqus job analysis. Refine output data and execute SLE module. Adjust model database for next iteration.	Deflection_N.dat
sph_tools_SLE.py	Process	Solve the sea level equation	RSL.dat

4.2. Abaqus FEM model creation

In this section an overview is provided of the procedure followed in the generation of the ABAQUS FEM model. The structure of this section largely resembles the step-by-step build-up of the FEM model itself. The generation of the various layers of the Earth is discussed in section 4.2.1. Afterwards, the finite element mesh is defined as described in section 4.2.2. Finally, in section 4.2.3, the application of loads to the model is discussed.

Table 4.2: Addition to model files for FEM model generation.

File	Type	Main function	Output
layer data.txt	Input	Contains layer radius, density, Young's modulus, and viscosity.	N/A
Initial_CoG_correction.py	Process	Perform an initial correction of the model's centre of gravity due to glacial and oceanic loading of the surface.	CoG_vector.dat

4.2.1. Layer generation

The Abaqus model is generated from the inside out. In accordance with the the data from the `layer data.txt` input file, firstly a core part is generated after which multiple shells around this core are created. The shell boundaries are located at a constant depth. All individual parts are divided into eight individual sections. In Abaqus, the process of dividing a part through virtual cutting of said part, is referred to as partitioning. This partitioning is performed in the three planes of the right-handed, y-up axis system. The definition of the Abaqus axis system and the partitioning of the spherical parts of the model is shown in figure 4.2a. This measure is taken to ensure that correct discretisation of the layers occurs when all parts are meshed at a later stage. The edges of the partitions serve as a guideline for the application of the mesh, and mimic the Earth's equator and longitudinal meridians. A more thorough explanation of the mesh application follows in section 4.2.2.

After the layers have been created and partitioned, the appropriate material properties are assigned to each layer. This data also originates from the layer data input file, and applies a radial viscosity distribution to the model. In case the viscosity of a layer is nonzero and lower than 1E40 Pa s, it is assigned viscoelastic behaviour. The crust, which is assigned a viscosity larger than 1E40 Pa s, is assigned purely elastic behaviour. Whilst the core is also assigned purely elastic behaviour, some attention goes out to the overall properties of this part within the FEM model. By using a near-zero value for the core's Young's modulus of 1E-20 Pa s, a negligible lateral stress is exerted on the CMB. The core is present as a part within the FEM model only to warrant incompressibility (Blank, personal communication).

After all FEM parts have been generated and the default material properties have been assigned, one can alter the material properties of specific layers in order to enforce a 3D rather than a 1D viscosity model. Through a FORTRAN user subroutine, each mesh element is given an individual viscosity as the FEM model job is being processed. For more details on how these material properties are determined and assigned per element refer to section 4.3. Having assigned the material properties, all layer parts are brought together in the model assembly. The assembly consists of so called instances, that refer back to their corresponding part. Hence, if a part is altered, so is the dependent instance within the model assembly.

4.2.2. Mesh definition and rotation

4.2.2.1. High resolution partitions

In order to investigate GIA in a specific area rather than on a global scale, a part of the FEM model can be discretised using a higher resolution mesh. In doing so, a boundary is created between low resolution mesh elements in the far field, and high resolution mesh elements that encapsulate the area of interest. The sizing of the low and high resolution mesh elements is dictated by their respective seeding settings. The seeding distance defines the maximum element edge size. This seeding distance is projected onto the edges of the Earth layer partitions. With this, one is able to specify the high resolution seeding distance in both radial and planar distance. For geometrical convenience, the high resolution area is defined by a certain angular radius around the pole located at the negative end of the y-axis of the model. With the exception of the lower Earth, all layer instances are partitioned along the conical boundaries that describe the polar circle radius.

(a) Partitioning along the Cartesian planes.

(b) Partitioning along the conical boundaries described by polar radius α.
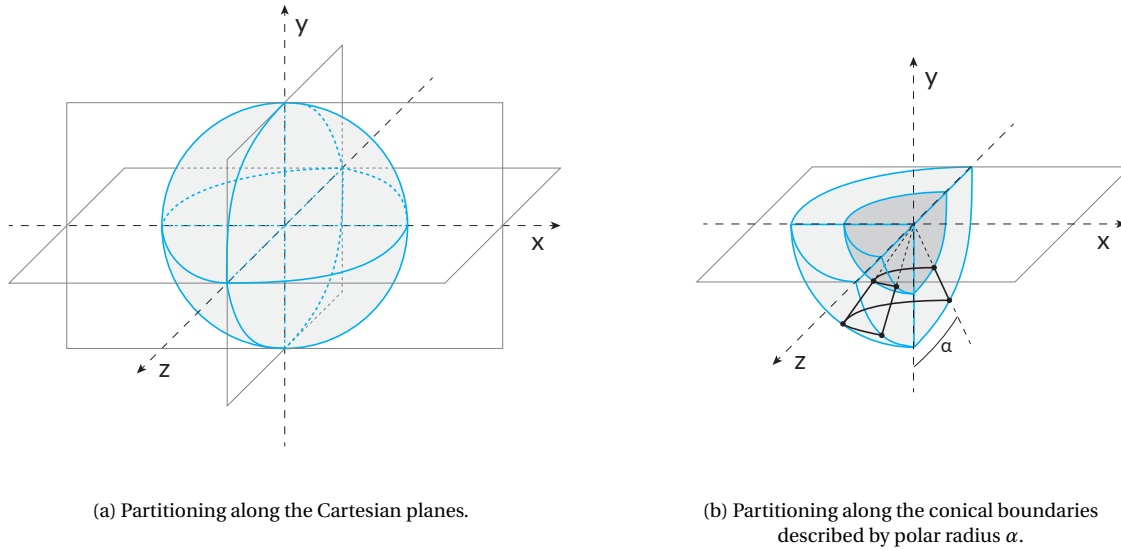
Figure 4.2: Partitioning of the model for future meshing.

This is depicted in the example in figure 4.2b. Here, the polar circle radius is defined as angle α. This example features two layers, and displays two out of eight partitions of both layers. The boundaries of these partitions are shown by the solid blue lines. In order to partition the outer layer, the layer is cut at the solid black lines connecting the intersection between the polar radius cone and the boundaries of the layer partitions.

Note that it is also possible to generate a similar conical partition at the opposite pole of the model. Without such intervention, the elements around this pole will take on a relatively narrow shape using the preferred mesh settings presented in the next section. This could potentially result in unexpected behaviour of the FEM solution at this location. As this area is however located on the very opposite side of globe relative to the area of interest, it is not deemed to exert a significant effect on GIA at this area of interest.

4.2.2.2. Mesh generation

It should be noted that the FEM software finds its own optimal solution for the generation of the mesh. It is however possible to provide Abaqus with guidelines on how to construct the mesh elements. An example of such guidelines are the edges that have been created by partitioning the model in the Cartesian coordinate system planes. Additionally, the shape of the elements and the meshing technique determine the characteristics of the generated mesh.

Abaqus allows for three types of 3D element shapes, being tetrahedral, wedge-shaped, and hexahedral (Abaqus 3DS SIMULIA, 2015a). Figure 4.3 shows an overview of these shapes. The wedge and tetrahedral elements are well suited for usage on complex geometries. These types of element can however be overly stiff, which can be compensated for by using a very high resolution mesh. The hexadral elements do not suffer from this types of behaviour and can provide a less costly yet accurate meshing solution. It should be noted that it is preferred to attain a near-rectangular element shape, as this minimises the sensitivity to its initial geometry. Also, it is advised to use "well shaped" elements, as this leads to improvement of convergence and accuracy. With this, the hexahedral mesh shape is preferred as it allows for an accurate yet relatively low-cost meshing solution. In addition, the hexahedral elements can attain a simple geometry within the shelled layers of the Earth FEM model.

By setting the element shape to hexahedral-dominated (hex-dominated), a combination between hexahedral elements and wedge-shaped elements can be made. The latter are only allowed to be present in some transition areas. For the Earth FEM model, such regions can be found at the poles only. Due to the partitioning performed in the three Cartesian planes, mesh elements that are in direct contact with the poles can only be described by triangular prisms.

The swept meshing technique, in combination with the hexahedral-dominated elements, is required to emulate a regular grid on the outer layers of Earth model. This meshing technique is displayed in figure 4.4b. To clarify the impact of this meshing technique, the result for the structured meshing technique is included in figure 4.4a. The model considered here is a simple dummy sphere that has been partitioned in
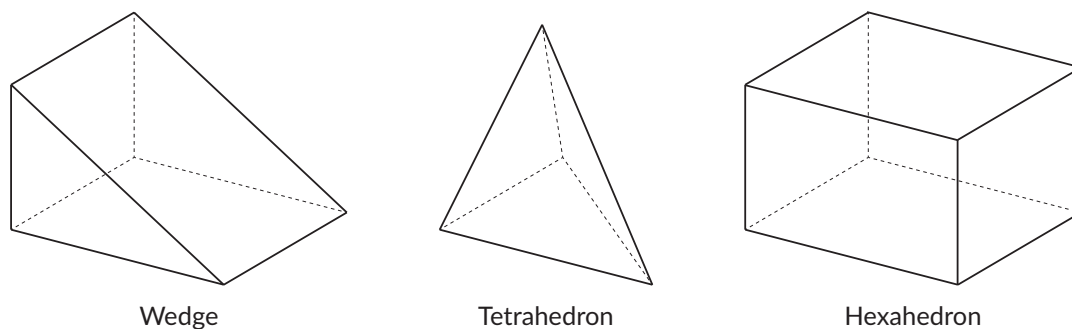
Figure 4.3: Available three-dimensional element shapes in Abaqus.

the three Cartesian planes. The element shape has been set to hex-dominated. It can be seen that shaping and placement of the elements when using the structured technique is relatively arbitrary and irregular when compared to the swept meshing technique. It is evident that there is no straightforward method available to include a high resolution area in the structured model.

Note that structured meshing is still used in the Abaqus FEM model, albeit on the core only. As was explained in section 2.1, the outermost part of the Earth's core is liquid. Due to this fact, and the notion that the deformations deep within the Earth are not of interest in this research nor thought to be of significant magnitude, the core is meshed using a coarse, structured mesh.
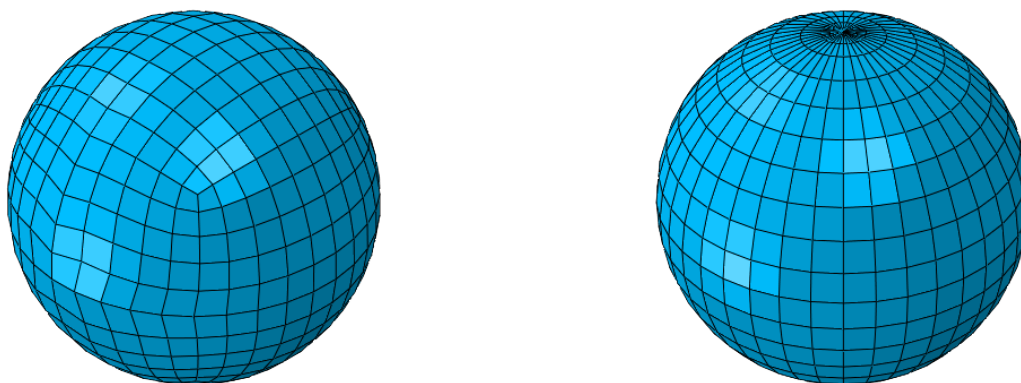
(a) Resulting mesh for the structured meshing technique.   (b) Resulting mesh for the swept meshing technique.

Figure 4.4: Partitioned spherical models after mesh application using hex-dominated elements.

4.2.2.3. Mesh rotation

While the 3D GIA FEM model has initially been created to study GIA on Antarctica, a simple rotation of the model prior to defining the model loading enables the study of other regions. This rotation is an addition made to the original 3D GIA FEM model, and has been developed such that an arbitrary area of interest can be specified.

The high resolution mesh area is rotated to this targeted area of interest after the mesh creation itself is completed. The rotation is performed on the instances in the model assembly. At this point, no physical properties have been assigned to the model yet. Therefore, this rotation will only affect the allocation of the mesh. The rotation itself is defined by entering the desired centre point of the high resolution area after rotation. This centre point is defined by a specific latitude and longitude. The selected location used in this research, is detailed in section 5.4.3.2.

4.2.2.4. Element types

Finally, the element types used in the created mesh are defined as first-order hybrid. When modelling (near) incompressible behaviour, hybrid elements must be used. Regular elements use the nodal displacements to compute the volume and consequently the pressure stress of an element. This method can not be applied

to incompressible materials, which dictate that its volume does not change when subject to a specific load. Hybrid elements allow for the automatic addition of a degree of freedom in order to determine the pressure stress directly.

First order elements are used in order to limit the computation time required. For first order elements, interpolation is performed at the corners of each element. While it is possible to extend the number of interpolation points for an increase in accuracy by including mid-side nodes, this would yield a more computationally expensive FEM.

It should be noted that it is preferred to apply full-integration rather than reduced-integration. The integration setting determines the amount of points used in the Gaussian quadrature/integration of the stiffness matrix of each element (Abaqus 3DS SIMULIA, 2015a). In reduced-integration, a lower-order integration is applied which again corresponds to a less costly analysis in terms of run time. Both types of integration suffer from unique complications. First-order reduced-integration elements are known to suffer from hourglassing. This uncontrolled distortion of the mesh can occur when the strains computed at the only integration point available are equal to zero. Even though these first-order reduced-integration elements are complimented with built-in hourglass control, they require a very fine mesh in order to yield accurate results. Fully-integrated first-order elements can conversely suffer from shear and volumetric locking. This locking can result in overly-stiff behaviour. Abaqus autonomously applies the selective use of reduced integration on volumetric terms, through which locking can be largely prevented. With this, full-integration elements are preferred over reduced-integration elements.

4.2.3. Load application

4.2.3.1. Step and load definition

In order to apply the surface loads to the Earth FEM model, first the time steps should be defined. In this section no specific moments in time will be selected, rather a description of the definition of time steps within Abaqus and the Earth FEM model is provided. For selection of the time steps, refer to section 5.1.3.

The model relies on the important assumption that the Earth model is in a state of isostatic equilibrium at the initial moment in time t_0. Hence, the representation of this moment in time in the Abaqus FEM model, leads to an initial load of zero. The loading at all consecutive moments in time follows from the difference between the instantaneous and the initial load. This is shown in the simplified representation of the time steps and subsequent loading in figure 4.5a. Here the loading provided at certain times t is shown in blue dots.

The load that is applied at time t_3, will be active throughout step 3, and is hence applied in the interval between t_2 and t_3. Using the default Abaqus settings, the grey shaded areas indicate the constant loading applied at all increments within the full duration of each time step. Due to the temporal variation of the total surface load, a new load is defined for every time step. Note that Abaqus propagates such new loads to all following time steps, meaning that there is a need for deactivation of the loads that apply to all preceding time steps.
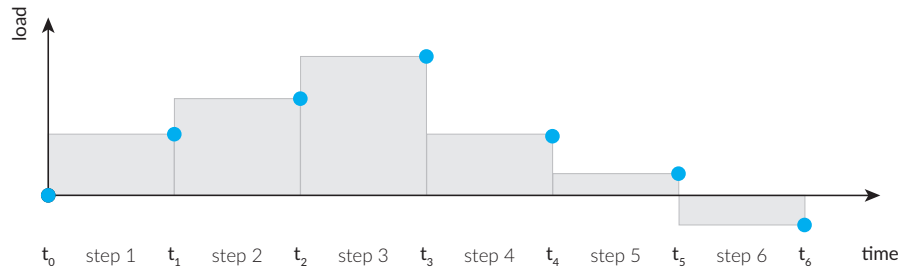
(a) Default load application.
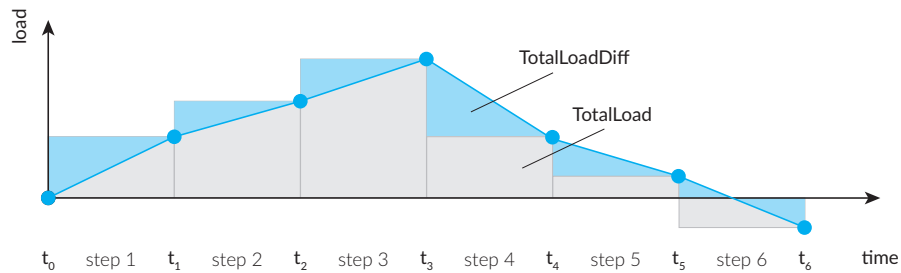
(b) Ramped load application.

Figure 4.5: Schematic representation of stepped load application in Abaqus.

By enabling ramp-loading through the Abaqus procedure referred to as tabular amplitude definition (Abaqus 3DS SIMULIA, 2015a), a linear interpolation between the known instantaneous loads is performed. This is represented by the solid blue line in figure 4.5b. The shaded blue areas indicate the additional loading applied in order to either reduce or increase the total load applied at the surface in accordance with the so-called ramped load. The inclusion of ramp-loading allows for a more accurate representation of gradual glaciation and deglaciation using less time steps when compared to the default stepped load application. It should however be noted that the time steps should be selected such, that all characteristic ice sheet maxima, minima, and rates of ice mass change are captured by the linear load approximation over time. Overall, this enables the usage of a limited amount of time steps and thereby a limited amount of computation time.

The total surface load is the sum of the glacial and the oceanic load. The glacial load follows directly from the ice height input as described in section 5.1, whereas the total oceanic load is derived from the total ice mass loss or gain over a single time step. This oceanic load is valid for the first iteration only, and is revised in the processing of the FEM deformation output. The theory behind the sea level equation that is used to determine the oceanic load at all following iterations, is described in section 3.2. A detailed description of the numerical procedure followed to compute and revise this oceanic loading, is included in section 4.4.2.

4.2.3.2. Centre of gravity correction

The Abaqus FEM model is defined with respect to the reference origin, referred to as the Centre of Figure (CoF). The introduction of loads onto the surface of the Earth, yields a shift of the Centre of Mass (CoM) of the body. This shift is described by vector $\overrightarrow{r}_{CoM}$. While the centre of the FEM model will remain fixed at the CoF, it is desirable to perform all computations with respect to the shifted CoM. In order to achieve this, a correctional load is applied to the model through equation 4.1 (Blank, to be published) (Paulson, 2006). This correctional load emulates the shift of the CoM, while all FEM computations are still performed with respect to the CoF. Note that in this context, the Centre of Mass and Centre of Gravity are located at the same point in space. As such, these terms are used interchangeably in the remainder of this report.

$$\sigma_{CoM} = -\overrightarrow{r}_{CoM}\Delta\rho\cos(\gamma) \tag{4.1}$$

Following the definition of Klemann and Martinec (2011), the gravitational field can be used to compute

the exact shift of the CoM $\vec{r}_{CoM}$. Angle γ can be determined by formulating vector $\vec{r}_{CoM}$ in terms of latitude and longitude, and computing the great circle angular distance on a sphere between this CoM and an arbitrary point. The term $\Delta\rho$ in equation 4.1, represents the density contrast encountered at the layer interfaces at which the correctional load is applied.

Klemann and Martinec (2011) suggest that it suffices to correct for the movement of the CoM at the surface of the Earth and at the CMB, where the density contrast across layers is largest. This procedure is adhered to in the initial CoG correction, performed by calling the `Initial_CoG_correction.py` file during model build-up dictated by the `model_gen.py` file. In further iterations, the CoG correction can be applied to all internal layer boundaries. As the full gravity field will already be computed at all layer boundaries in order to solve the SLE, no additional expensive computations are required for a more comprehensive CoG correction. The correctional loads are administered to the FEM model in a fashion similar that to all other (surface) loads previously discussed.

4.2.3.3. Integration accuracy

The intervals between times t define the time steps. These time steps are automatically split in to smaller time increments as Abaqus analyses the FEM model. The minimum and maximum allowable increment time is determined by the user and ensures that the amount of increments suffices to yield accurate results in an acceptable amount of computation time. The model used in this research, determines the minimum and maximum increment time as a fraction of the step time as follows: $t_{\mathrm{inc,\,min}} = t_{\mathrm{step}}/1E6$ and $t_{\mathrm{inc,\,max}} = t_{\mathrm{step}}/25$.

An additional setting that determines the exact increment time, is the creep strain error tolerance (CE-TOL). The relation between stress and strain for a non-linear viscoelastic Earth rheology has been described in section 2.2.3, and its further implementation will be discussed in section 4.3. The CETOL defines what the maximum allowable creep strain error is between the start and end of an increment. The increment time is adjusted such that this error does not exceed the tolerance value, that should be in the order of σ_{err}/E. Here σ_{err} is the allowable error in the stress and E is the elastic modulus. For the model used in this research, the CETOL is set to 1E-5 as recommended by Blank (personal communication).

4.2.3.4. Layer interaction definition

In order to account for the buoyancy interaction between the layers of the FEM model, a so-called Winkler foundation is included at the boundaries between the layers. This boundary condition is in accordance with Wu (2004), and is represented by an elastic spring. Its stiffness follows from the product of the difference in density across the layer interfaces, and the local radial gravitational acceleration.

4.3. Implementation of a 3D composite rheology

After the FEM Earth model has been successfully generated, it can be saved in the Abaqus model database file format (.mdb). Included in this model database are the instructions for the completion of the FEM analysis, referred to as job. An important part of this job is the inclusion of the 3D composite rheology discussed previously. The steps taken to accomplish this as the Abaqus job is running are discussed in this section.

4.3.1. Composite rheology subroutine

As mentioned in section 4.2.1, it is possible to assign material properties to specific elements on an individual basis. This is done through a so-called user subroutine that is called at all element integration points. This user subroutine is executed for all Earth layers that have been manually altered from their default viscoelastic setting, to creep. All other layers adhere to their predefined one-dimensional material properties. The exact properties of the layers that do follow a 3D composite rheology are specified in section 5.2.

The subroutine ensures that the material behaviour of each element is in accordance with the composite rheology flow laws that have been introduced in section 2.2.3. The procedure followed and the scripts involved in the computation of the exact creep parameters per element are shown in figure 4.6 below. Using the unique identifier of the elements and their associated nodes, the location of these nodes is extracted from the model database using the `Element_list_print.py` PDE script. The manually run Matlab script `ComputeCentroidElementLocation.m` is used to compute the three-dimensional position of the centroid of all elements. Through the interpolation of a thermal model of the interior of the Earth, the temperature at the centroid of each element is computed. This temperature is assumed to be constant throughout the entire element. The rheological settings for grain size and water content, along with the temperature, determine the final value for the creep parameters B_{diff} and B_{disl}. These values are saved in the `e.dat` file. This file will serve as an input for the user subroutine.

Table 4.3: Additional model files used for implementation of a 3D composite rheology

File	Type	Main function	Output
e.dat	Input	Contains dislocation creep and diffusion creep parameters for each finite element.	N/A
Element_list_print.py	Process	Extract element numbers, associated nodes, and x-y-z coordinates of said nodes.	Element_list.dat, Node_list.dat
Element_list.dat	Input	Contains list of element numbers and numbers of nodes confining each element.	N/A
Node_list.dat	Input	Contains list of node numbers and associated x-y-z coordinates.	N/A
ComputeCentroidElementLocation.m	Process	Determine the x-y-z location of each element's centroid.	Element_centroid_list.txt
Element_centroid_list	Input	Contains list of element numbers and associated x-y-z coordinates of their centroid.	N/A

Note that further simultaneous development of the 3D GIA FEM model by Weerdesteijn (2019) has resulted in a more efficient workflow for the determination of element specific creep parameters. This adaptation yields a more user friendly procedure, in which the extraction of all element details and the computation of their centroids are performed using the Abaqus PDE without the intervention of the user. While this adaptation has not been implemented in this research, it is recommended to combine the model adaptations by Weerdesteijn (2019) and those realised in this study.
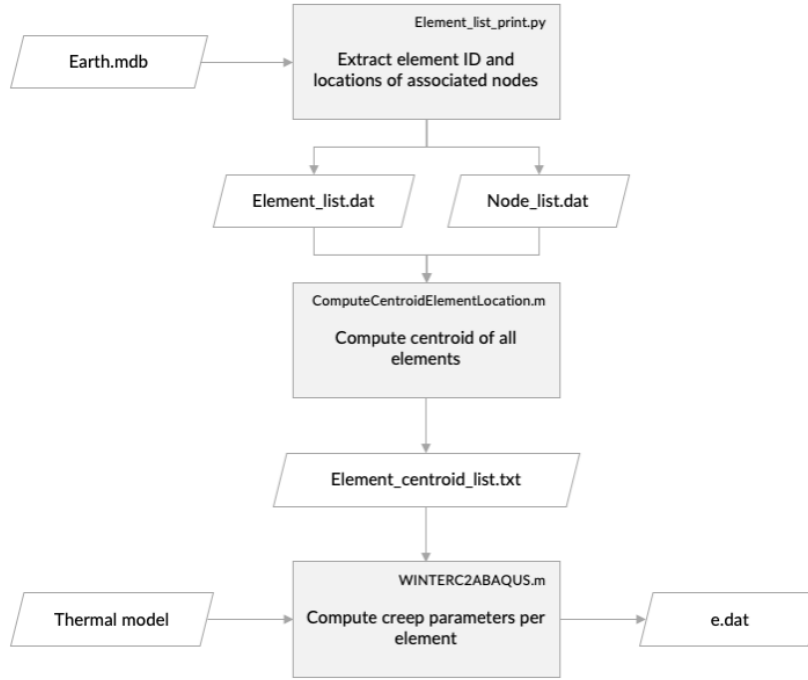
Figure 4.6: Flowchart describing the procedure followed in the computation of element specific creep parameters.

The user subroutine is a FORTRAN script that calls on the two Abaqus subroutines UEXTARNALDB and CREEP (Abaqus 3DS SIMULIA, 2015b). Such subroutines are partially predefined and are to be altered by the user for their specific purpose. This predefined setup is called the user subroutine interface. The UEX-TERNALDB subroutine is used to read the `e.dat` file, containing all element numbers and associated creep parameters. The CREEP subroutine is used to determine the creep strain increment, which may be a function of the equivalent pressure stress, the equivalent deviatoric stress, and any other user defined variables. For a composite rheology, the creep strain increment $\Delta\epsilon$ after increment time Δt follows from equation 4.2 below (van der Wal et al., 2013).

$$\Delta\epsilon = B_{\text{diff}}q\Delta t + B_{\text{disl}}q^n\Delta t \qquad (4.2)$$

Here, the creep parameters B_{diff} and B_{disl}, and stress exponent n are supplied by the user. The von Mises stress q and the increment time Δt are variables that are passed in from the Abaqus FEM analysis. The computed creep strain increment is fed back to the Abaqus analysis, where it is used in further processing of the FEM job.

4.4. Solving the sea level equation

After completion of the Abaqus job, further processing of the FEM analysis is conducted in the `iter_ult.py` script. The results of the FEM analysis are saved in the output database, or .odb file. The main focus of this section is the processing of the output database for further usage in the SLE module. Whilst the theory defining the sea level equation has been discussed previously in chapter 3, this section focuses on the steps taken to solve the SLE. Firstly, the processing of the output data resulting from the FEM analysis is discussed in section 4.4.1. Next, the iterative numerical algorithm that is used to solve the SLE using this processed output data is elaborated on in section 4.4.2.

4.4.1. Abaqus output data refinement
4.4.1.1. Interpolation over an irregular grid
As described in section 4.2.2, the ABAQUS mesh is reallocated such that the high resolution focal area no longer covers the South Pole, but rather Northwestern Europe. A consequence of this rotation is that the location of the mesh nodes no longer resemble a regular latitude-longitude grid. This can be observed from

figure 4.7, where the nodal locations for both the original and rotated case are depicted on a two-dimensional grid. Deformation data is extracted from the output database at these nodal points, after which this data is interpolated onto a finer regular grid corresponding with the resolution of the ice input. This interpolation is required for SLE computations at a later stage. As the initial 3D GIA FEM model SLE module expects the deformation data on a regular grid, modifications are required to successfully interpolate this data onto the regular target mesh. The modifications and interpolation routines considered are discussed in this section.
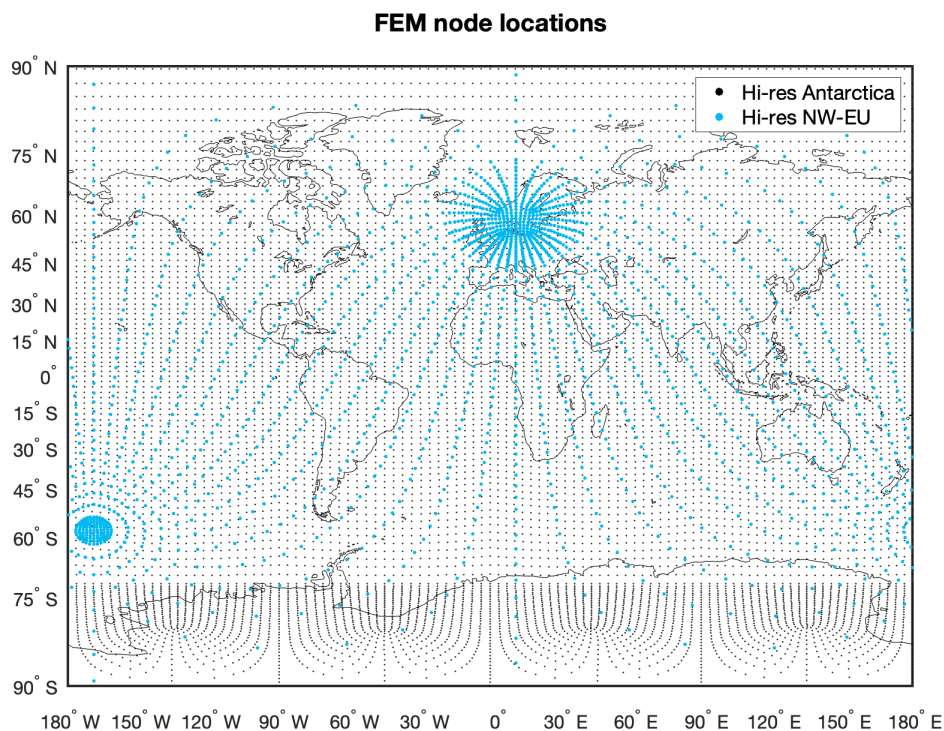
Figure 4.7: Location of Abaqus nodes for the original GIA FEM model focusing on Antarctica, and the adapted GIA FEM model focusing on Northwestern Europe.

4.4.1.2. Griddata interpolation

The original 3D GIA FEM model Python subroutine `sph_tools_TPW7_1SLE.py` uses the `block_gen1` function to interpolate the deformation data from the ABAQUS output mesh to the target mesh. The default interpolation routine used is the `scipy` function `griddata`. The `griddata` function is designed to interpolate unstructured D-dimensional data to a set of sample points as defined by the user. In the original 3D GIA FEM model the method of interpolation is set to linear. As deformation data is interpolated on a two-dimensional latitude-longitude grid, measures are taken to ensure that the deformation along all longitudes at the two poles and along all latitudes at the 0° meridian are consistent. In order to ensure continuous deformation across the 0° meridian, the raw outputted data is complimented with replica data on either side of the meridian. For example, raw data that is available at 5° longitude, is used to create a synthetic nodal point at 365° longitude. Additionally, the deformation that can be found at the minimum and maximum latitude is used to create two arrays of synthetic nodes across all longitudes at the south and north pole respectively.

4.4.1.3. Barymetric interpolation

An alternative to the `griddata` routine has been proposed by Blank (personal communication). This barymetric interpolation is better equipped to interpolate deformation data on a sphere, rather than a two-dimensional grid. The barymetric interpolation routine identifies the three closest nodes that enclose a sample point on the targeted regular grid on the surface of a sphere. This is shown in figure 4.8a. The proximity of the nodes is computed using the great-circle distance, meaning that no intervention is required to interpolate at sample points close to the poles or 0° meridian, as is the case for the 2D griddata approach. Using

the Python routine `Node_list_print.py`, the locations of the nodes are extracted from the ABAQUS output database. Next, the Matlab routine `ConvertNodeLocationList.m` identifies the three closest nodes, and assigns them a weight between 0 and 1 based on the location of sample point. The weights are computed such that the hypothetical barycentre of the three nodes coincides with the location of the sample point. This means that one of the three closest nodes can be assigned a weight of 0, given that the sample point lies in between the two remaining nodes. This scenario, in which node b is assigned a weight w_b of 0, is depicted in figure 4.8b. The deformation at the sample point u_{sample} follows from the weighted average of the deformation at the nodes as follows:

$$u_{sample} = u_a * w_a + u_b * w_b + u_c * w_c \tag{4.3}$$

| (a) Three irregularly spaced nodes enclose the sample point. | (b) Special barymetric interpolation scenario in which node b is assigned a zero weight. |
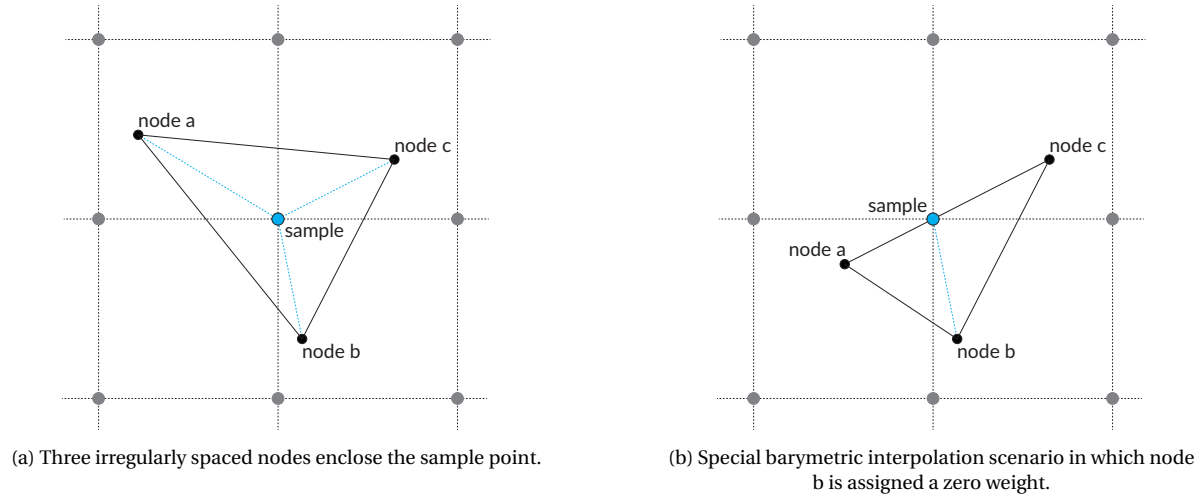
Figure 4.8: Schematic overview of irregularly spaced nodes and sample point on regular grid in the barymetric interpolation routine.

4.4.1.4. Interpolation performance comparison

In order to select a preferred interpolation routine, a comparison is made between the interpolated surface deflection at the simulated present time obtained through both the griddata and barymetric interpolation routine. The results for both routines have been depicted in figure 4.9 and are generated using the 1D BR setting as described in section 5.7. The deflection plotted here is an absolute result with respect to the initial equilibrium state of the FEM model.

It can be observed that both routines provide a smooth output in the high resolution region. Here the nodes of the elements at the surface, indicated with white dots, are located closest to one another. Note that the barymetric interpolation routine is roughly 1.5 to 2 times as computationally expensive compared to the griddata routine. It is evident that both routines suffer from the thinly dispersed nodes outside of the high resolution area. While the barymetric interpolation better confines surface movement in high-latitude regions such as Greenland and the Barents Sea, the barymetric interpolation however also introduces sharp transitions in between the sparsely spread nodes. This is most visible at latitudes greater than 75°, and within Greenland. This behaviour is unexpected and undesired, and is not showcased by the interpolation of deformation data that has been generated on a non-rotated regular grid (Blank, personal communication). As such it is expected that the barymetric interpolation routine is not yet suited for interpolation of irregularly spaced data, due to an unknown error at the time of writing. Therefore, the griddata routine is the preferred method for interpolation of the irregularly spaced Abaqus output data to a regular grid for further processing in the SLE module.
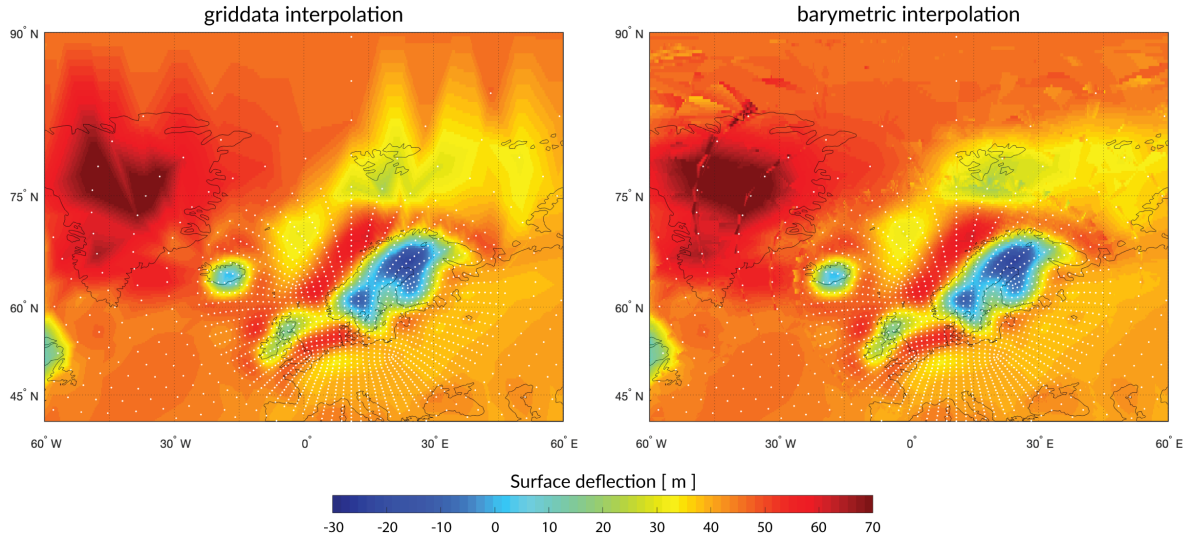
Figure 4.9: Deflection at final time step, a using the linear griddata interpolation routine (left) and the barymetric interpolation routine (right).

4.4.2. Iterative numerical algorithm

In order to solve the GSLE in equation 3.8, a priori knowledge of the topography and ocean function at the onset of loading is required. This calls for an iterative procedure over the entire glaciation-deglaciation cycle until the estimate of the initial topography $T(\theta, \psi, t_0)$ converges. In this section, the numerical algorithm executing this iterative process as adopted by Blank (to be published, personal communication) is detailed. Note that this section is limited to an explanation of the algorithm on a conceptual level.

A flowchart for the numerical SLE algorithm, or module, is provided in figure 4.10. The overall goal of this module is to solve the sea level equation and determine the topography at all simulated time steps. These time steps, each denoted by j, are part of the cycle of glaciation and deglaciation, referred to as the full glacial cycle. The iterative procedure is executed across this full glacial cycle. Each iteration is denoted by k. The solution of the SLE module will be used to perform a correction of the loads administered to the FEM model.

First, the spatially variant sea level change is computed through equation 3.5. In order to do so, both the spatially variant change in the geoid $\Delta \mathcal{G}$ and the displacement of the solid surface are required. The Abaqus FEM analysis outputs the displacements at all layer boundaries. In accordance with Wu (2004), the radial displacements are decomposed into spherical harmonics. This decomposition is used to solve the Laplace equation and determine the gravitational potential ϕ_1. The gravitational potential in its turn is divided by the gravitational acceleration g_r, after which the change in geoid is obtained. As these values follow directly from the Abaqus FEM output, these computations are not part of the iterative procedure discussed next, but rather serve as a preparation for the computation of the spatially varying sea level change.

The SLE module is initiated by assuming that the topography across all time steps in the full glacial cycle is equal to that of the present day. Next, a check is performed to select the appropriate time step t_c at which the overall sea level equation convergence test will be performed. This check is performed due to the fact that in some glacial models, the ice load at the onset of glaciation is identical to the ice load at the end of glaciation (present time). Combined with a small deflection, the convergence criterion could be met in the first iteration, preventing further refinement of the topography and SLE. Hence, a convergence time step t_c will be selected at which the time to the final time step t_p is maximised, and there is a sufficiently large difference in surface loading.

At this point, the topography, the displacement of the solid surface, the spatially variant change in geoid, and the input loading are known. With this, it is possible to compute the ice-free ocean function, the shoreline migration projections, and the spatially variant sea level change. The shoreline migration projections are denoted RO for change in bathymetry, and TO for change in basin size (Kendall et al., 2005). These values can be used to compute the revised ice load, which consists of all land based and grounded marine ice masses. The spatially invariant sea level change is a function of this revised ice load as well as the shoreline migration projections. The spatially invariant sea level change is solved for through a spherical harmonics decomposition.
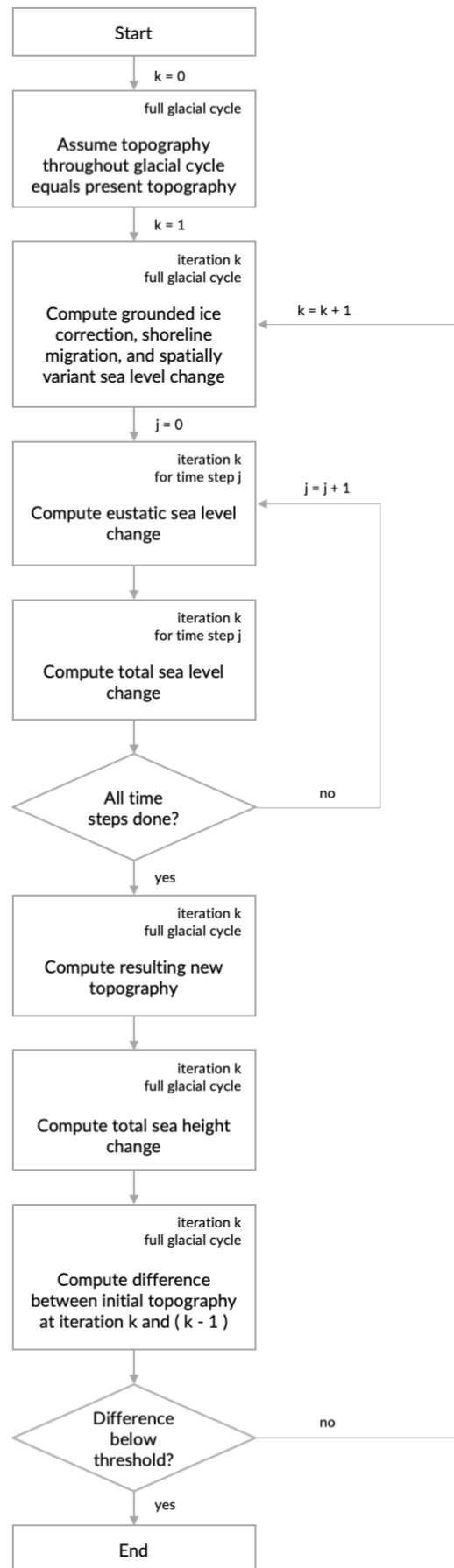
Figure 4.10: Conceptual flowchart of the iterative numerical algorithm used to solve the SLE. After Kendall et al. (2005), figure 4 and Blank (to be published, personal communication).

The summation of the spatially variant and invariant sea level change result in the total sea level change at each time step j. Note that this procedure is part of the inner loop, shown in figure 4.10. After all time steps have been processed, the iteration procedure is continued by computing the resulting new topography and total sea height change across the full glacial cycle. Lastly, the difference between the topography at the convergence time step t_c between iterations k and $k-1$ is computed. In case this convergence criterion meets the threshold, the iterative procedure is completed. If not, the newly computed topography is used as an input for the next iteration. The convergence threshold for the topography at time t_c typically equals 1E-4 (Kendall et al., 2005).

4.4.3. Revision of the surface loading

After completion of the SLE module, the iterated oceanic loading is used to revise the total surface loads applied to the Abaqus FEM model. These revised surface loads will be used in the Abaqus FEM analysis in the following model iteration. As was mentioned in section 4.2.3.2, the gravitational potential ϕ_1 is required to compensate for the dislocation of the CoG. This gravitational potential has been computed and saved in order to solve the SLE, and hence is now available to compute the load required to compensate for movement of the CoG at every density transition within the Abaqus FEM model.

4.4.4. RSL output definition

The SLE module computes the ΔSL at the end of each time step on a regular global grid, and saves the obtained data in the `RSL.dat` file. The computed sea level is relative to that established at the initial time t_0. Hence, to obtain the RSL with respect to the present day, the ΔSL computed at the present time t_p is subtracted from the ΔSL at all time steps. RSL curves for a specific site are acquired by interpolating the previously obtained global RSL grid to the coordinates of the selected location. The interpolation used is a simple linear interpolation.

With the ΔSL available on a regular global grid at every time step, it is also possible to construct relative sea level change rate maps, such as presented in section 3.2.2. These RSL change rate maps are constructed through linear derivation between two time steps. The analogous procedure followed to determine uplift rates rather than RSL change rates is detailed in the following section.

4.5. Uplift rate output definition

In this section, a brief overview is provided of the additional steps taken in order to acquire the desired uplift rate output. This requires the addition of a final time step in to the near future.

At every time increment, the translational and rotational displacements at the nodes are computed and saved as Abaqus variable U. It is possible to also request the translational and rotational velocities V at the nodes as a model output. However, it is not clear whether this velocity is determined at the instantaneous end of a time increment, or at the mid-way point between two increments. Hence, an alternative method is preferred in order to negate this ambiguity. As such, it is proposed to add a final time step in simulation, that extends beyond the present time into the future. The ice load used for this future step, is set equal to that of the present time. Using the linear derivative of the displacements computed at the present and future time steps, a near-instantaneous uplift rate can be computed.

The time interval between the present and future time step should be chosen sufficiently long such that a noticeable and realistic further deformation can occur, and sufficiently short such that no excessive relaxation occurs. In order to determine what time interval fits this description, a sensitivity test has been performed with three additional future time steps, being present+1, present+10, and present+50 years. Note that by default, the model will treat the future time step like any other. This means that the SLE module will account for a changing sea level between the present time and future time. This implies that the total ice load between the present and future time remains unchanged, while adjustments of the oceanic loading distribution do occur. While the possibility exists to filter out the elastic response to this changing sea load between the present time and future time, this is not applied in this test nor the remainder of this research. As is detailed in appendix A, the effect of this elastic filtering is negligible. Additionally, it is deemed realistic that the present day GIA response of the solid Earth includes an elastic component due to rearranging of oceanic loading on the surface.

The model settings for the sensitivity test are summarised below, in Table 4.4. Note that due to an unforeseen error, the 3D viscosity in this test was assigned to the wrong elements. Hence, while this model includes a 3D composite rheology, it is not a realistic representation of the Earth's interior. Additionally, excess ice was

present in Scandinavia at the start of the simulation. Both this disturbance of the equilibrium state as well as the incorrect Earth interior invalidate the results of this test. Additionally, both errors have been mitigated in all further conducted tests.

Table 4.4: Model settings for future time interval sensitivity test.

Setting	Value
Ice model	Bradley2018
Thermal model	WINTERC
Grain size	4 mm
Water content	Dry
Iterations	1
Global resolution	400 km
Local resolution	100 km
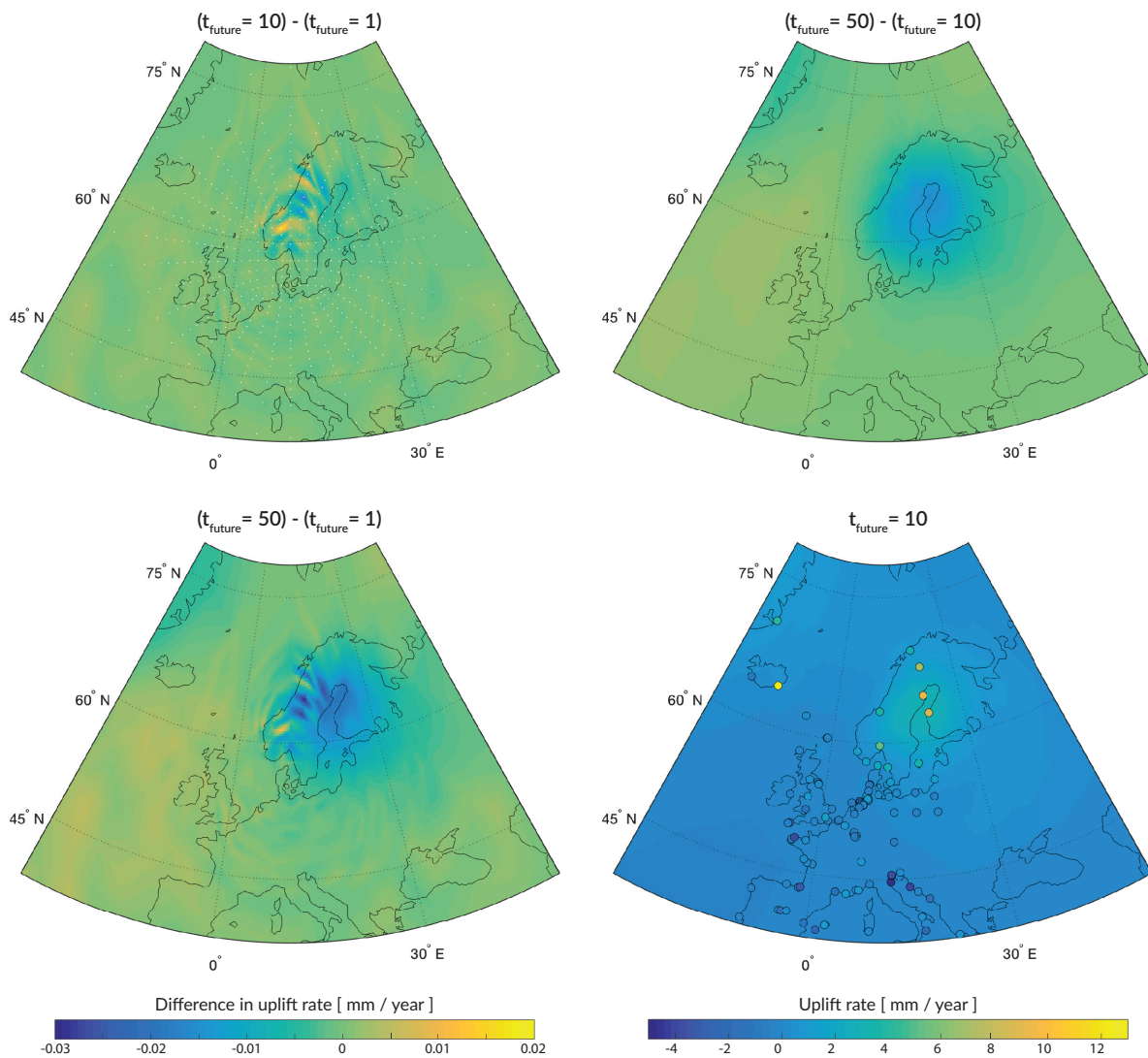
Figure 4.11: Differences in uplift rates determined using two different future time intervals (top, bottom left, using the left colour scale), and uplift rate using a future time interval of 10 years (bottom right, using the right colour scale).

In order to compare the uplift rates that have been computed using the selection of 3 future time steps, the differences between one another have been displayed in figure 4.11. These differences are computed by

subtracting the uplift rate derived at the latest future time step from the earliest future time step.

$$\Delta \dot{u} = \dot{u}_{\text{late}} - \dot{u}_{\text{early}} \tag{4.4}$$

From these figures, three main observations can be made. Firstly it can be seen that all differences between the uplift rates computed using various intervals in Northwestern Europe lie within the +0.02 to -0.03 mm/year range. It should be noted that this is not expected to impact conclusions drawn from any visual analysis op uplift rate maps, and is very comparable in magnitude to the smallest errors anticipated in the GPS observations. More details on these observations are included in section 5.6.

Secondly, significant irregularities are present in top and bottom left frames in figure 4.11, where the differences in uplift rate for the intervals of 10 and 50 years with respect to the interval of 1 year are depicted. These irregularities can be recognised from the small adjacent patches of opposite sign, located near present-day Norway and Sweden. Such irregularities can not be found the top right frame, where the differences in uplift rate for the interval of 50 years with respect to 10 years is shown. As such, it is believed that this patchy behaviour can be attributed to the uplift rate computed using the 1 year time interval. It is suspected that this behaviour arises at the +1 year future time interval only, due to the large difference in step size with all preceding time intervals. In order to investigate the possible origin of this irregular behaviour, the locations of the FEM nodes are included in the top left frame. From this frame it can be seen that the centres of the irregular patches coincide with the locations of the FEM nodes. Also, the boundaries of the patches run between neighbouring nodes. Therefore, it is reasoned that the time interval of 1 year may have introduced faulty behaviour in the FEM analysis due to a large contrast with the duration of the preceding time steps. Possibly, the irregular behaviour is a signature of volumetric locking or hourglassing as described in section 4.2.2. The aforementioned supports the notion that the step size of 1 year into the future is not suitable for uplift rate computations.

Lastly, the plots in figure 4.11 enable the selection of a single future time step that can be used for all uplift rate computations. As the interval of 1 year is deemed to small, the remaining options are an interval of 10 years and an interval of 50 years into the future. From the top right frame in figure 4.11, it can be observed that no irregular behaviour is present, and that the uplift rate using the 50 years interval predicts a lower uplift rate near the centre of the Fennoscandian ice sheet than the uplift rate using the 10 years interval. This implies that the longer time interval allows for more relaxation in this previously glaciated region. As this relaxation contribution is not desirable and leads to an under-estimation of the near-instantaneous vertical surface deformations, the 10 years interval is deemed most suitable for the computation of the uplift rate.

<div style="text-align: right;">

5

</div>

<div style="text-align: right;">

Experimental framework

</div>

In this chapter an insight will be provided in to the setup of the simulations performed in this research. To this extent, first all relevant model settings and input parameters are discussed. These input parameters include the two glaciation histories employed in this research in sections 5.1, as well as the five viscosity distributions detailed in section 5.2, and the present day topography in section 5.3. The model settings, mainly focused on the resolution of the model, are detailed in section 5.4. The remainder this chapter focuses on the data that will be used for comparisons with the generated results of each simulation. To this extent first a collection of 3 RSL databases is introduced in section 5.5, after which a set of GPS-derived uplift rates is detailed in section 5.6. This chapter concludes with section 5.7, in which a comprehensive overview of all tests performed. Here all simulations are given a unique identifier that may be used throughout the remainder of this work.

5.1. Surface loading

In this section, the two ice models used in this research are discussed. The selection of ice models consists of the ICE-6G model discussed in section 5.1.1, and the Bradley2018 model discussed in section 5.1.2. These two models have been selected because all required input data was readily available: the models were either obtained online (W.R. Peltier, 2018), or through personal communication (Bradley, personal communication, April 24 2018). By selecting these two models, the dependence of GIA modelling on the ice model can be accounted for. The selection of ice models is not extended beyond two models in order to limit the total number of simulations within the time available for this study. This section concludes with a discussion of the simulation time steps selected, and the major differences between the two ice models at these moments in time in section 5.1.3.

5.1.1. ICE-6G_C model

The ICE-6G_C model is one of many iterations of the ICE-nG (VMx) model series driven by Peltier and associates (Peltier et al., 2015; Roy, 2017). While early iterations of the ICE-nG models were constrained using only RSL observations, the ICE-6G_C model also employs space geodetic data. Also, the ICE-6G_C model has a higher temporal resolution compared to its predecessor, the ICE-5G model, throughout the most recent 26 ka. The ICE-nG model series have been developed in conjunction with their preferred 1D viscosity profile, being VM5a for the ICE-6G_C model. More details on this specific viscosity profile are included in section 5.2.

It should be noted that the ICE-6G_C (VM5a) model is not the most recent iteration of the ICE-nG model series. Since the initial publication of the ICE-6G_C (VM5a) model by Peltier et al. (2015), two new configurations have been proposed: ICE-6G_C (VM6) (Roy and Peltier, 2015) and ICE-7G_NA (VM7) (Roy and Peltier, 2017). Both configurations were developed in order to yield a higher model performance with respect to RSL and GPS observations on the American continent. The ICE-6G_C (VM6) configuration was later omitted due to newly introduced unacceptable misfits to space geodetic constraints (Roy and Peltier, 2018). The tuning of the ICE-7G_NA (VM7) to observations in North-America, has resulted in a glacial model which, outside of this area, remains unchanged compared to the ICE-6G_C model. Regardless of the study on the applicability of the ICE-7G_NA (VM7) model for the Mediterranean (Roy and Peltier, 2018), some caution should be exercised when considering the application of the ICE-7G_NA model and its predecessors in a GIA model for Northwestern Europe. The seventh generation model is more strongly constraint to local geodetic and

RSL data in Laurentia than the ICE-6G_C model. Additionally, all ICE-nG models are also heavily tuned to the VMx viscosity distributions and vice versa. This could compromise their performance in other regions in conjunction with other viscosity profiles (Bradley, personal communication, April 25, 2018). From this, it is concluded that the ICE-6G_C model is one of two preferred glacial models for this research into GIA in Northwestern Europe. The global ice sheet coverage of this model at 22ka BP is included in figure 5.1.

5.1.2. Bradley2018 model

The Bradley2018 model is a plastic ice sheet model that it is not constrained by RSL data, but rather by geomorphological data (Bradley et al., 2018). The model consists of the combination of a regional model for the British-Irish Ice Sheet (BIIS), the Fennoscandian Ice Sheet (FIS) and the Barents Sea Ice Sheet (BSIS), and far-field models. Indicators used to constrain the BIIS, originated from more than 170,000 datapoints in the BRITICE V2 Geographical Information System (GIS) database compiled by Clark et al. (2017). A similar database, DATED-1 (Hughes et al., 2015), has been used primarily to reconstruct the FIS and BSIS. The DATED-1 GIS database is a collection of published data on the retreat and advance of these ice sheets, and associated geomorphological indicators. The data contained in this database has been translated to ice sheet time-slice maps at four time periods between 40 ka and 25 ka BP, and at every 1000 years between 25 ka to 10 ka BP.

The far-field portion of the Bradley2018 model is the result of a series of iterations of the ICE-3G model. Due to continuous development of the Bradley2018 model, the far-field ice sheet deglaciations have been revised over time, primarily in order to more accurately reproduce the timing of global meltwater pulses (Bradley, personal communication, April 24, 2018). Also, improved regional models have been used to further develop the far-field ice sheets over time. A graphical representation of the extent and ice sheet thickness for the Bradley2018 model at the LGM is given in figure 5.1. Here it is evident that a cylindrical ice loading is applied outside of the regional ice sheets in proximity of Northwestern Europe.
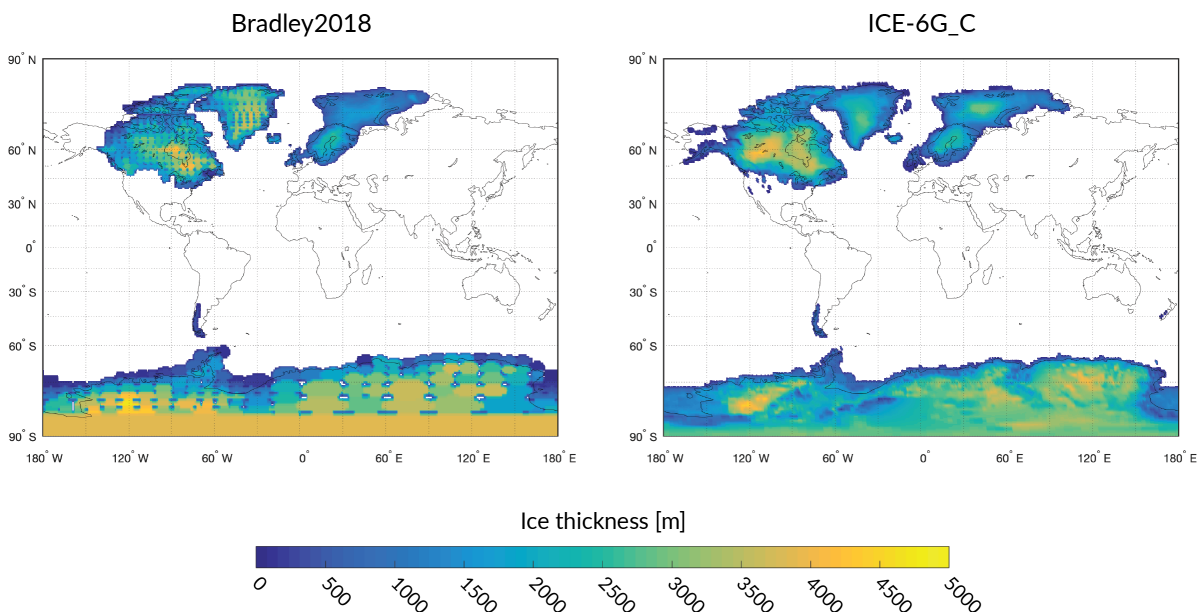
Figure 5.1: Ice sheet extent and thickness for the Bradley2018 model and the ICE-6G_C model at 22 ka BP.

5.1.3. Ice model comparison at selected time steps

The time steps used in all simulations performed are selected such that the latest glacial cycle is fully captured. It is ensured that only those time steps are selected, at which ice height data from both the ICE-6G_C model and the Bradley2018 model are available. Also, an additional time step beyond the present time is included for uplift rate computations as explained in section 4.5. Consequently, the following moments in time

will be simulated after the ice model specific onset of glaciation: [26, 22, 18, 17, 16, 15, 14, 13, 12, 11, 10, 9, 8, 7, 6, 5, 4, 3, 2, 1, 0, -0.01] ka BP. Here ka is defined as 1000 years · 365.25 days · 24 hours · 3600 seconds = 31,557,600,000 seconds.

Note that the ICE-6G_C model goes back to 122 ka BP at which there is no ice present in Northwestern Europe, whilst the Bradley2018 model goes back to 116 ka BP. The Bradley2018 model shows that an ice sheet covering the majority of Norway is present at this earliest available time step. This does not agree with the notion that Scandinavia was ice-free at the start of the last glaciation, with the exception of small glaciers in the Norwegian and Swedish mountains (Mangerud et al., 2011). Hence, in this study, the ice which is present in the Bradley2018 model in Scandinavia at 116 ka BP is removed. By defining the start of the simulation at 122 and 116 ka BP for the ICE-6G_C and Bradley2018 model respectively, the duration of the first time step differs between these two settings. The impact of this discrepancy of 8 ka years is however deemed negligible considering the 90+ ka linear build-up of the ice in the 3D GIA FEM model. Additionally, by adhering to the timing of the onset of glaciation as defined by the two ice models, modifications to these models are minimised.

It is believed that using the aforementioned time steps an accurate representation of glaciation, the LGM, and the following rapid deglaciation can be achieved. Note that the computational cost increases approximately linearly with the amount of time steps selected. This is due to the repetitive processing performed per time step. Adding more time steps is believed to be too costly. In case it is preferred to further limit the number of time steps, it is recommended to decrease the number of time steps in the range between 14 and 8 ka BP where deglaciation can be considered steady. It is possible that such a steady rate of deglaciation can accurately be represented through ramp loading over a decreased number of time steps. The impact of excluding certain time steps should be investigated, as this is not included in this research due to limited resources. It is preferred to maintain the 1 ka year interval in the last 8 ka in order to warrant a sufficiently high spatial resolution for RSL curve reconstruction.

Time in Abaqus is defined to be zero at the onset of any simulation. Any of the following time steps are defined by the amount of time that has passed since the initial moment in time. As such, the following time arrays are defined in the input file in order to comply with this definition:
Bradley2018
[90, 94, 98, 99, 100, 101, 102, 103, 104, 105, 106, 107, 108, 109, 110, 111, 112, 113, 114, 115, 116, 116.01] · ka
ICE-6G_C
[96, 100, 104, 105, 106, 107, 108, 109, 110, 111, 112, 113, 114, 115, 116, 117, 118, 119, 120, 121, 122, 122.01] · ka

Using figure 5.2, a brief comparison can be made between the ice histories as captured by the Bradley2018 and ICE-6G_C model. It can be seen that at 26 ka BP, the extent of the ICE-6G_C model Fennoscandian ice sheet is greater than that for the Bradley2018 model. While at this time the Fennoscandian and Barents-Sea ice sheets are not joined together in the Bradley2018 model, this connection does exist for the ICE-6G_-C model. Additionally, the ICE-6G_C model displays a larger overall ice sheet thickness compared to the Bradley2018 model. The two ice models are however significantly more similar at 22 ka BP. It should be noted that while the Bradley2018 implies ice sheet growth between 26 and 22 ka BP, the ICE-6G_C displays opposing behaviour. Hence, a large difference between the two ice models used in this research exists in terms of the extent and height of the ice sheets at their culmination point and the time at which this maximum is attained.

Additionally, it can be observed that the while the extent of the BIIS in the ICE-6G_C model exceeds that of the Bradley2018, the ice sheet thickness of the latter is generally higher for this particular ice sheet. This is most evident at 15 ka BP.

While not fully depicted in figure 5.2, other noteworthy differences between the two ice models arise in the interval between 22 ka BP and present time. In the Bradley2018 model, the BIIS is separated in to two smaller ice sheets over Scotland and Ireland respectively at 17 ka BP, after which the Irish portion of the ice sheet fully melts after 15 ka BP. In the ICE-6G_C model, no such separation occurs. Rather, the BIIS remains a single entity until fully molten at 11 ka BP. According to the ICE-6G_C ice model, Northwestern Europe becomes ice free at 9 ka BP. Full deglaciation is delayed for the Bradley2018 model, in which Northwestern Europe becomes ice free at 7 ka BP.

Note that both ice models have been interpolated onto a 0.25° degree latitude-longitude grid. The original Bradley2018 and ICE-6G_C model were available at lower resolutions on a 512x1024 and 180x360 grid respectively. The SLE module however requires a certain uniform input resolution. This will be discussed further in section 5.4.
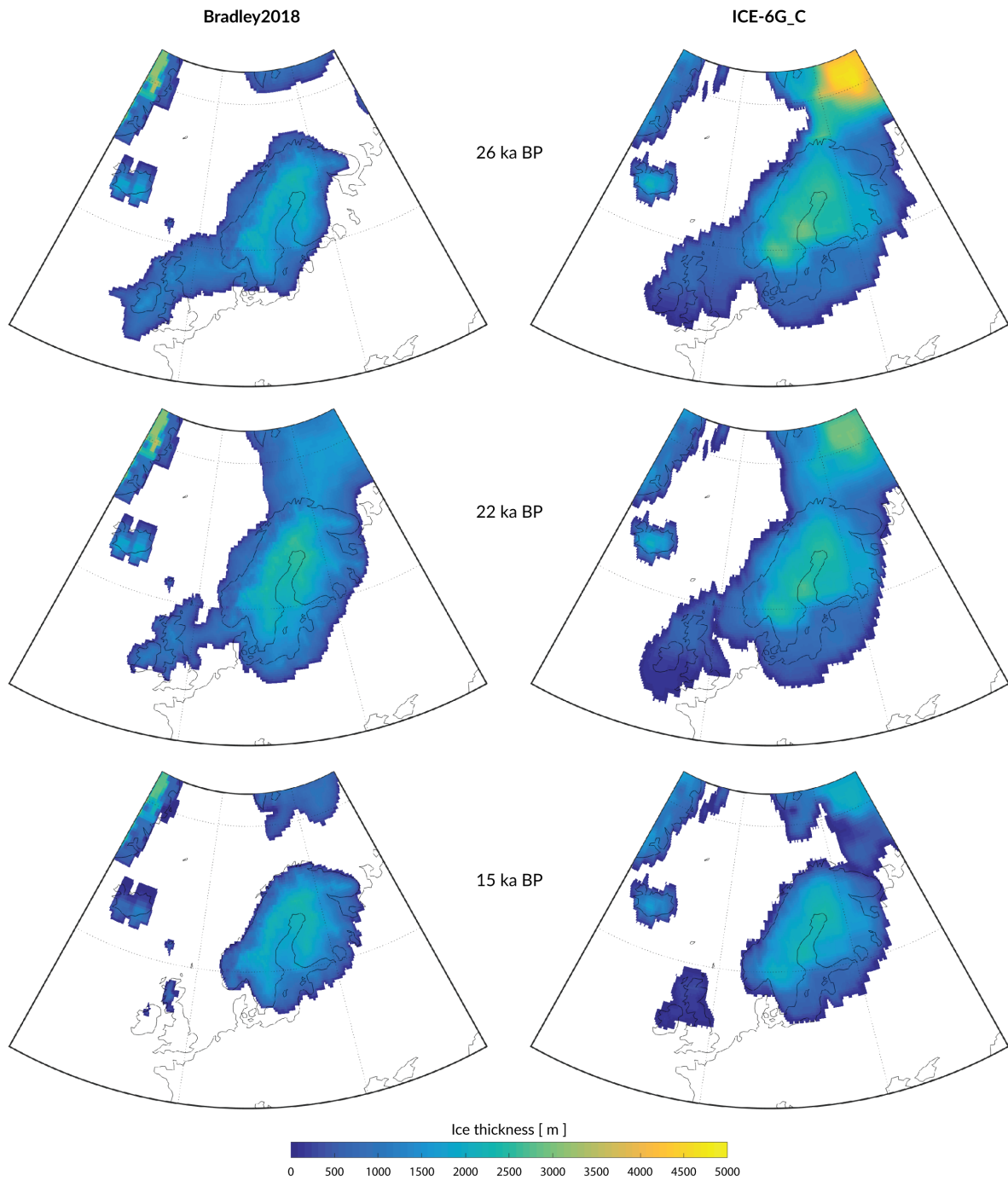
Figure 5.2: Ice thickness at different moments in time for the Bradley2018 model (left) and the ICE-6G model (right).

5.2. Viscosity distribution

5.2.1. WINTERC-3D temperature model

One of the variables required to compute a viscosity distribution within the Earth's outermost layers is the temperature T. A 3D map of the Earth's temperature can be obtained using a wide range of measurement and modelling techniques. Recent efforts however have been undertaken to acquire a single temperature model from the inversion of a multitude of primary data sources. These sources include seismic waveform tomography, satellite gravimetry, surface topography, and geochemical analysis of mantle material samples (Fullea, 2019). The resulting model provides temperature readings at 2 km intervals between 1 and 401 km depth, on a 1-by-1 degree regular latitude-longitude grid.

It was found by Trampert et al. (2001) that seismic velocities are mainly dependent on thermal variations, and are only sensitive to modest compositional variations in the lower mantle. Note however that here composition is defined in terms of volumetric distribution of different types of minerals. Additionally, Faul and Jackson (2005) found that seismic wave attenuation can be attributed to grain size sensitive diffusion. While neglecting the effects of grain size and water content in the interior of the Earth could lead to an overestimation of seismically derived temperatures (Barnhoorn et al., 2011), it is not known whether this is the case for the WINTERC-3D model.

This preliminary temperature model from the WINTERC-3D thermochemical imaging project, will be used as the sole input of temperature data for the determination of all 3D viscosities in this research. Given the previously discussed uncertainty, this represents an important limitation of this study.
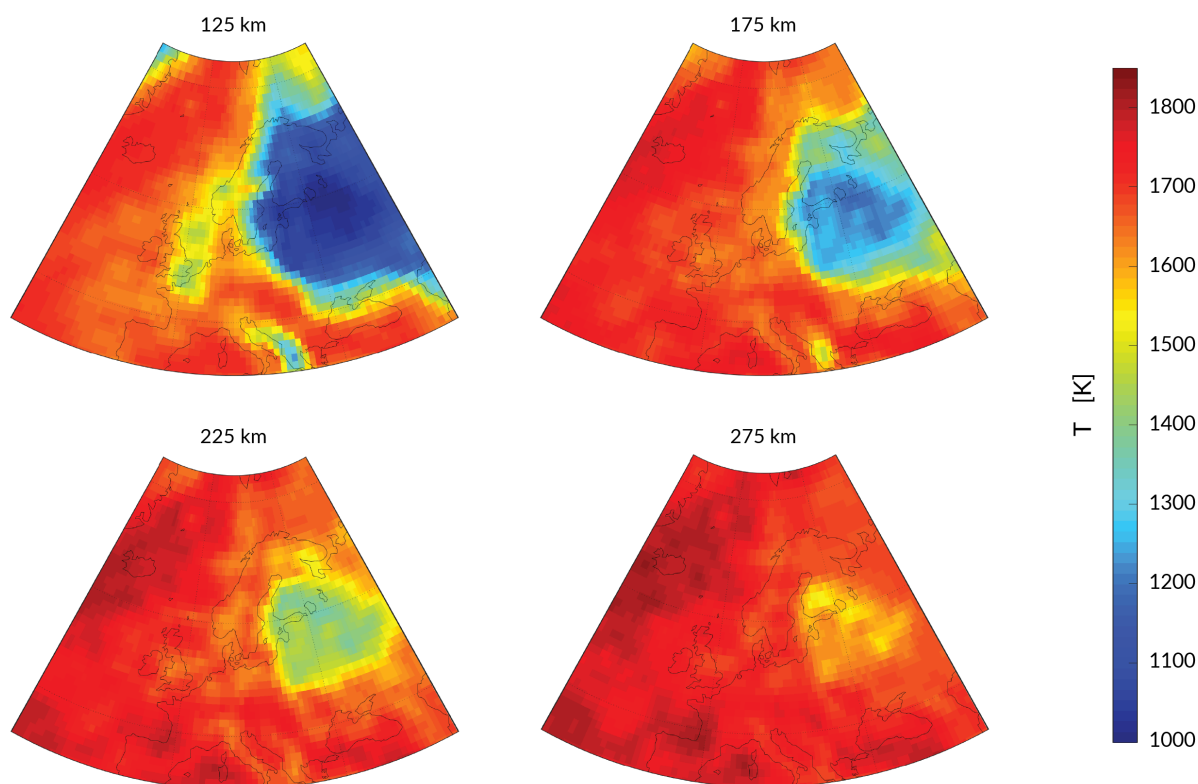
Figure 5.3: WINTERC-3D temperature maps at various depths.

Figure 5.3 includes four temperature maps derived from the WINTERC-3D model at different depths. It can be seen that a distinctive separation exists between hot and cold areas in the South-West and North-East of Europe respectively. This corresponds well with differentiation between the Baltic Shield and its surroundings as discussed in section 2.1.2. Additionally, it can be seen that a significant temperature anomaly exists beneath the North Sea in the shallow upper mantle. This area stretches from West Norway to the north of France, and connects three concentrations of lower temperature at the Channel, the Doggerbank, and West Norway. While the latter two concentrations could be linked to the Central Graben and Viking Graben described in section 2.1.2, no evident link is found between the temperature anomaly beneath the Channel and

the tectonic origin of Northwestern Europe. It could be possible that this anomaly is related to the boundary between the French Variscides in the south and the German-Polish Calidonides in the North. An expected continuation of the temperature anomaly along this boundary in landward direction, is however not present. Hence it is uncertain what the tectonic cause of this temperature anomaly beneath the Channel is.

5.2.2. 1D rheology

The one-dimensional VM5a viscosity model (Peltier et al., 2015) is used in order to perform a comparison between the performance of a 1D rheology versus a 3D composite rheology. This viscosity model has been developed in conjunction with the ICE-6G model, and consists of 6 radially uniform layers. All details required for usage in this study can be found in table 5.1 (Peltier et al., 2015). As was mentioned in section 4.2.1, the crust and core are assigned alternative mechanical properties based on their viscosity.

Table 5.1: VM5a layer data (van der Wal, 2019, personal communication).

Depth range [km]	Density [kg/m^3]	Shear modulus [Pa]	Viscosity [Pa s]
0 - 60	3020.00	0.5376E11	0.10E44
60 - 100	3375.00	0.6750E11	0.10E23
100 - 670	3631.00	0.8852E11	0.50E21
670 - 1171	4514.00	1.7889E11	0.16E22
1171 - 2891	5062.00	2.4005E11	0.32E22
2891 - 6371	10925.0	1.000E-20	0.00E00

5.2.3. 3D rheology

As discussed previously in sections 2.2.3 and 4.3, the effective viscosity is dependent on the creep parameters B_{diff} and B_{disl}, and the von Mises stress q. For convenience, equations 2.3 and 2.7 are repeated here:

$$B = Ad^{-p} f\text{H}_2\text{O}^r \exp\left(\alpha\varphi\right) \exp\left(\frac{E + PV}{RT}\right) \tag{5.1}$$

$$\eta_{eff} = \frac{1}{3B_{\text{diff}} + 3B_{\text{disl}} q^{n-1}} \tag{5.2}$$

In order to illustrate the effect of varying the water content and grain size on the three-dimensional viscosity, four viscosity maps are included in figure 5.4 below. All relevant rheological flow law parameters can be found in table 2.1. Note that while the effective viscosity used in the FEM analysis is determined from the actual stress experienced at each individual element, a universal stress of 1 MPa is applied in the generation of the viscosity maps below. This allows for a comparison irrespective of applied ice loading history in simulation. It should however be noted that these maps do not fully represent the viscosity as used in the model, but rather illustrate the difference in magnitude of the overall viscosity per compositional setting.

As can be observed from figures 5.3 and 5.4, the temperature anomaly at the Baltic Shield translates to an area of relatively high viscosity in the effective viscosity distributions. It is also noted that while the 10 mm dry, 4 mm dry, and wet rheologies yield distinctively different effective viscosities, both wet rheologies result in a very similar overall weak viscosity distribution. Additionally it should be observed that compared to the viscosity captured by VM5a, both wet rheologies result in an overall effective viscosity that is two orders of magnitude lower. Also, such low viscosity borders on infeasibility.
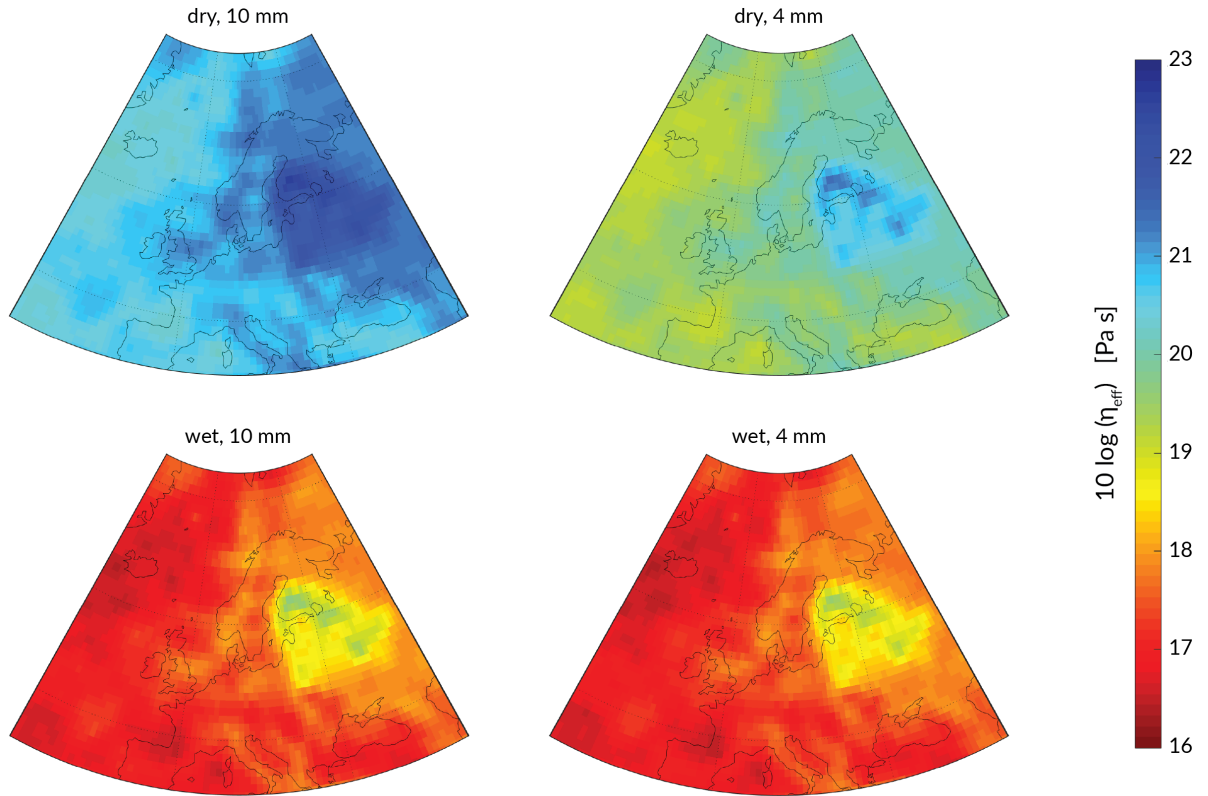
Figure 5.4: Effective viscosity at 275 km depth for four different composite rheologies using the WINTERC-3D thermal modal and a uniform stress of 1 MPa.

5.3. Topography

The topography used in this research has been defined by Whitehouse et al. (2012) (Blank, personal communication) and is available at a 0.25-by-0.25 degrees resolution. This topographic model consists of the ALBMAP (Le Brocq et al., 2010) for latitudes South of -55° latitude. The remainder of the topographic model consists of the ETOPO2v2 model (National Geophysical Data Center, NOAA, 2006).

5.4. Model settings

This section features a collection of additional model settings, such as the physical constants and number of iterations used in all simulations. These are described in sections 5.4.1 and 5.4.2 respectively. The overall resolution of the model is affected through both the meshing settings used in the Abaqus FEM model as discussed in section 5.4.3, and the settings used to solve the sea level equation as discussed in section 5.4.4.

5.4.1. Physical constants

An overview of all physical constants defined in the `model_data.py` file is included in table 5.2:

Table 5.2: Physical constants used in this research.

Constant	Symbol	Unit	Value
Gravitational constant	G	m^3 kg^{-1} s^{-2}	6.6732E-11
Density water	ρ_{water}	kg / m^3	1000.0
Density ice	ρ_{ice}	kg / m^3	931.0

5.4.2. Iteration

The number of model iterations performed, is defined by the user. The desired number of iterations is not determined through an automated process. Rather, a series of manual trial-and-error simulations has been executed by Blank (personal communication), who found that after 2 iterations an acceptable level of con-

vergence was achieved. While the level of convergence increases with the number of iterations performed, so does the computational cost.

5.4.3. Abaqus FEM resolution

5.4.3.1. Mesh size

Three specific variables constitute the size of all mesh elements, either within or outside of the high-resolution area. The mesh size outside of the high-resolution area is dictated by the `Seeds` variable. This seeding distance defines the maximum distance between nodes. Using this variable in a multi-layer and partitioned Abaqus model, the FEM software determines the actual final seeding distance. A similar approach applies to the high-resolution mesh area. The size of these specific elements in radial direction is set by `R_Target_seed`, and by `Plane_Target_seed` in planar direction.

As the total computation time increases with the amount of elements created, it is desirable to maximise their size. More importantly however, the accuracy of the model benefits from minimising the elements. It should be noted that in case the size of the mesh elements becomes too large, any three dimensional variation in the viscosity of the solid Earth is rendered insignificant. The same goes for the geographical features of Northwestern-Europe, being the location of shores and bodies of ice. Hence a balance should be found between a reasonable accuracy to capture the geophysical features of Northwestern-Europe, and a reasonable computational cost. Also it is desired to limit the difference in size between the high-resolution and low-resolution mesh elements in order to minimise the effects of the interaction between these elements at the boundary of the high-resolution area.

Figure 5.5a shows a capture of the Abaqus GUI depicting the elements within Northwestern Europe and the total load applied to these elements at 7 ka BP using the Bradley2018 model. The green elements are associated with dry land masses, the black elements are indicative of a large negative loading due to ice, and the grey elements correspond to large positive loading due to water. Note that the sign and magnitude of these loads represent a state relative to the onset of glaciation, as was detailed in section 4.2.3.1.

In figure 5.5a, `Plane_Target_seed` and `R_Target_seed` are both set to 80km, whereas `Seeds` is set to 350km. Similar values have previously led to an acceptable level of accuracy in the application of the original 3D GIA FEM model (Blank, personal communication). It can be seen here that with these seeding settings, the main geographical features of Northwestern Europe and its surroundings are visible. An example of such a feature is the Channel, which provides a clear separation between the Great-Britain and the European mainland.

5.4.3.2. Location and extent of high-resolution mesh

The definition of the high-resolution mesh area in the Abaqus FEM model has been detailed in section 4.2.2.1. The selection of the extent of this high-resolution mesh around a specific central location is substantiated here.

As this research focuses on the part of Europe in close vicinity of the North sea, and the two main former ice sheets over the British Isles and Fennoscandia, it is important that this region is well encapsulated in the high-resolution area. While the total high resolution area should be minimised to limit computational cost, the area should be large enough to provide a margin around its boundaries where smaller elements transition to larger elements as described in the previous section.

A process of trial and error has resulted in the selection of a high-resolution area of 18° angular radius centred around 11° latitude and 58° longitude. The extent and centre of this area are depicted in figure 5.5b.
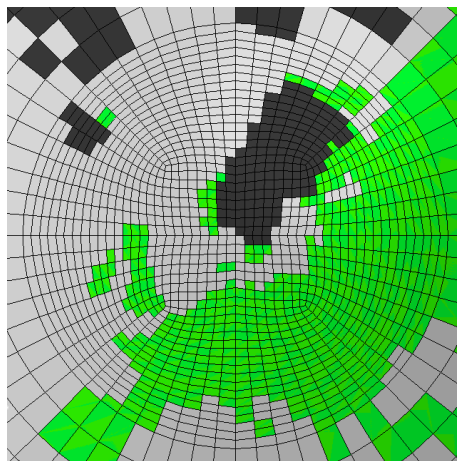
(a) High resolution mesh size in Abaqus FEM model. Gray, black, and green elements are associated with oceanic loading, glacial loading, and zero surface loading respectively.
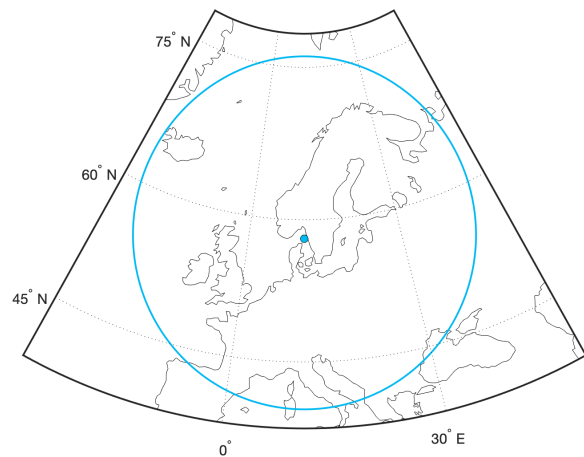
(b) Centre location and extent of high resolution partition.

Figure 5.5: Overview of selected mesh sizes for the high resolution Abaqus FEM model partition.

5.4.4. SLE module resolution

The maximum spherical harmonics degree and order that is used for global field decomposition in the SLE module, has been set to 256. The resolution of the ice and topography input files dictate the resolution at which the SLE is solved. The size of the regular global grid on which these inputs are available are the following:

ICE-6G_C	180 by 360
Bradley2018	512 by 1024
Topography	721 by 1441

As Northwestern Europe is characterised by deltas, islands, and irregular coastlines, it is beneficial to maximise the resolution at which the SLE is solved. This way, the shorelines are represented at the highest possible accuracy. Therefore, both ice models have been interpolated onto a target grid that matches the highest available resolution, i.e. the resolution of the topography. The 721 by 1441 grid implies a 0.25° resolution. Padding near the poles and the +180°/-180° meridian has been applied where necessary.

5.5. RSL databases

The selection of RSL databases is used in order to analyse the RSL curve results of the tests described in section 5.7. These databases have been used as they give a combined coverage throughout Northwestern Europe and were readily available through personal communication.

5.5.1. HOLSEA

The holocene sea-level database for the Rhine-Meuse Delta compiled by (Hijma and Cohen, 2019), contains 50 SLIP's and 56 upper limiting data points. Most data points in the so-called HOLSEA database are located in close proximity of one another. The resulting area-specific RSL curve in figure 5.6 shows a uniform far-field RSL behaviour for the Rotterdam-Scheldt region specifically.
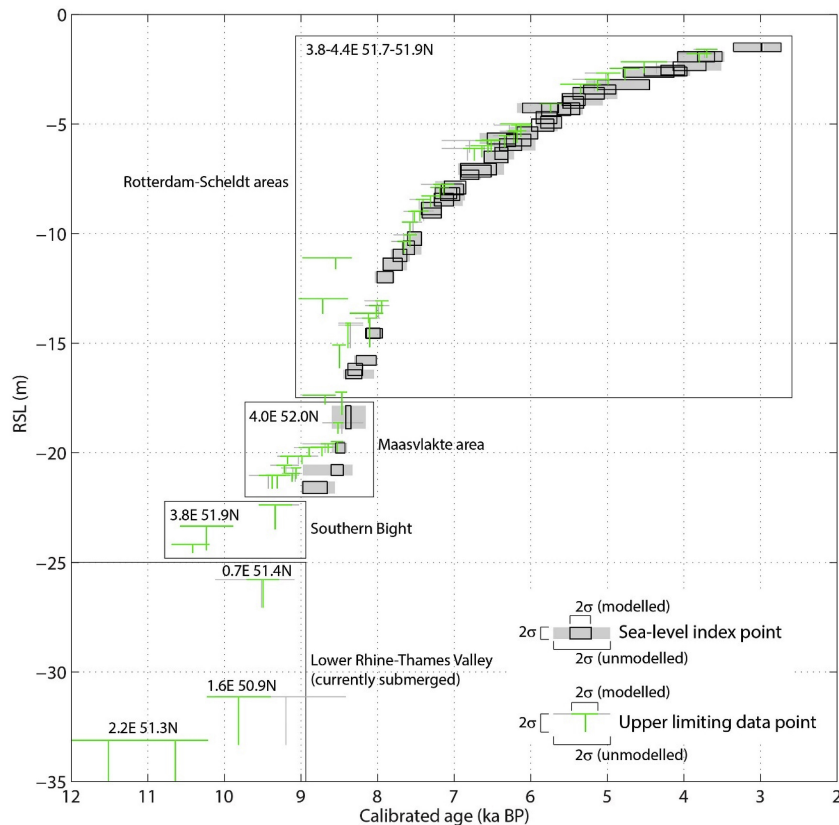
Figure 5.6: Plot of HOLSEA SLIPs and upper limits grouped per region, indicated by their respective latitude and longitude coordinates. From (Hijma and Cohen, 2019), figure 5.

5.5.2. Shennan and Bradley

The database complied by Shennan et al. (2018) henceforth referred to as SHEN-BR, contains more than 2100 RSL data points for Britain and Ireland. These data points include SLIPs, upper limits, and lower limits. The observational sites included in this database are depicted in figure 5.7. This figure also includes categorisation of these locations depending on their corresponding RSL curve behaviour, ranging from near-field (A), to far-field (E).

5.5.3. Tushingham and Peltier

The 1991 database compiled by Tushingham and Peltier, has been used in the construction of one of the predecessors of the ICE-6G_C (VM5a) model: the ICE-3G model (Tushingham and Peltier, 1992). It is not clear what the dependence is of the ICE-6G_C model on the RSL datapoints in this database, hence it is possible that a bias towards these RSL sites is present in the generated results using the ICE-6G model, especially when combined with the 1D viscosity profile. Note that the Tushingham and Peltier database is denoted TP92 in the remainder of this report. The TP92 database will mainly be used for RSL curve comparisons in Scandinavia. Three additional sites have been selected outside of Scandinavia, for the Dutch coasts and Scotland. The bulk of the TP92 RSL sites, located on the European mainland, are shown in Figure 5.8.
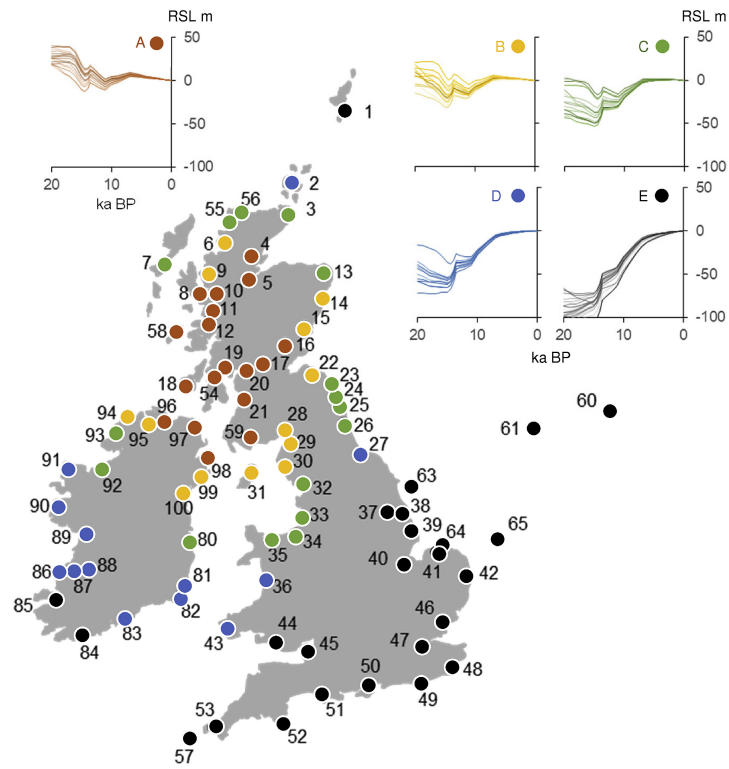
Figure 5.7: RSL sites in the SHEN-BR database, grouped in categories A to E on the basis of similarities in predicted RSL behaviour. From Shennan et al. (2018), figure 4.
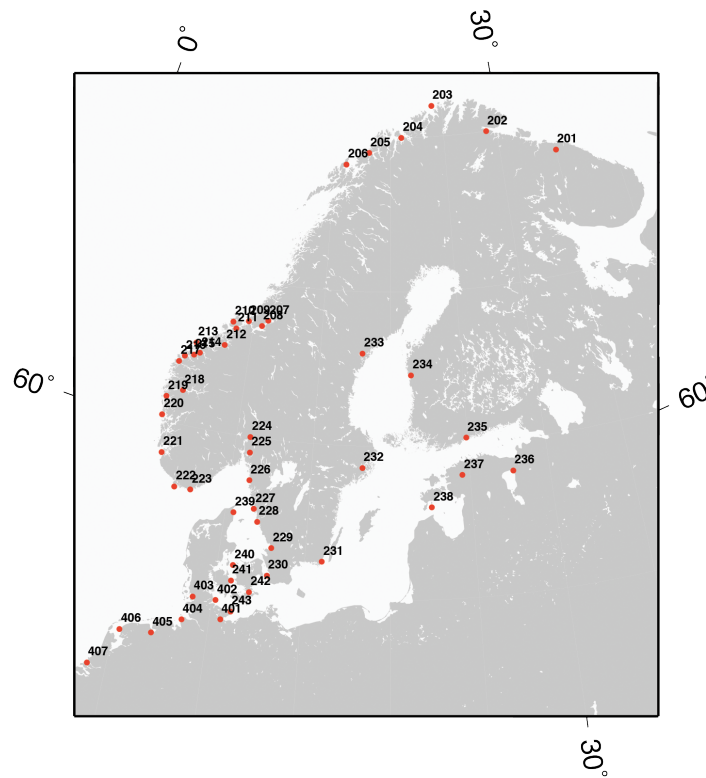
Figure 5.8: TP92 RSL observation sites (after van der Wal, 15/04/2019, personal communication).

5.5.4. Selected RSL sites

From the three RSL databases introduced previously, a number of observation sites has been selected for comparisons with simulated RSL output. The selected sites are included in figure 5.9 below. These sites have been selected such that they form a comprehensive set of sites in the near-field, mid-field, and far-field of both the British-Irish and Fennoscandian ice sheets. Sites that provide a large temporal spread of RSL observations are preferred.
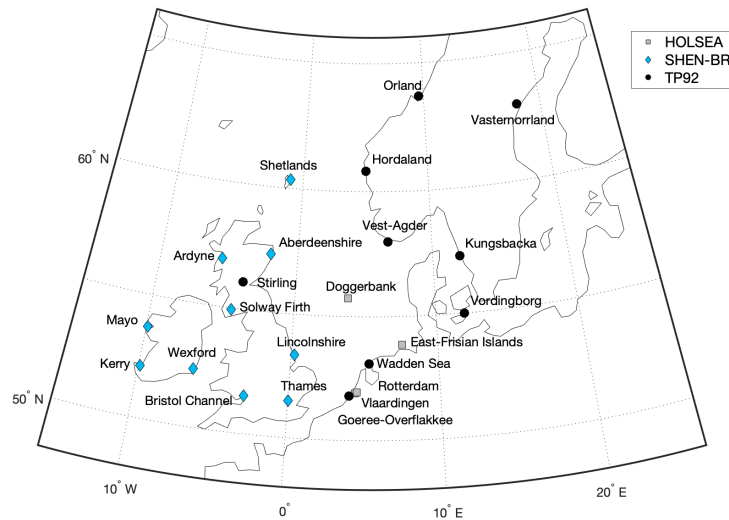
Figure 5.9: Selected RSL observation sites and corresponding site names.

5.6. GPS observations

The simulated uplift rates will be compared against two collections of radial velocities acquired at GPS stations throughout Europe. These two databases are discussed in sections 5.6.1 and 5.6.2 respectively. Having introduced the uplift rate data sets used, a brief discussion on their combined usage is provided in section 5.6.3.

5.6.1. BIFROST

Kierulf et al. (2014) have compiled one of the most recent GPS deformation rate data sets for Northwestern Europe. The GPS network used consists of all permanent Fennoscandian GPS stations for which more than three years of data is available. Additional sites located on the North European mainland yield a total number of 150 stations. The Kierulf2014 data set, is the most recent publication of station velocities within the BIFROST (Baseline Inferences for Fennoscandian Rebound Observations Sea Level and Tectonics) project, which was initiated in 1993 Lidberg et al. (2010). The extended BIFROST network is composed of a multitude of stations that are part of a multitude of regional GPS networks, being SWEPOS of Sweden, FinnRef of Finland, SATREF of Norway, and the EUREF Permanent Network (EPN) for sites in Northern Europe, including the UK Lidberg et al. (2010).

Note that a selection of older BIFROST GPS data as published by Lidberg et al. (2010) has been used to constrain the ICE-6G_C model (Peltier et al., 2015). This could introduce a bias towards the uplift rates at selected stations. Such a bias may be mitigated by using a reprocessed version of the BIFROST uplift rates as documented by Kierulf et al. (2014).

The Kierulf et al. (2014) solution is available with respect to both the ITRF2008 reference frame and a best fitting GIA reference frame. A further discussion on the importance of reference frame definition follows in section 5.6.3.

5.6.2. TIGA-WG

The second collection of uplift rates employed in this research are a product of the efforts of the Tide Gauge Benchmark Monitoring Working Group (TIGA-WG) (Hunegnaw et al., 2016), and have been provided by

Teferle (2018, personal communication). The TIGA-WG aims to provide vertical surface deformation rates for the correction of sea level measurements at tide gauges on a global scale. This is achieved through the combined solution using the analyses performed by the individual TIGA Analysis Centres (TAC) (Hunegnaw et al., 2017). The station velocities are computed with respect to the IGb08 reference frame (Hunegnaw et al., 2016), which in turn is aligned to the ITRF2008 (International GNSS Service, 2012).

5.6.3. Combined uplift rate observations

The GPS station locations and the locally observed uplift rates, are shown in the left frame of figure 5.10. Note that here both the BIFROST and TIGA-WG stations are depicted, and that some sites are included in both data sets. It is evident that the dense coverage in Fennoscandia is mostly provided by the BIFROST data sets. The TIGA-WG database provides additional uplift rates across the remainder of the European mainland and the British Isles. In this section some light will be shed on the impact of reference frame definitions on the observed and simulated uplift rates, and the differences between the two uplift rate databases introduced in the previous sections.

5.6.3.1. Reference frames

As was mentioned previously, the reference frames used in the BIFROST project and the TIGA-WG combined solution are ITRF2008 and IGb08 respectively. This gives rise to two complications which should be accounted for when comparing the simulated uplift rates with a combination of the observed uplift rates. First and foremost, it should be noted that the simulated uplift rates are obtained in a reference frame of which the origin coincides with the model's centre of mass. Wu et al. (2011) found that the ITRF2008 origin experiences a drift with respect to the true centre of mass at a level of 0.5 mm / year, primarily in the z direction. This leads to a bias between the simulated and observed uplift rates, which varies in latitudinal direction across Northwestern Europe. At 50 degrees latitude this bias equals circa 0.38 mm / year, and at 75 degrees latitude this bias equals circa 0.48 mm / year in upwards direction.

As demonstrated by Kierulf et al. (2014), the GPS uplift rates can also be realised in the reference frame as dictated by a GIA model and its centre of mass. This so called GIA frame approach allows for the minimisation of uncertainties and biases introduced by reference frame inconsistencies, plate tectonics, and other geophysical processes. As the resulting velocity fields using this approach are specific to the GIA model used, the solution computed with respect to the ITRF2008 reference frame is preferred for further usage in this research. Alternatively, one could compute both the observed and simulated uplift rates with respect to the rate at a single specific station (van der Wal et al., 2011). This approach too eliminates most differences introduced by a mismatch in reference frames, as well as the effect of rotational feedback which is captured in the observed uplift rates (van der Wal et al., 2015). Due to time constraints and the belief that the reference frame effects are sufficiently small to perform a visual comparison between model settings, neither approach has been implemented at this time.

5.6.3.2. Comparing observations between databases

Aside from the discrepancies that arise between simulated uplift rates and GPS observations as described previously, some caution should be exercised when combining two observation databases due to the differences between them. Both data sets are constructed with respect to two separate, albeit related, reference frames. Additionally, differences in the processing strategy of the GPS data may introduce discrepancies between the two data sets. By comparing the observed uplift rates and corresponding errors at stations that are included in both the BIFROST and TIGA-WG data set, the differences between the two can be investigated.

As can be seen from the left frame in figure 5.10, the TIGA-WG observations overall suffer from a larger error than the BIFROST observations. From the right frame it can be concluded that there is no recognisable pattern present, rather the magnitude of the differences between the two databases appears to be random. The lack of a spatially uniform difference or gradient thereof, implies that the difference in the reference frame used is negligible. Additionally, at the majority of the duplicate stations the error in the TIGA-WG observations exceeds the computed difference. It is undesirable to conduct a quantitative, statistical comparison between modelled uplift rates and observed uplift rates from these two different sources. Such analysis will not be conducted in this research. Rather, a visual comparison will be made on the magnitude and spatial pattern of simulated versus observed uplift rates. It is believed that by taking the aforementioned implications into account, it is acceptable to use the combined TIGA-WG and BIFROST observations in a comparison with the simulated uplift rates.
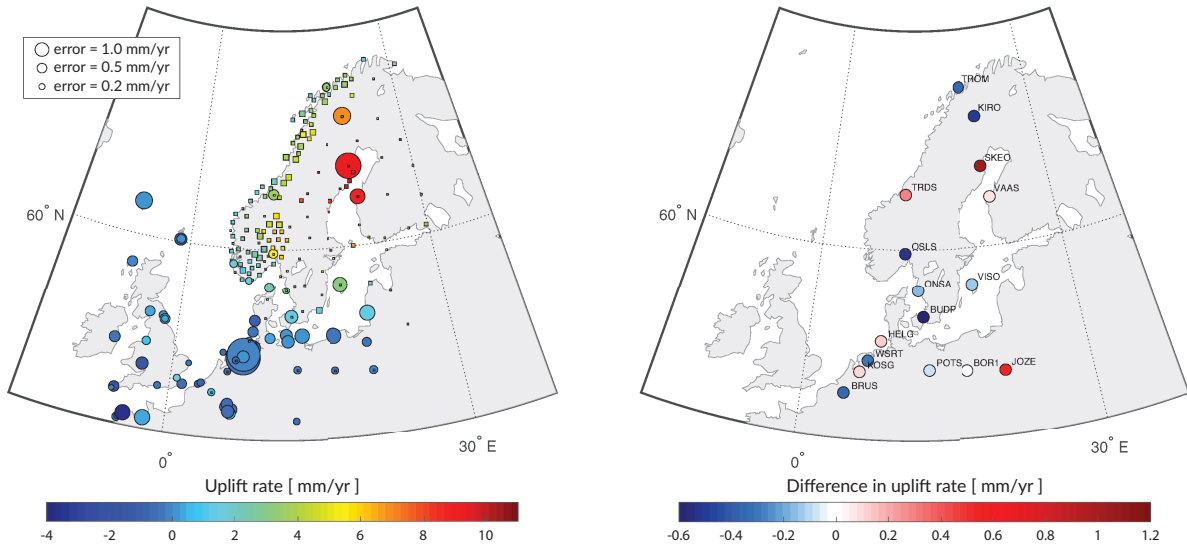
Figure 5.10: (left) Observed uplift rates and associated error from the TIGA-WG and BIFROST database indicated using circles and squares respectively. The icon size reflects the magnitude of the error. (right) Difference in uplift rate at stations included in both databases, computed by subtracting TIGA-WG observations from BIFROST observations.

5.7. Test overview

In this section, a brief overview is provided on the settings used in all executed simulations. Note that a more thorough explanation of these settings are included in the preceding sections. All simulations are assigned a unique test-ID, that will be used in the remainder of this report. The experiment design options are comprised of five rheological configurations, and two settings for the ice model input used. The motivation for the selection of these two ice models has been included in section 5.1.

The rheological configurations consist out of a single 1D configuration, and four 3D configurations. The latter configurations differ only in composition, which is determined by the grain size and the water content. Both variables are limited to two options each, being 4 mm and 10 mm for the grain size, and 0 and 1E3 molecules H per 1E6 molecules Si.

The grain sizes of 4 and 10 mm are deemed to be representative of the smaller and larger grain sizes encountered Scandinavia based on mantle xenolith observations Barnhoorn et al. (2011). The water content in a wet state corresponds to that of the oceanic asthenosphere (Hirth and Kohlstedt, 1996). These options for grain size and water content have been applied by both Barnhoorn et al. (2011) and van der Wal et al. (2013). By using identical rheological settings, a comparison can be made between the results of this study and those provided in literature. Note that the option of an even smaller grain size of 1 mm as employed by van der Wal et al. (2013) is excluded in this research. This is due to both time constraints, as well as the finding that settings using this 1 mm grain size are outperformed by rheological configurations using a larger grain size.

Separating all tests based on the ice model used, tables 5.3 and 5.4 describe the setup for all tests using the Bradley2018 and ICE-6G_C ice model respectively.

Table 5.3: Rheological configuration overview for Bradley2018 tests.

Test ID		1D BR	D10 BR	W10 BR	D04 BR	W04 BR
Ice model		Bradley2018	Bradley2018	Bradley2018	Bradley2018	Bradley2018
Viscosity profile		VM5a	3D	3D	3D	3D
Thermal model		N/A	WINTERC	WINTERC	WINTERC	WINTERC
Water content	H / 1E6 Si	N/A	0	1000	0	1000
Grain size	μm	N/A	10E3	10E3	4E3	4E3

Table 5.4: Rheological configuration overview for ICE-6G_C tests.

Test ID		1D 6G	D10 6G	W10 6G	D04 6G	W04 6G
Ice model		ICE-6G	ICE-6G	ICE-6G	ICE-6G	ICE-6G
Viscosity profile		VM5a	3D	3D	3D	3D
Thermal model		N/A	WINTERC	WINTERC	WINTERC	WINTERC
Water content	H / 1E6 Si	N/A	0	1000	0	1000
Grain size	μm	N/A	10E3	10E3	4E3	4E3

6

Results and discussion

In this chapter, the results of all 10 simulations described in section 5.7 are analysed. This analysis consists of a qualitative discussion of relative sea level curves and uplift rate maps as generated by using all 10 simulation settings discussed in the previous chapter. The methods through which these results are obtained are described in section 4.5. The results are compared against RSL and uplift rate observations as discussed in section 5.5 and 5.6 respectively.

As a first step in the analysis of the results, the performance of the two ice models considered is discussed in section 6.1. Here, only the 1D viscosity profile is included. The results obtained from GIA simulations using the Bradley2018 ice model in combination with a range of 3D composite rheology configurations, are discussed in section 6.2. In section 6.3, a similar approach is applied to the analysis of the results obtained using the ICE-6G_C ice model.

Note that often times throughout this chapter, a selection of the results is presented rather than the full set of available results. All generated results have however been included in this report, and can be found in Appendix B.

6.1. Ice model performance
In order to assess the ice model performance, a comparison is made between the RSL and uplift performance of the ICE-6G_C and Bradley2018 model in combination with the 1D VM5a viscosity model. Referring back to the test overview in section 5.7, these simulations are denoted 1D 6G and 1D BR respectively.

6.1.1. RSL curves
Out of the 23 RSL observation sites available, a selection of 6 locations is included in figure 6.1. The measurement sites included here, were found to provide a good representation of the model performances in the far-field, mid-field and near-field RSL behaviour at all sites for both ice models. The conceptual differences between these three types of behaviour have been discussed in section 3.2.2.

6.1.1.1. Far-field behaviour
The far-field behaviour can best be identified at two measurement sites in the Netherlands, being Goeree-Overflakkee and Rotterdam. The RSL measurements available at these sites originate from two separate RSL databases, TP92 and SHEN-BR respectively. It can be seen that irrespective of the source of the observations, the ICE-6G_C model slightly outperforms the Bradley2018 ice model in the far field. Using an identical 1D rheology, the far field behaviour in both simulations is mainly characterised by the total global ice melt. As was discussed in section 5.1, the ICE-6G_C model consists of a collection of regionally and globally tuned ice sheets in Europe, North-America, and Antarctica. The Bradley2018 model on the contrary, exists of ICE-3G, which in itself is a legacy version of the ICE-6G_C model. Hence, it is reasoned that the differences between the two ice models outside of Northwestern Europe gives rise to the superior performance of the ICE-6G_C model in the European far-field.
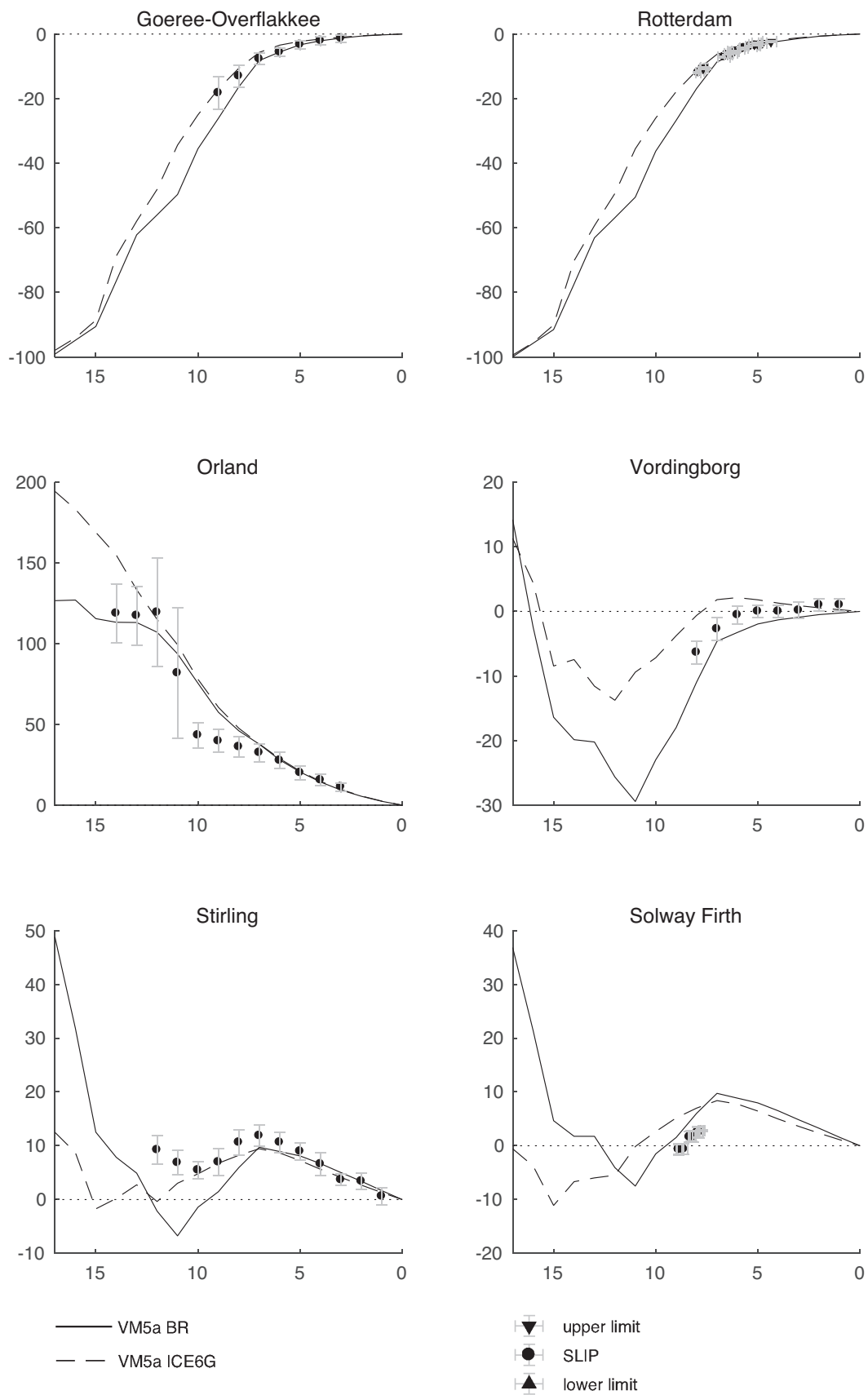
Figure 6.1: RSL curves and observations for a selection of sites, using the VM5a 1D viscosity model in combination with the ICE-6G_C and Bradley2018 ice models. Time in ka BP on the x-axis and RSL in meters on the y-axis.

6.1.1.2. Near-field behaviour
When investigating the near-field RSL curve for Orland, it can be seen that the RSL observations indicate a rapid step-like decrease in RSL between 12 and 10 ka BP. This behaviour is not displayed by the ICE-6G_C model. The more steep and fitting decline in RSL as captured by the Bradley2018 model, is attributed to the rapid decrease in ice height recorded in this model between 11 and 10 ka BP. It is of interest to investigate whether the fit of a model using the Bradley2018 ice history can be improved by including a 3D rheological configuration, rather than the 1D VM5a viscosity profile used here. This will be discussed in section 6.2.

6.1.1.3. Mid-field behaviour
Discussed last, is the RSL performance of the Bradley2018 and ICE-6G_C model at mid-field sites in both Scotland (Stirling, Solway Firth) and Denmark (Vordingborg). It can be seen that at all sites, both models show an initial decrease in RSL, followed by an increase in RSL, and another period of decreasing relative sea level until present time. As was discussed in section 3.2.2, the sudden increase in RSL is caused by the sea level rise after the mid-field has become ice free. The concluding RSL decrease can be attributed to forebulge migration. The timing of the transitions between RSL decline, increase, and decline, as observed from the SLIPs, are best reproduced by the Bradley2018 model. This applies to all three sites considered here.

When taking a closer look at the respective performance of the two ice models at Stirling, it can be seen that the ICE-6G_C model does appear to provide a good fit to the observed RSL, most notably from 10 ka BP onwards. It is however also evident that timing-wise, the consecutive decline, increase, and decline of the RSL observations is better represented by the Bradley2018 model. It is believed that this example in particular justifies the application of a qualitative RSL curve analysis over a quantitative analysis. A quantitative analysis, using for example the commonly applied chi-squared misfit (Wu, 1999), may express a smaller misfit for the ICE-6G_C model while a larger misfit is computed for the Bradley2018 model which better captures the RSL fall-rise-fall behaviour at this location.

Using the aforementioned analysis, it is concluded that between the ICE-6G_C and Bradley2018 model, the latter should be considered the preferred glacial model for Northwestern Europe. It should however be noted that the ICE-6G_C model slightly outperforms the Bradley2018 model in terms of global ice melt volume, which is follows from RSL observations in the far-field.

6.1.2. Uplift rates
The simulated uplift rates in figure 6.2 show that both simulations 1D BR and 1D 6G predict that uplift occurs near the centre of the former Fennoscandian and British-Irish ice sheets. Note that both simulated uplift rates are underestimations of the observed uplift rates around the Gulf of Bothnia. The Bradley2018 model yields higher uplift rates than the iCE-6G_C in this area, providing a better approximation of the observations. The model performance along the Scandinavian shores is good for both models. It is however noted that the ICE-6G_C model results in positive uplift rates that stretch too far into the Norwegian Sea, whereas the Bradley2018 model results in positive uplift rates that do not stretch into the Norwegian Sea far enough. The quality of the fit deteriorates outside of Scandinavia. Observations in Wales and Northern Scotland suggest that the uplift signature of the ICE-6G_C model in particular stretches too far towards both the north and south. While the Bradley2018 model does provide a better representation in this direction, this observation is substantiated by data from just two GPS stations. Neither model configuration is able to match the observed uplift rate Ireland, England or in the remainder of the European mainland.

From the simulated uplift rates, it can be observed that neither ice model using the radially symmetric viscosity profile is able to accurately predict uplift rate outside of the formerly glaciated areas. However, the vertical surface deformation modelled in this research, includes GIA induced surface deformation only. While GIA is believed to be the dominant factor in vertical surface deformation near the centre of former ice sheets, other processes may dictate such deformation outside of these regions.

A main difference that can be observed by comparing the uplift rates for both ice models, is the extent of the regions centred at the former ice sheets that show a positive vertical surface deformation rate. It is evident that using the ICE-6G_C model, a larger area experiences a positive uplift rate at present time. For the Bradley2018 model these areas are limited to the north west of the British Isles and the entirety of Scandinavia bounded by the shores of the European mainland, the ICE-6G_C model results in a positive uplift rate for the entire United Kingdom and Scandinavia, as well as the northernmost portion of East-Europe. This is attributed to the difference in height and extent of the Fennoscandian and British-Irish ice sheets between both ice models as discussed in section 5.1.

The increased uplift rate to the south of Scandinavia as simulated using the ICE-6G_C model, is found

to be too large and not in agreement with the GPS derived uplift rate in this area. It is reasoned that based on these observations, the Bradley2018 model is preferred for simulation of the GIA induced uplift rate in Northwestern Europe. This is in agreement with the findings based on the RSL curves in the previous section.
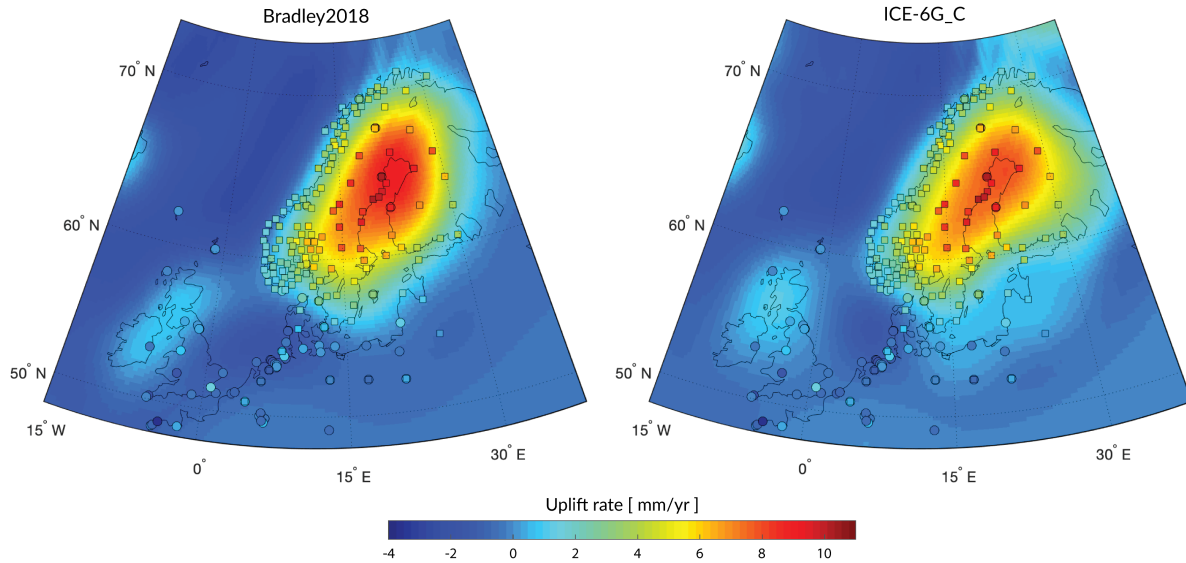
Figure 6.2: GPS derived vertical surface deformation and simulated uplift rate in Northwestern Europe, using the VM5a 1D viscosity model in combination with the ICE-6G_C and Bradley2018 ice models.

6.2. Bradley2018 3D rheologies

6.2.1. RSL curves

In this section, the RSL curves obtained from all model configurations using the Bradley2018 model are discussed. In total, a selection of 12 sites is included in this section. These sites provide a good spatial coverage within Northwestern Europe. Additionally, these sites were found to best represent the agreements and differences between the performances of the 3D rheologies for all sites.

Figure 6.3 includes a selection of sites mainly located in Scandinavia, whereas 6.4 contains the remaining RSL focusing on the British Isles.

6.2.1.1. Weak and strong rheologies

An observation that can be made from both figures 6.3 and 6.4, is that the 3D rheological configurations can yield RSL curves that differ significantly from the 1D rheological configuration. A single exception to this observation however arises at the Rotterdam RSL site in figure 6.4. As was mentioned in the previous section however, this is attributed to the relatively minor contribution of the local rheology to RSL curves in the far-field when compared to the eustatic sea level rise.

At all remaining sites, it can be seen that, in addition to the differences between the 3D and 1D configurations, very distinct variations exist between the four 3D composite rheology configurations themselves. As was discussed in section 5.2, the wet rheological configurations yield relatively low effective viscosities that are significantly lower than the VM5a model. Also, in contrast to the two dry rheological models, the effective viscosity for both wet rheological configurations were found to be relatively similar to one another irrespective of grain size. This similarity can also be observed from the RSL response in the mid-field and near-field. It can be seen that at all sites included in figures 6.3 and 6.4, the relative sea level curves for both wet rheological configurations are located very close to one another.

It can however also be seen that at some locations, the weaker dry rheology using 4 mm grains, results in RSL curves that are nearly identical to the wet rheological configurations. This is the case for all depicted Scottish and Irish sites, as well as the Doggerbank site. Note that this also applies to the Irish sites of Kerry and Mayo, included in appendix B. At the Scandinavian RSL sites however, the RSL behaviour of the 4 mm

dry configuration can be differentiated from the wet configurations more easily. Here the 4 mm dry rheology appears to resemble the strongest 10 mm dry rheology more closely.

It is believed that the resemblance of the 4 mm dry rheology to the wet rheologies throughout Britain, and the lack thereof in Scandinavia cannot be explained in terms of geology. There is no common denominator between the Scottish, Irish, and Doggerbank sites in terms of temperature distribution or tectonic origin.

It could however be possible that the difference in behaviour between the 4 mm dry rheology and the two wet rheologies is caused by a difference in stress in the interior of the Earth. The BIIS is covers a significantly smaller area and is of less height compared to the FIS. This implies that the stress beneath Scandinavia is higher than the stress beneath the British Isles.

It is hypothesised that for higher stresses, the resemblance between the viscosity of the 4 mm dry and wet rheologies is less than for lower stresses. As was discussed in section 2.2.3, dislocation creep is the dominant creep mechanism in areas of high stress. This type of creep is independent of grain size. In order to test the hypothesis, the universal stress of 1E6 MPa used to create the viscosity maps in section 5.2.3 has been replaced by a universal stress of 1E5 MPa and 1E7 MPa. With the lowest universal stress, the 10 mm wet and the 4 mm dry rheology yield a very similar viscosity distribution, and the 4 mm wet rheology results in an overall weaker viscosity that differs by circa 1 order of magnitude from the other two rheologies. Conversely, with the highest universal stress, the two wet rheologies yield a near-identical viscosity distribution that overall is more than 3 orders of magnitude lower compared to the 4 mm dry rheology. This confirms the previously stated hypothesis, and thereby the relevance and importance of the inclusion of a composite rheology over a solely linear or non-linear rheology as discussed by Forno et al. (2005); Gasperini et al. (2004); van der Wal et al. (2010).

6.2.1.2. Site-specific preferred rheologies
In this section, the preferred rheologies for the sites in figures 6.3 and 6.4 are discussed.

Firstly, for a few sites the inclusion of 3D composite rheologies has not resulted in a better fit to the observed RSL data when compared to the 1D viscosity distribution. This is the case for Vasternorrland, Aberdeenshire, and Solway Firth. At the two Scottish sites, the overall RSL trend derived for the 1D rheological configuration shows the highest resemblance to the strongest rheology, using 10 mm dry grains. It should however be noted that at Aberdeenshire, this rheological setting conflicts with an upper limit present at 12 ka BP.

The 10 mm dry rheology is the preferred configuration at two other sites in Scotland, being Stirling and Ardyne. Whereas this rheology is ruled out at Aberdeenshire due to an upper limit, the 10 mm dry rheology is the only configuration deemed feasible at Ardyne due to a range of lower limits. The Stirling curve shows that the inclusion of a 3D composite rheologies can yield a significant improvement of the fit of the simulated sea level to the observed SLIPs.

When assessing the overall performance of the dry, 4mm grain size rheology, it can be observed that this rheological configuration is among the preferred configurations for the majority of the sites depicted. At the Doggerbank, Vasternorrland, Hordaland, Kungsbacka, Vordingborg, Wexford, and Rotterdam, this slightly weaker yet dry rheology, provides a relatively good fit to the observed RSL. This contrasts (van der Wal et al., 2013), who found that regardless of the thermal model used, the best fit to RSL observations in Fennoscandia required a 10 mm wet rheology.

While the two wet rheologies do provide an improved or equally good fit to the RSL observations compared to all other rheologies at Vordingborg and Wexford, the overall RSL trend at these sites can also be attained by the dry 4 mm grain size rheology. At the Vest-Agder site exclusively, a wet rheology yields an RSL trend that cannot be represented by any other rheological configuration. The increase in RSL and the change in sign between 10 and 5 ka BP which is visible in the SLIPs, could only be simulated by the weakest rheology considered, being the 4 mm wet configuration.

Figure 6.3: RSL curves and observations for a selection of sites, using the Bradley2018 ice model in combination with various rheological configurations. Time in ka BP on the x-axis and RSL in meters on the y-axis.
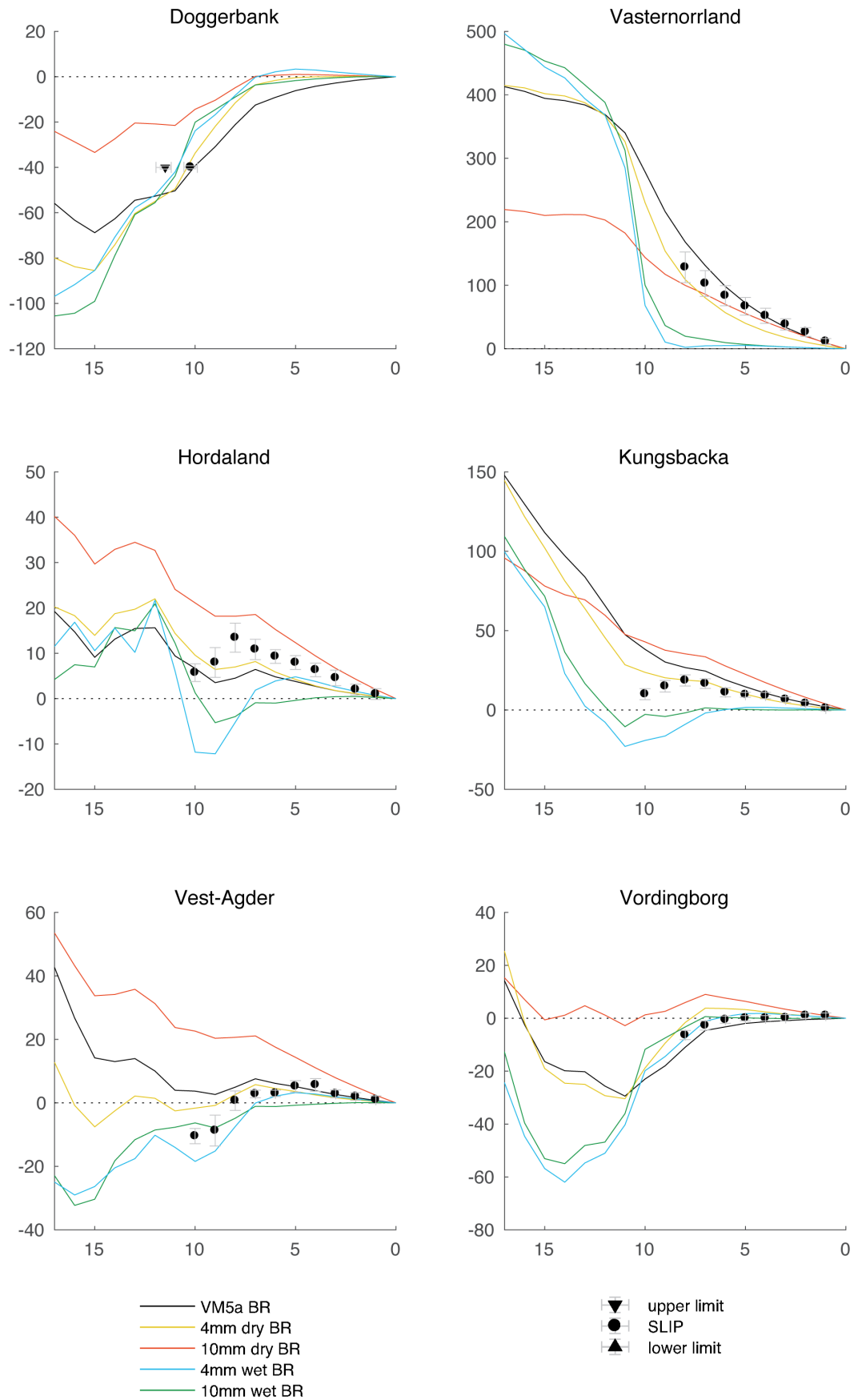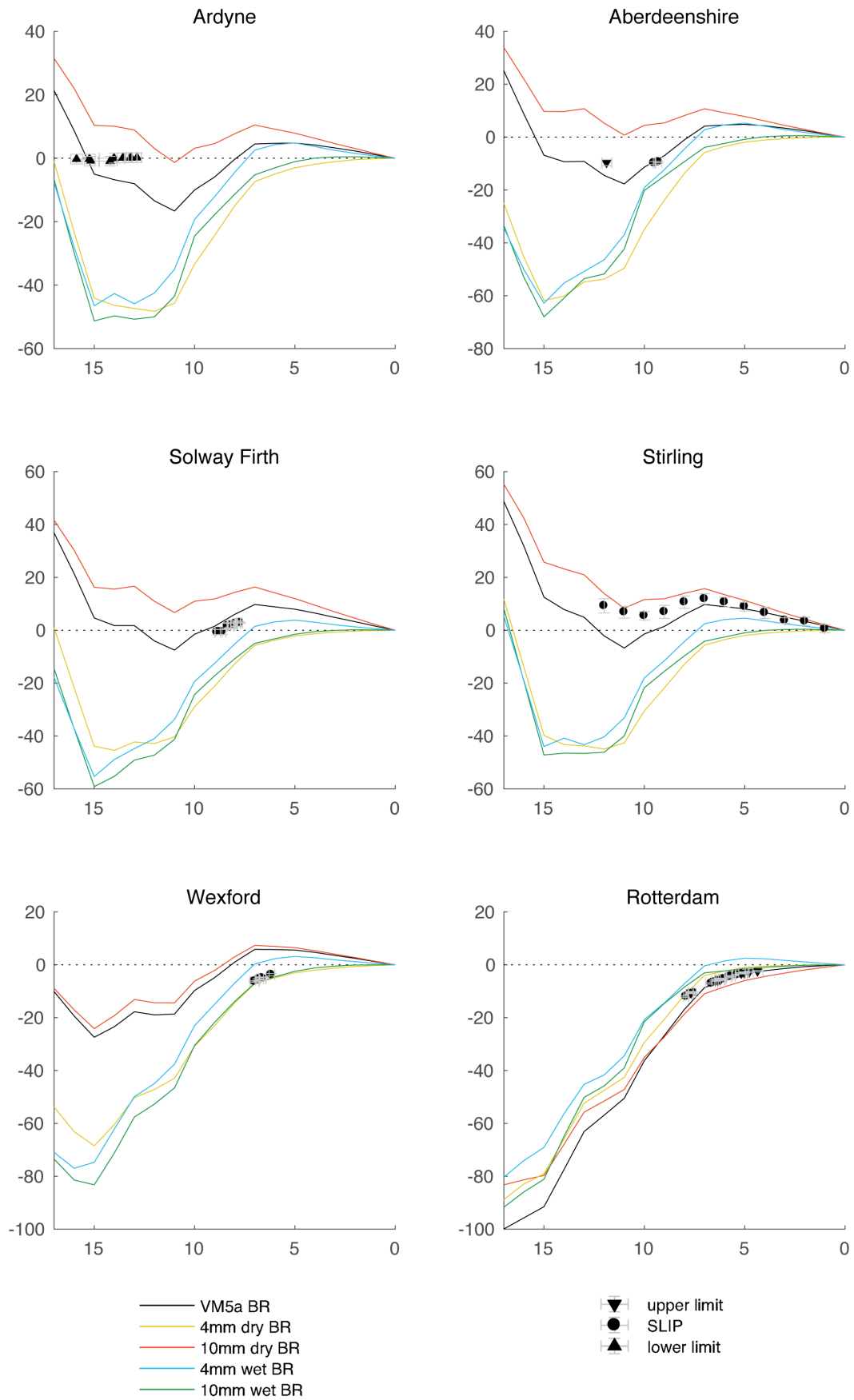
Figure 6.4: RSL curves and observations for a selection of sites, using the Bradley2018 ice model in combination with various rheological configurations. Time in ka BP on the x-axis and RSL in meters on the y-axis.

6.2.1.3. Regional synthesis of preferred rheologies

From the preceding site-specific analysis on model performance per rheological configuration in terms of RSL, it is attempted to synthesise these findings such that the rheologies preferred on a regional scale within Northwestern Europe can be identified. The following discussion employs both the results depicted in this section, as well as the additional results included in appendix B. It is attempted to link the preferred rheologies to the tectonic origin of various regions within the area of focus. This may aid in inferring a relation between the composition and tectonic properties of the Earth's interior in Northwestern Europe, and in answering the third research question posed in this study.

Note that differences that arise from the tectonic origin of all regions within Northwestern Europe are partially accounted for in the 3D rheological configurations through the thermochemical model used. The most evident example of this fact is the large transition from a low temperature and consequently high viscosity of the Baltic Shield to a high temperature and low viscosity in the remainder of Scandinavia. It is however possible that not only the temperature, but also the composition of the mantle material differs with its tectonic age, as discussed in section 2.2.3. Additionally, it is uncertain to what extent the composition affects the WINTERC-3D model.

Firstly, it is observed that at all Irish RSL sites, the relatively weak rheologies using either a smaller grain size or a higher water content are preferred. When assessing the RSL curves at the Scottish sites, a less uniform observation is made. As was mentioned previously, a stronger rheology appears to be preferred at Solway Firth, Stirling, and Ardyne. It is evident that at the latter, the weaker rheologies are deemed not feasible. In the east of Scotland however, the opposite is true. At Aberdeenshire, the strongest rheology using dry 10 mm grains is excluded as a feasible configuration. At the Lincolnshire, Bristol Channel and Thames sites, the preferred rheology is deemed ambiguous. This is attributed to the low dependence of far-field RSL behaviour on local rheology. As such, no definitive verdict can be obtained for these English and Welsh sites. Summarising, it appears that a weak rheology is preferred for the entirety of Britain and Ireland, with the exception of the mid-west of Scotland. Comparing these findings with the tectonic properties of Northwestern Europe as discussed in section 2.1.2, it is concluded that no clear correlation between the variation in tectonic age of the British Isles and the preferred rheologies found here.

At the Dutch and German far-field sites, the curves per rheological configuration are slightly more diverse than those for the south of Britain. At Vlaardingen, Goeree-Overflakkee, and the Wadden Sea, a preference for the two dry rheologies and the 1D viscosity profile can be observed. At Rotterdam, all but the dry 10 mm and 1D rheologies are excluded. Similarly, the two wet rheologies are excluded at the East-Frisian Islands. Hence, all RSL sites that lie within the German-Polish Caledonides that are investigated here can be modelled to an acceptable degree using either the 4mm or 10 mm dry rheology.

At the Shetlands, none of the 3D composite rheology configurations is deemed feasible. At the Doggerbank however a clear preference for the weaker rheologies exists. Due to the limited availability of RSL measurements in the marine margin between the British Isles and Scandinavia, no evident relation between the tectonic age and preferred rheology can be found.

In the Northern part of Scandinavia, at Vasternorrland and Orland, a clear preference exists towards the stronger, dry rheologies. This contradicts the conclusion drawn by Barnhoorn et al. (2011), stating that a wet upper mantle is most likely present in Scandinavia. Such wet rheology is however preferred at the Vordingborg and Vest-Agder sites. Some specific interest goes out to the RSL behaviour at the Hordaland and Kungsbacka sites. Here the trend of RSL rise between 10 and 8 ka BP can only be captured by the weaker rheologies. The overall fit to the observed RSL at these sites however is best for the weaker, yet dry, 4 mm grain size rheology.

Based on the preference for wet rheologies at Vest-Agder and Vordingborg, it is reasoned this may imply that material dated to the Sveco-Norwegian orogen has a higher water content than the mantle material in its surroundings. This implication is however not unambiguous and could be confirmed nor denied in this research. It is not known exactly whether material dated to this time period is expected to have a higher water content than older or younger material. Both paleozoic (ca. 550 - 250 ka BP) and proterozoic (2500 - 550 ka BP) subduction zones may exist beneath the Sveco-Norwegian region (Artemieva et al., 2006), which is also intersected by the northern end of the Trans-European Suture Zone. While such subduction zones are however not limited to the interior beneath the Sveco-Norwegian region, this could explain the local preference towards a wet rheology.

6.2.2. Uplift rates

In this section, the simulated uplift rates for all 3D rheological configurations are presented and discussed. From figure 6.5 it is evident that the weaker rheologies, i.e. the rheologies that are either wet and/or are of smaller grain size, all perform poorly near the two expected centres of uplift. The dry 10 mm grain size rheology however yields a good fit to the uplift rates expected at the formerly glaciated areas.

When comparing the uplift rate fit of the Bradley2018 ice model using this strong, 3D rheology, to the 1D rheological configuration in figure 6.2, it can be seen that both yield very similar results. This corresponds to the findings of van der Wal et al. (2013). Two key differences however arise between the 10 mm dry rheology and the 1D viscosity distribution. Firstly, it can be seen that the magnitude of both the positive vertical deformation rate centred at Scandinavia and the negative vertical deformation rate in the Norwegian Sea, is slightly larger for the dry 10 mm rheology than for the 1D viscosity profile. It can also be observed that the positive uplift rates for the 10 mm dry rheology extend further outwards when compared to the 1D configuration, most notably along the Norwegian coasts and into the eastern European mainland. Secondly, it can be observed that the centre of uplift appears to have shifted: while for the 10 mm dry rheology the centre of uplift is located in Sweden, for the 1D configuration the centre of uplift lies directly above the Gulf of Bothnia. This is the body of water between Sweden and Finland.
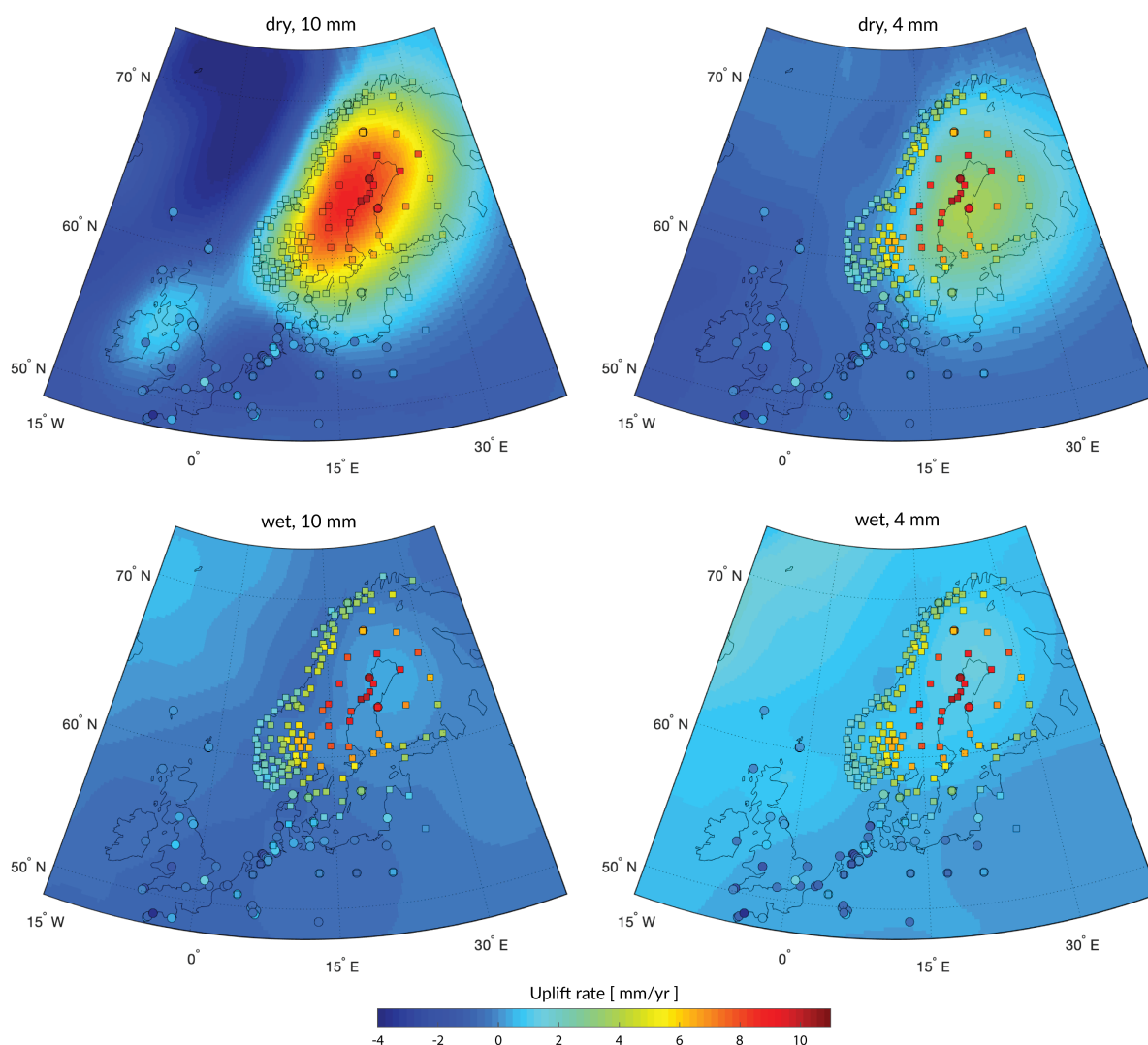

Figure 6.5: GPS derived vertical surface deformation and simulated uplift rate in Northwestern Europe, using the Bradley2018 ice model in combination with various rheological configurations.

Lastly, it is of interest to note that using the 1D viscosity distribution, the centre of subsidence between the British Isles and Scandinavia is located to the north of the Wadden Sea. For the 10 mm dry rheological configuration, this feature is however located more to the south, centred within the Netherlands. The overall vertical surface motion of the Netherlands is described as tilting along a north-west to south-east axis (Fokker et al., 2018). Due to the shift of the centre of subsidence mentioned previously, such a tilt cannot be observed from the GIA induced uplift rates that result from the 10 mm dry rheological configuration. It is implied that the GIA induced tilt of such coastal areas is sensitive to the inclusion of a 3D composite rheology, and should be accounted for in the future. Note that a zoomed-in uplift rate map using a different projection and colour scale is included in the section hereafter.

It is believed that the aforementioned differences can be attributed to both the difference in viscosity between the 1D and 10 mm dry rheological configuration in terms of stress-dependent magnitude, and lateral variation. The overall magnitude of the effective viscosity of the 10 mm dry composite rheological configuration is high when compared to the VM5a model for a universal stress of 1 MPa as described in section 5.2. Higher stresses are however expected to be encountered locally, e.g. beneath the Fennoscandian ice sheet. Such higher stresses can diminish the contribution of dislocation creep to the overall strain and strain rate as discussed in section 2.2.3. Taking into account the applicability of high stress and the variation in temperature between the Baltic shield and its surroundings, it is believed that the 10 mm dry rheology yields a higher effective viscosity at the Baltic shield, and a lower effective viscosity to the west of the Baltic shield. This could explain the difference in magnitude of the present time uplift rate in Sweden and along the Norwegian coast.

Additionally, due to this large temperature variation due to the Baltic shield, a transition between a high viscosity and low viscosity zone exists directly beneath the former Fennoscandian ice sheet when using the 10 mm dry rheology. As the eastern part of Scandinavia is characterised by a higher viscosity than the west, this region provides a higher resistance against surface deformation. As such, the uplift rate in eastern Scandinavia is lower than in the west, yielding a displacement of the centre of uplift with respect to the 1D viscosity configuration.

As was mentioned previously, out of all 3D rheological configurations considered in this section, only the 10 mm dry rheology yields a good fit to vertical surface deformation in GIA dominated regions. Similar to van der Wal et al. (2013), the weaker rheologies yield an inferior performance in terms of uplift rate. While the 4mm dry rheology does show uplift near the former Fennoscandian ice sheet, this is not the case for the former British-Irish ice sheet. Moreover, the magnitude of the uplift in Scandinavia is too low when compared to the GPS derived uplift rates.

Analysing the fit of the two wet rheologies to the observed vertical surface deformation rates, it can be concluded that both configurations yield a poor fit and fail to reproduce the expected uplift in previously glaciated areas. Very minimal uplift signatures are present in Scandinavia. While these wet rheologies do not agree with the observed uplift rates in Northwestern Europe, it was found that a more recognisable signature of positive vertical surface deformation is present in North-America. Included in figure 6.6, are uplift rate maps for both wet rheologies that include both North-America as well as Northwestern Europe.

From figure 6.6, it can be concluded that ongoing uplift is simulated near the former Laurentide ice sheet in North-America when considering the 10 mm wet rheology. As this ice sheet is deemed larger and higher, i.e. more massive than the European ice sheets, it is reasoned that this positive uplift rate can be partially attributed to the long wavelength GIA induced response of the lower mantle. Beneath 420 km depth, the 3D GIA FEM model again follows the VM5a viscosity distribution irrespective of the rheological configuration. Above this depth the 4 mm wet rheology is however deemed weaker than the 10 mm wet rheology. Therefore it is expected that the more shallow and local GIA response to the Laurentide ice sheet glaciation and deglaciation has already been dissipated using the wet, 4mm grain size rheology, leaving only a marginal yet long wavelength uplift rate signature in the Northern hemisphere.
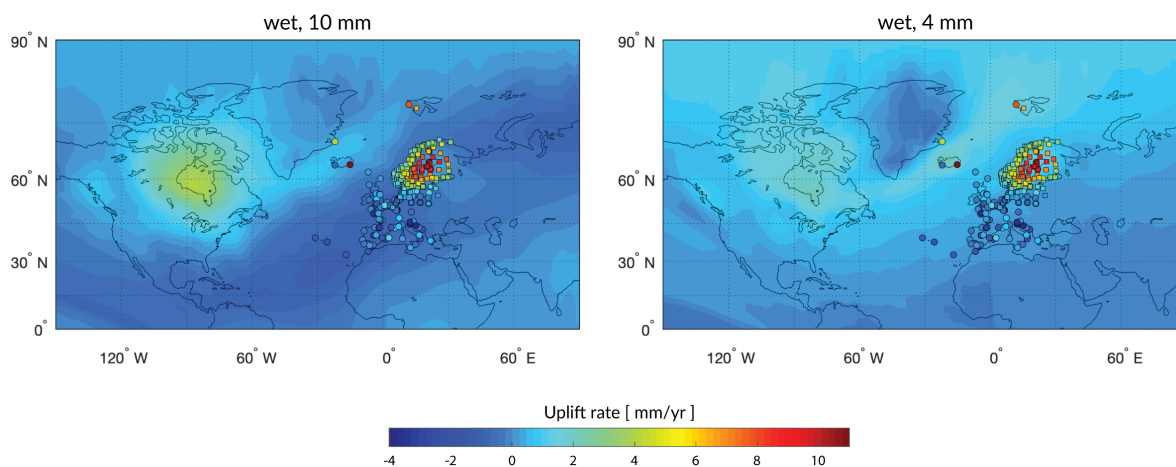
Figure 6.6: GPS derived vertical surface deformation and simulated uplift rate in Northwestern Europe, using the ICE-6G_C ice model in combination with various rheological configurations.

6.2.3. RSL change rates

In this section a brief comparison is made between the RSL change rates presented in section 3.2.2 and the RSL change rates that are modelled using the two best performing models in terms of uplift rate. These are the 1D and 10 mm dry configuration. Note that no RSL change rate observations are used in this comparison, rather this section provides additional insight into the effects of the inclusion of 3D rheological models on the spatial distribution of present day relative sea level change.

It can be seen from figure 6.7 that the left frame does not fully agree with its counterpart in figure 3.5 in terms of magnitude and sign. This is best visible between Scotland and Norway, as well as around Ireland. Here the Bradley2018 VM5a configuration yields a negative RSL change rate, more so than the Bradley2011 configuration in figure 3.5. It should however be noted that both the ice model as well as the Earth model used differ between the two: figure 3.5 is compiled using the Bradley2011 model in combination with its own preferred 1D Earth model, whereas the left frame in figure 6.7 is constructed using the newer Bradley2018 model in combination with the VM5a Earth model.
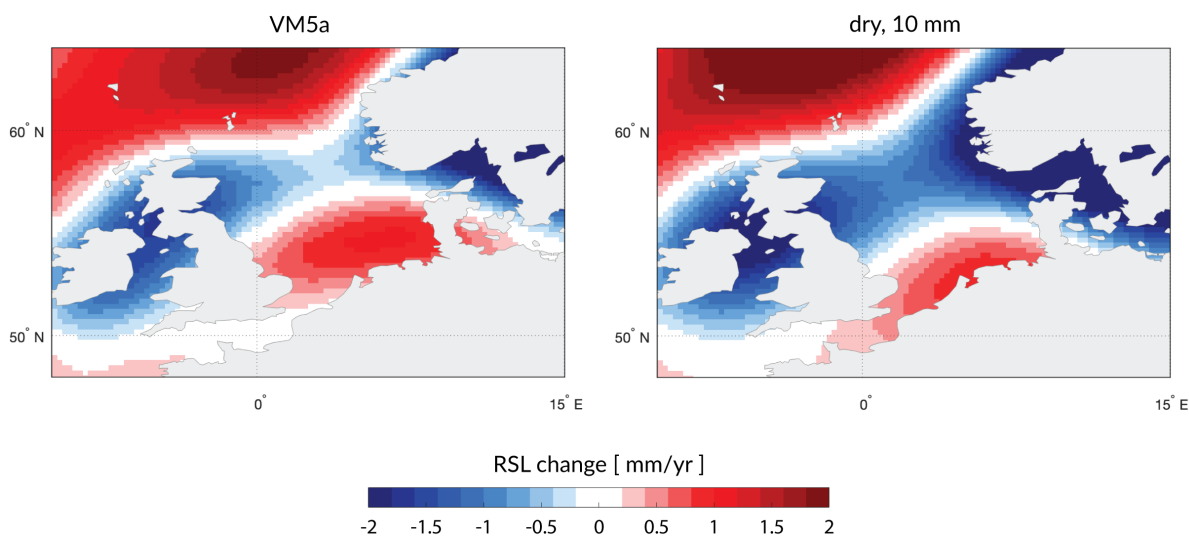
Figure 6.7: Relative sea level change rates, using the Bradley2018 ice model in combination with various rheological configurations.

Most notable however is the similarity in behaviour with respect to the uplift rates as described in the previous section. The magnitude and extent of the region with a sub zero RSL change rate increases between the 1D and 10 mm dry configuration. As a consequence, the negative RSL change rate modelled in Scandinavia extends further beyond the Norwegian and Swedish shores. Additionally, the centre of positive RSL change rate in the North Sea is shifted from the marine environment at circa 55 degrees latitude, to a location at circa

52 degrees latitude centred in the Netherlands. Such a shift may lead to an RSL change rate increase of circa 0.2 mm per year. This observation is of interest for future analysis of sea level change and surface deformation along the Dutch coasts. More on such sea level change projections is discussed in section 6.3.2.

For future reference and comparison purposes, two new plots of the uplift rates in proximity of the North Sea are included in figure 6.8. This figure adheres to the same projection and scale as the RSL change rate plots in figures 6.7 and 3.5. It is evident that while the direction of the two rates are inverted, the spatial distribution of the rate minima and maxima are nearly identical. The sum of the RSL change rates and the uplift rates in this section is equal to the geoid rate, as dictated by the definition of the sea level described in section 3.1.
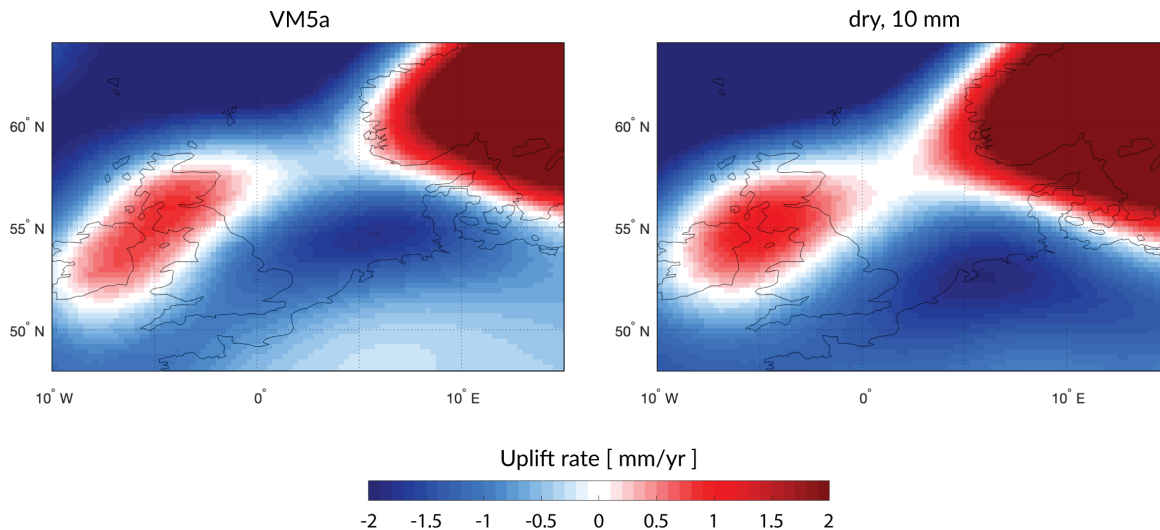

Figure 6.8: Uplift rates, using the Bradley2018 ice model in combination with various rheological configurations.

6.3. ICE-6G_C 3D rheologies

In this section, a selection of RSL curves and uplift rate maps obtained from GIA simulations of the ICE-6G_C model in combination with all four laterally varying composite rheologies are discussed.

As was determined in section 6.1, the ICE-6G_C is not the preferred ice model for Northwestern Europe in this research. However, it is of interest to assess whether the effects of the inclusion of different 3D composite rheologies are subject to change depending on the ice model used in simulation.

A first observation made from the majority of the RSL sites in figure 6.9 and the additional results in appendix B, is that site-specific trends in the near-field and mid-field can not be reproduced by altering the rheological configuration when using the ICE-6G_C model. As was discussed previously in this section, the RSL curve at site Orland is characterised by a period of relatively constant relative sea level, a steep decline between 12 and 10 ka BP, and a further gradual and constant decline until the present time. This could not be captured by the ICE-6G_C model in combination with the VM5a viscosity model. From figure 6.9, it can be concluded that varying the rheological configuration, does not improved the characteristic sudden decrease in RSL as captured by the observed SLIPs.

A similar observation can be made for the Stirling site. While the 10 mm dry rheology does lead to an improved fit of the SLIPs between 7 ka BP and present time, the trend of RSL fall between 12 and 10 ka PB cannot be reproduced by any of the rheological configurations. It is theorised that both the characteristic steep RSL decline, and the RSL fall-rise-fall, are primarily dependent on the deglaciation history. Based on the results in this study, it is thus recommended to use the Bradley2018 model for 3D GIA modelling in Northwestern Europe.

Referring back to section 6.1, it can be seen that the best RSL curve performance at far-field site Rotterdam is achieved by the 1D 6G model. This model configuration outperforms all other models using a 3D composite rheology. This supports the notion that the ICE-6G_C model in combination with its native viscosity model VM5a is best suited to accurately model far-field behaviour in Northwestern Europe.

Lastly, it can be seen that at the Solway Firth site, the GIA model using a wet 4 mm rheology yields a very good fit to RSL observations. However, it should be noted that the evident misfit in the uplift rate map in

figure 6.10 leads to believe that the W04 rheology is not suitable for global application in the 3D GIA FEM model. This uplift rate observation is in accordance with the observations discussed for the Bradley2018 model in section 6.2. Additionally, adopting a very weak rheology to correct for the possible shortcomings in the ICE-6G_C model for GIA modelling in Northwestern Europe, defeats the purpose of this research.
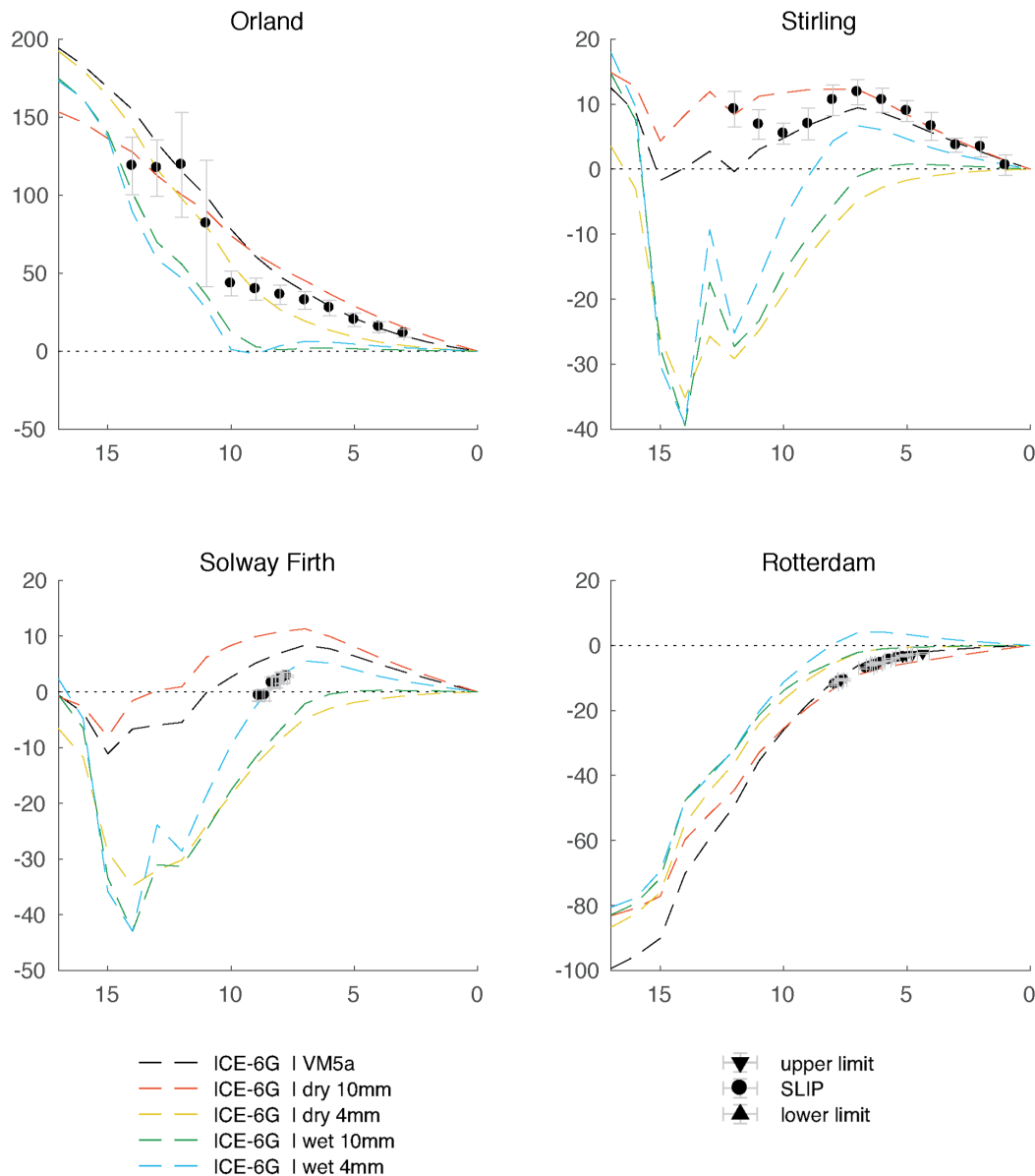
Figure 6.9: RSL curves and observations for a selection of sites, using the ICE-6G_C ice model in combination with various rheological configurations. Time in ka BP on the x-axis and RSL in meters on the y-axis.

6.3.1. Uplift rates

From the uplift rate maps included in figure 6.10, no significant new findings arise. Irrespective of the ice model used, the weaker rheologies introduce a severe deterioration of the fit to the GPS derived uplift rate observations. In agreement with earlier findings for the Bradley2018 model, only the dry, 4 mm rheology is able to reproduce the positive uplift rates for Scandinavia to some extent. The best performing 3D rheology in terms of uplift rate however remains the 10 mm dry rheology.
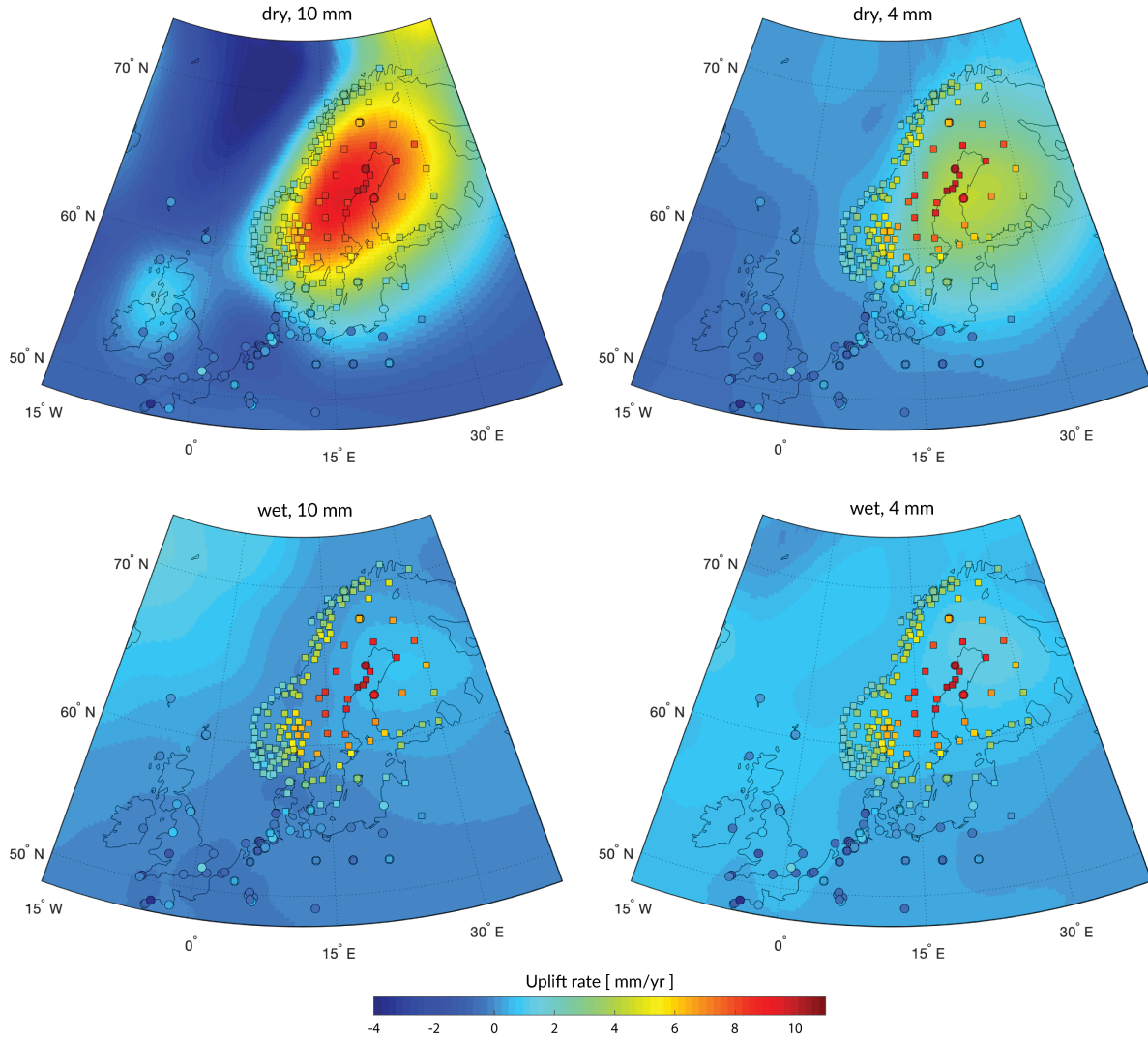
Figure 6.10: GPS derived vertical surface deformation and simulated uplift rate in Northwestern Europe, using the ICE-6G_C ice model in combination with various rheological configurations.

6.3.2. RSL change rates

This section mirrors section 6.2.3, in that a comparison is made between the RSL change rates for the ICE-6G_C model depicted in section 3.2.2 and the RSL change rates that are modelled using the 1D and 10 mm dry model configurations.

From the left frame in figure 6.11 it is concluded that the model output of the ICE-6G_C VM5a configuration in this research agrees very well with the corresponding frame in figure 3.5. It should be noted that while the ice and Earth model configuration originate from a single source, differences in FEM methodology as well as spatial and temporal resolution may exist. This gives rise to deviations between the two figures in terms of magnitude.

Reflecting on the analysis of the relative sea level change rate for the Bradley2018 models, the same applies here. With the introduction of the 10 mm dry rheology rather than the VM5a configuration, the centre of positive RSL change moves land-inward from the North Sea. At the northernmost coastlines of the Netherlands this yields an increase of the RSL change rate in the order of 0.4 mm per year. Additionally, the negative RSL change in Fennoscandia extends further into the surrounding seas. In the state-of-the-art sea level change projections for the Dutch Wadden Sea by Vermeersen et al. (2018), the GIA contribution to sea level change is derived from the ICE-5G VM2 model. The aforementioned sea level change projections for Den Helder and Delfzijl imply that GIA is the second largest contributor to local sea level change, with a cumulative contribu-

tion of 0.11 and 0.12 m respectively in the 21st century. Vermeersen et al. (2018) emphasises that the selection of GIA and solid Earth can impact such projections and recommends future usage of 3D nonlinear rheologies. The observations made from figure 6.11 support these conclusions.
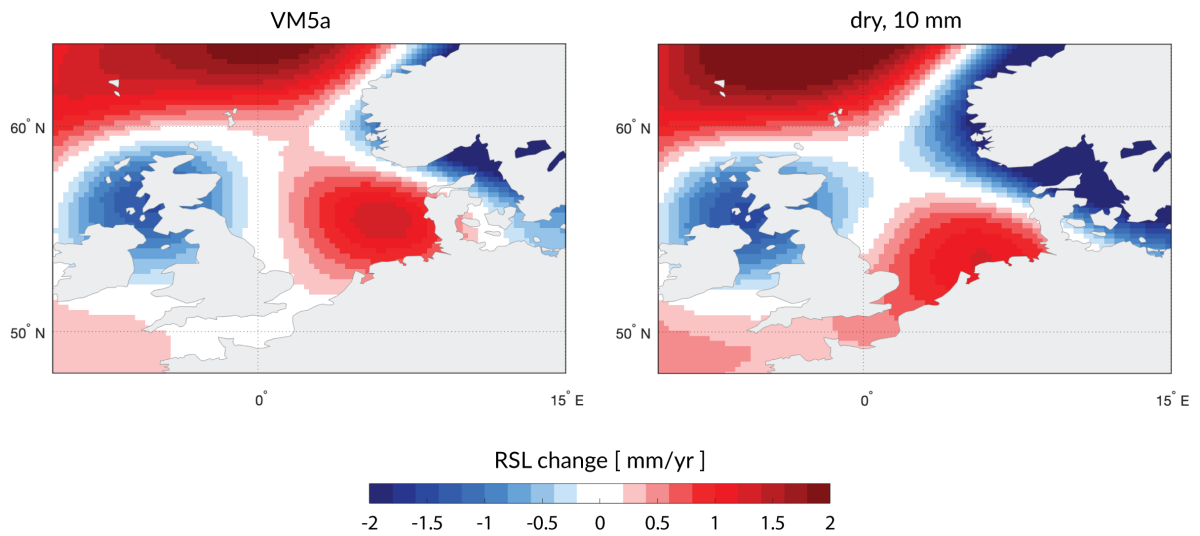
Figure 6.11: Relative sea level change rates, using the ICE-6G_C ice model in combination with various rheological configurations.

In parallel with section 6.2.3, figure 6.12 displays the uplift rates for two different rheological configurations included in figure 6.10 and 6.2. Again, an alternative projection and colour scale have been employed.
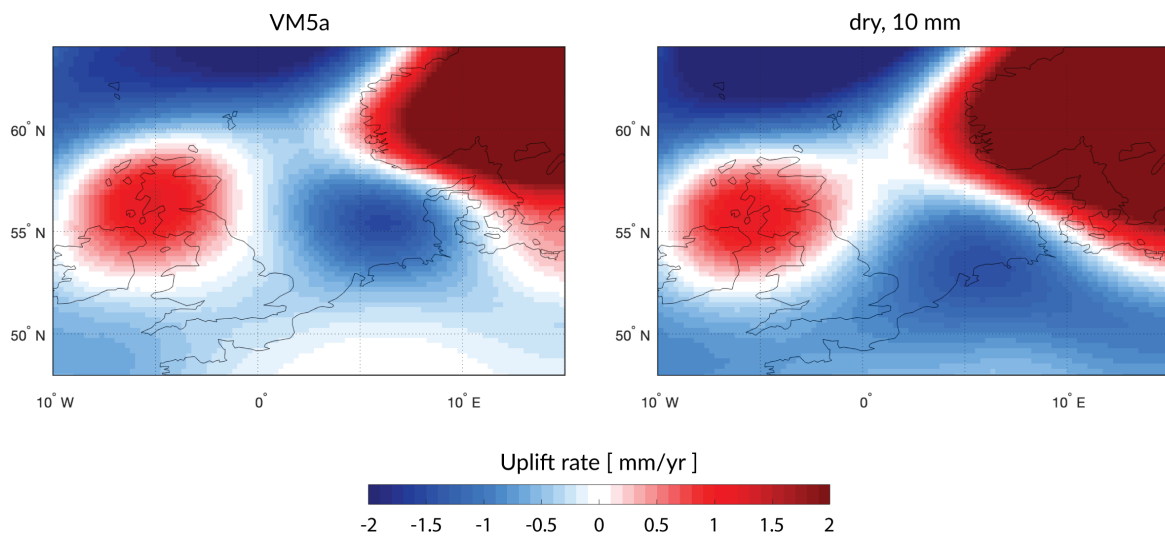

Figure 6.12: Uplift rates, using the ICE-6G_C ice model in combination with various rheological configurations.

7

Conclusion

In this chapter, the research questions defined in section 1.6 will be answered. These conclusions follow directly from the research methodology applied and the results obtained as discussed in the previous chapters.

To what extent does the GIA model performance improve upon the usage of a 3D composite rheology viscosity profile, rather than a radially symmetric viscosity profile?

In terms of uplift rate, it is concluded that the inclusion of a 3D composite rheology can yield an improved fit to observed uplift rates. This applies to areas in which GIA is deemed the dominant contributor to vertical surface deformation. Outside of these areas, no model combination could accurately reproduce the observed uplift and/or subsidence. This is attributed to the presence of other Earth deformation mechanisms that are not included in this research.

The uplift rates predicted by both the ICE-6G_C and Bradley2018 model in combination with the radially symmetric viscosity profile VM5a agree well with GPS derived observations. The fit to these observations can be improved by implementing a 10 mm grain size, dry composite rheology inferred from a three dimensional temperature model of the Earth's upper mantle. In doing so, the large lateral variation in mantle viscosity in Scandinavia is accounted for. This lateral transition results in a shift of the centre of uplift from the centre of the former ice sheet in the Gulf of Bothnia, to an area of lesser viscosity underneath Sweden. Not taking into account such a large lateral heterogeneity, could lead to an overestimation of ice sheet thickness in case a glacial model were to be developed based on uplift rates and a 1D viscosity distribution.

The incorporation of weaker composite rheologies, i.e. using either a higher water content and/or smaller grain size, was shown to significantly deteriorate the fit to the observed uplift rate. It is believed that the overall lower viscosities acquired using these rheological configurations, allow for more rapid relaxation. Hence, it is theorised that the ongoing uplift response which is simulated for a strong rheology at present time, may have already occurred at an earlier time and at a different magnitude.

In terms of relative sea level, it is concluded that an improvement of the GIA model performance can be achieved by adopting a 3D composite rheology at the majority of the RSL sites investigated. The exact improvement and the rheology with which this improvement is attained, are however regionally specific, as will be discussed later. Far-field RSL curves are less affected by the rheological configuration used, as here the eustatic sea level rise dominates the signal.

Additionally, it was determined that the extent to which an improved fit to RSL observations could be achieved, is dependent on the ice model used. It is concluded that the Bradley2018 ice model is preferred over the ICE-6G_C model for GIA modelling in Northwestern Europe. The former was found to more accurately represent characteristic observed RSL gradients and transitions between RSL rise and fall (and vice versa) than the ICE-6G_C model.

It was found that the inferior fit of the ICE-6G_C model to RSL observations in Northwestern Europe could not be overcome entirely by replacing the 1D viscosity distribution with a 3D composite rheology. This ICE-6G_C model is developed in conjunction with the 1D viscosity profile used in this research. Hence it is believed that due to the ICE-6G_C model being tuned to this VM5a viscosity profile and vice versa, the fit of

the ICE-6G_C model to RSL observations is already optimised for the 1D configuration used in this research. Additionally, further altering the rheological configuration of the overall model significantly beyond realistic values to compensate the limitations of the ICE-6G_C glacial history for regional GIA modelling, is not in line with the purpose of this research.

What 3D composite rheology GIA FEM model is best suited to model the vertical surface deformation of North-western Europe?

As was concluded before, out of the 5 different rheological configurations tested, only the radially symmetric and 10 mm dry 3D composite rheology configurations yield a good fit to observed uplift rates in previously glaciated regions. Additionally, a preference toward the Bradley2018 model has been expressed for GIA modelling in Northwestern Europe, based on the fit to RSL observations.

While no single rheological setting in combination with the Bradley2018 ice model yields the best performance in terms of RSL, the best fit to GPS observed uplift rates is attained by applying the 10 mm dry 3D composite rheology. Even though no large differences arise between the magnitude of the vertical deformation rates in formerly glaciated regions, it is believed that the 3D composite rheology better captures the total extent and perceived centre of uplift of areas that currently experience GIA induced vertical motion than the 1D model. This is derived mainly from the model performance in Scandinavia and Scotland, where GIA is believed to dominate vertical surface deformation rates.

The mismatch between the simulated and observed uplift rates outside of Ireland, Scotland, and Scandinavia, is attributed to the presence of other deformation processes in these areas. The uplift rate for coastal lowlands is however non-zero and should be accounted for in estimates of total surface deformation rates. This could lead to new insights for said other surface deformation processes. Additionally, it is concluded that the spatial distribution of negative uplift rates in the North Sea is sensitive to the rheological setting. Since this alters the pattern of uplift rate and its gradient across the Dutch coasts, it is important to account for these effects in future surface deformation and sea level change projections.

What can be inferred about the Earth's interior in Northwestern Europe from various rheological configurations of the GIA FEM model?

It was found that no conclusive evidence could be acquired to directly correlate the regionally preferred rheological configurations to the tectonic origin of these regions within Northwestern Europe. The most notable observations derived from RSL simulations lead to believe that dry rheologies prevail in the majority of the focus area. A preference towards a strong rheology was found for the mid-west of Scotland. While not fully substantiated in this study, it is believed that the water content in material dated to the Sveco-Norwegian orogen might be higher when compared to material of both earlier and later tectonic periods.

It is evident that the approach of using a selection of four different rheological configurations in combination with a 3D temperature model, allow for ambiguity in the assessment of a regionally preferred rheology. It is believed that this ambiguity could be minimised by testing for a more extensive range of grain size and water content, if possible including a 3D variability. This may enable the acquisition of a more comprehensive set of results from which a rheological distribution of Northwestern Europe can be inferred.

8
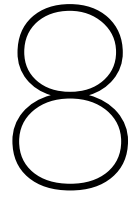
Recommendations

In this chapter a number of recommendations for future research are discussed. The majority of these recommendations follow directly from the execution of this research and the consequently obtained answers to the posed research questions. The recommendations are grouped based on their combined priority and significance.

It is advised to increase the variability of the three dimensional composite rheological configurations used in this research. This can be achieved through either of the following.

Firstly, it is suggested to expand on the range of configurations used in simulation in order to gain a more extensive insight into the effect of grain size and water content variation. In this research, two options for either variable have been selected. It is believed that these options yield a selection of relatively strong and relatively weak rheologies. It is recommended to also use Earth models in GIA simulations of Northwestern Europe and beyond, that can be qualified to be of moderate strength. This can be achieved by using a larger range of available grain sizes and water content in the development of the 3D Earth models. Most notably, it is recommended to investigate the effect of altering the water content throughout the range in between the two values used in both this and preceding research. Such an expansion of the parameter space may also call for the implementation of a quantitative analysis. The merit of a qualitative analysis to the interpretability of the results however remains.

Secondly, it is believed that the composite rheologies can be improved by varying both the grain size and water content in 3D. Such a model may be acquired by deriving a 3D model of these variables from analysis of surfaced mantle material and the tectonic history of the Earth, as well as from seismic and magnetic observations of the Earth's interior. Experimental research shows that water content in the mantle may be inferred from its electrical conductivity (Yoshino and Katsura, 2013). Additionally, a better understanding of grain size evolution may aid in the determination of laterally varying grain sizes (Dannberg et al., 2017). Accurate modelling of the composition of the Earth in terms of grain size and water content will lead to a better understanding of the properties and history of the interior of the Earth, as well as its effects on GIA.

Aside from the limited variation within the compositional parameters applied in this study, the use of a single single thermo-chemical model for the generation of the 3D viscosity distributions is a significant limitation of this research. While the WINTERC-3D model combines a variety of geophysical observations in order to generate a temperature distribution of the Earth's interior, it is uncertain to what extent compositional effects are accounted for. It is advised to investigate these uncertainties, and to assess whether the conclusions of this research hold for other thermal models as well.

Next, it is recommended to further investigate the effects of 3D composite rheologies on both present day and future projections of sea level change and surface deformation in coastal regions such as the Netherlands. This is driven by the observation that the spatial distribution of positive and negative uplift rates differs between the best performing 1D and 3D GIA FEM model respectively. Additionally, the selection of the best performing 3D GIA FEM model for Northwestern Europe is based on its fit to uplift rate observations in formerly glaciated areas. While it is assumed that the selected model also yields an accurate representation of GIA induced surface deformation outside of these regions, it is advised to attempt further validation in such areas where other surface deformation mechanisms may be more dominant. This could be achieved by

modelling the contribution of processes like compaction and tectonics, and assessing the cumulative fit of all modelled contributors to observed uplift rates.

Here, a few recommendations are provided which are believed to be easily implementable and of lesser priority than the aforementioned.

While the Bradley2018 model was selected as the preferred ice model for GIA modelling in Northwestern Europe, it was also found that the alternative ice model ICE-6G_C yields a better performance compared to the Bradley2018 model in far-field RSL observations. Hence it is recommended to combine the glacial history of Bradley2018 in the vicinity of Northwestern Europe, with the far-field ice sheets as captured by the ICE-6G_C model. It is believed that this may improve the fit of simulated RSL curves to observations made throughout Northwestern Europe in its entirety.

A further refinement of the simulated RSL curves may also be attained by updating the topographical model used in this research. This is expected to yield a more accurate representation of the coastlines of Northwestern Europe.

In this research, more than 20 time steps have been used to simulate the glaciation and deglaciation of Northwestern Europe between 122,000 years in the past and the present time. The number of time steps used is directly proportional to the computational cost of the simulation. While the total computational cost is regarded as high yet acceptable, redesigning the simulations or the 3D GIA FEM model itself to be less computationally expensive, would allow for an increase in either temporal or spatial resolution of the model. An increase in computational cost efficiency could be obtained by decreasing the total number of simulated time steps, or by enabling multi-processor usage for the Python processes executed outside of the Abaqus PDE. Note that the former may negatively affect the accuracy of the model, which should be tested for.

To conclude, some final recommendations are made that can be of help to further GIA research beyond the scope of this thesis. It is recommended to implement the effects of the Earth's rotation on both the deformation of the Earth as well as the distribution of water on its surface. This is expected to yield a more realistic and comprehensive GIA model. It should be assessed whether such rotational effects may be neglected in regional GIA studies. Additionally, given the flexibility of the 3D GIA FEM model regarding the regional focus are, the model allows for the study of GIA outside of Northwestern Europe, such as North America.

A
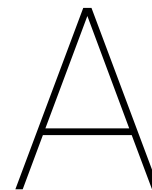
Filtering the Earth's elastic response

In this appendix, the implications of filtering the elastic response to changing sea level for the determination of uplift rate are discussed. The overall procedure followed to compute the uplift rate is described in section 4.5. Here, a brief discussion of whether or not this filtering should be applied is provided. This discussion is supported by an analysis of the exact impact of this filtering on the computed uplift rate.

A.1. Ambiguity of the elastic responses

In accordance with the principles of viscoelasticity, any change in loading of the surface of the Earth will yield both an instantaneous elastic response, and a long-term viscous response. In this research, the Earth is subjected to both oceanic and glacial loading. In order to compute the uplift rate, an additional time step has been added to the 3D GIA FEM simulations. At this future time, the ice load is identical to that at the present time. By default, the original 3D GIA FEM model by Blank (to be published), iteratively computes the total oceanic load as dictated by both the total change in ice volume, as well as the change in topography due to deformation of the Earth. This implies that while the ice loading of the surface between the present time and future time does not change, the oceanic loading does. This difference in oceanic loading across the future time step, induces an instantaneous elastic response. This elastic response can be filtered out, by actively applying the present time oceanic load, at both the present and future time in the Abaqus FEM model. This load application is performed both in model generation, and in model iteration where all oceanic surface loads are revised.

The deformation of the Earth can be attributed to both a glacial and oceanic component, which in turn both yield an elastic and a viscous response. Hence it is believed that by including the elastic response to GIA induced present day sea level change, the 3D GIA FEM model provides a realistic approximation of the viscoelastic behaviour of the Earth. On the other hand however, it is reasoned that including the present day elastic response introduces an ambiguity in the computed uplift rate. This is due to the fact that many other factors, such as tides, the oceanic temperature, periods of drought, or present day ice melt, could yield a similar elastic response at the present day. These processes are not accounted for in this study. It is not known what the contribution of such processes is to the computed uplift rate, and how they relate to the GIA induced elastic sea level response. Such ambiguity could be avoided by enabling the elastic response filter between the present time and future time used for uplift rate computations. Overall, it is debatable whether the GIA induced elastic response should be included in uplift rate computations. It is believed that such a decision is mostly dependent on the observable used to compare the computed uplift rates with. The filtering applied in the computations should match any filtering applied on the observations. In this study, GPS derived uplift rates are used. These uplift rate observations are believed to include both the viscous and elastic GIA induced present day surface deformation. While it is reasoned that neither enabling or disabling the elastic filter yields invalid results, it is beneficial to investigate the difference between two test cases in which the elastic filtering is either enabled or disabled.

A.2. Impact analysis of elastic filtering on uplift rate

In order to analyse the impact of elastic filtering on the uplift rate computations from the difference in uplift between a present time and a future time, the D10 BR test (refer to section 5.7 for an overview of this test

setup) has been performed twice. Whereas the one simulation allows a change in oceanic load between the present and future time, the other simulation does not allow for a change in oceanic load across the last time step. These simulations are denoted "incl. elastic" and "excl. elastic" respectively.

In figure A.1, the uplift rates that result from the two simulations using the 1D 6G setup are shown. Upon visual inspection of this figure, no differences between both simulations can be found. It can be concluded that in a general sense, both settings result in positive uplift rates at previously glaciated regions that agrees reasonably well with GPS derived vertical surface deformation rates.
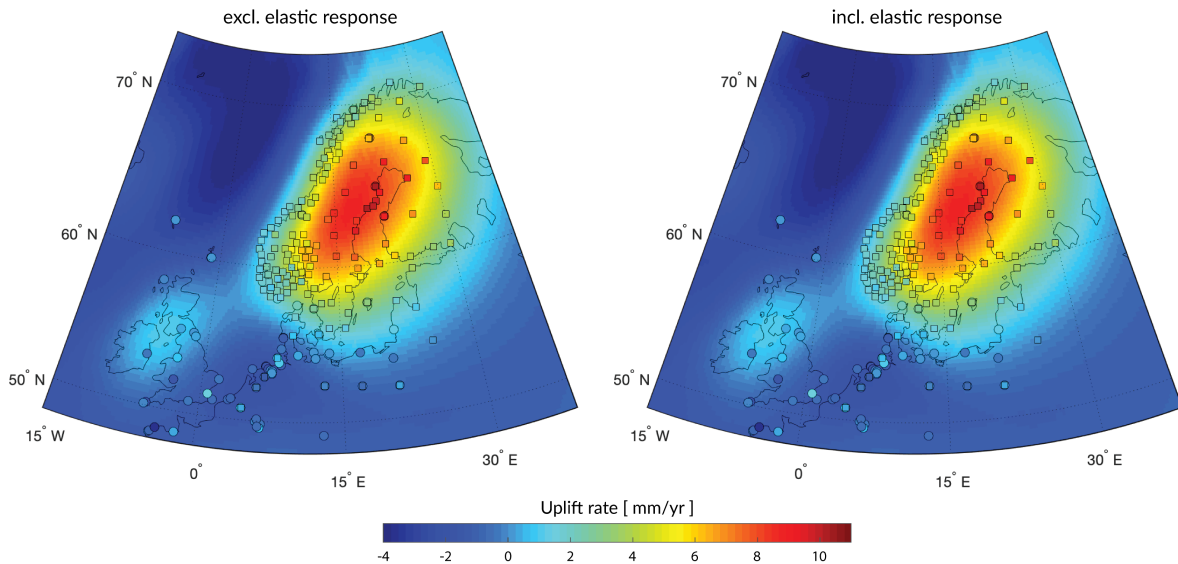

Figure A.1: Uplift rate excluding and including the elastic response to changing sea level in the last time step. Included are the observed uplift rates from the (circle) TIGA-WG and the (squares) BIFROST project as described in section 5.6.

A more interesting insight into the effect of elastic filtering can be discerned from figure A.2, in which the difference between the two uplift rate maps is plotted. This difference is obtained by subtracting the uplift rates that do not include the elastic sea level response, from those that do include this elastic response. It is evident that while the overall difference between the two solutions is marginal, it is most prevalent in oceanic regions. The simulation that allows for adjustment of the oceanic loading across the future time step yields a significantly higher uplift rate in the Gulf of Bothnia. It is theorised that present day uplift in Scandinavia results in draining of this body of water into the subsiding Norwegian Sea, which further promotes an increase in uplift over time. A similar explanation is valid for the difference in uplift observed in the Irish Sea and the part of the North Sea between Scotland and Norway. Here the difference is however smaller due to the lesser uplift rate with respect to Fennoscandia.

Also included in figure A.2 are the error associated with the TIGA-WG uplift rate observations as well as the standard deviation of the BIFROST uplift rate observations. It is observed that at the majority of the GPS stations, the associated error and standard deviation exceed the absolute difference between the uplift rates obtained from a model that includes and a model that excludes the elastic response to a changing sea level. While this is not true for a small selection of sites along the Gulf of Bothnia, it is concluded that the overall impact of either including or excluding the elastic response to sea level change in the uplift rate computations is very small. As such it is posed that the uplift rates may be computed without enabling the elastic filter, due to the marginal effect of the elastic response to sea level change over the 10 year future time interval.
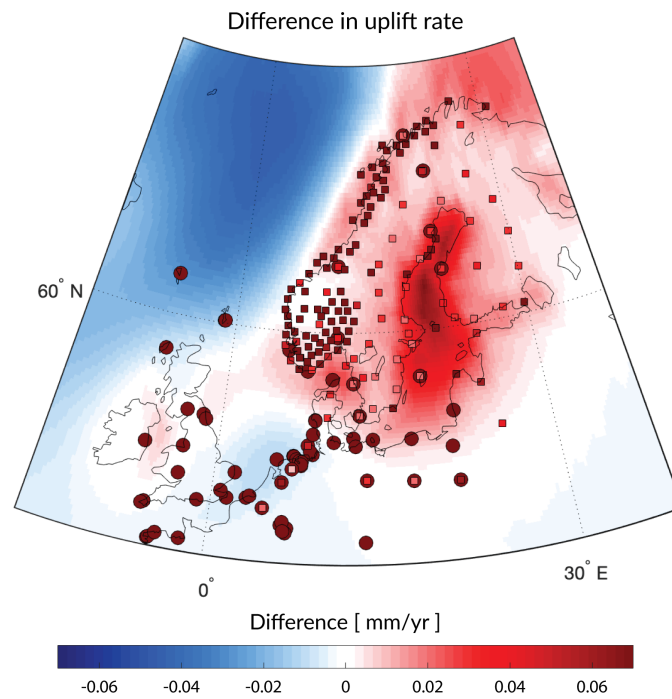
Figure A.2: Absolute difference between the uplift rates including and excluding the elastic response to changing sea level in the last time step. Included are the errors in the observed uplift rates from the (circle) TIGA-WG and the (squares) BIFROST project as described in section 5.6.

B

Additional results
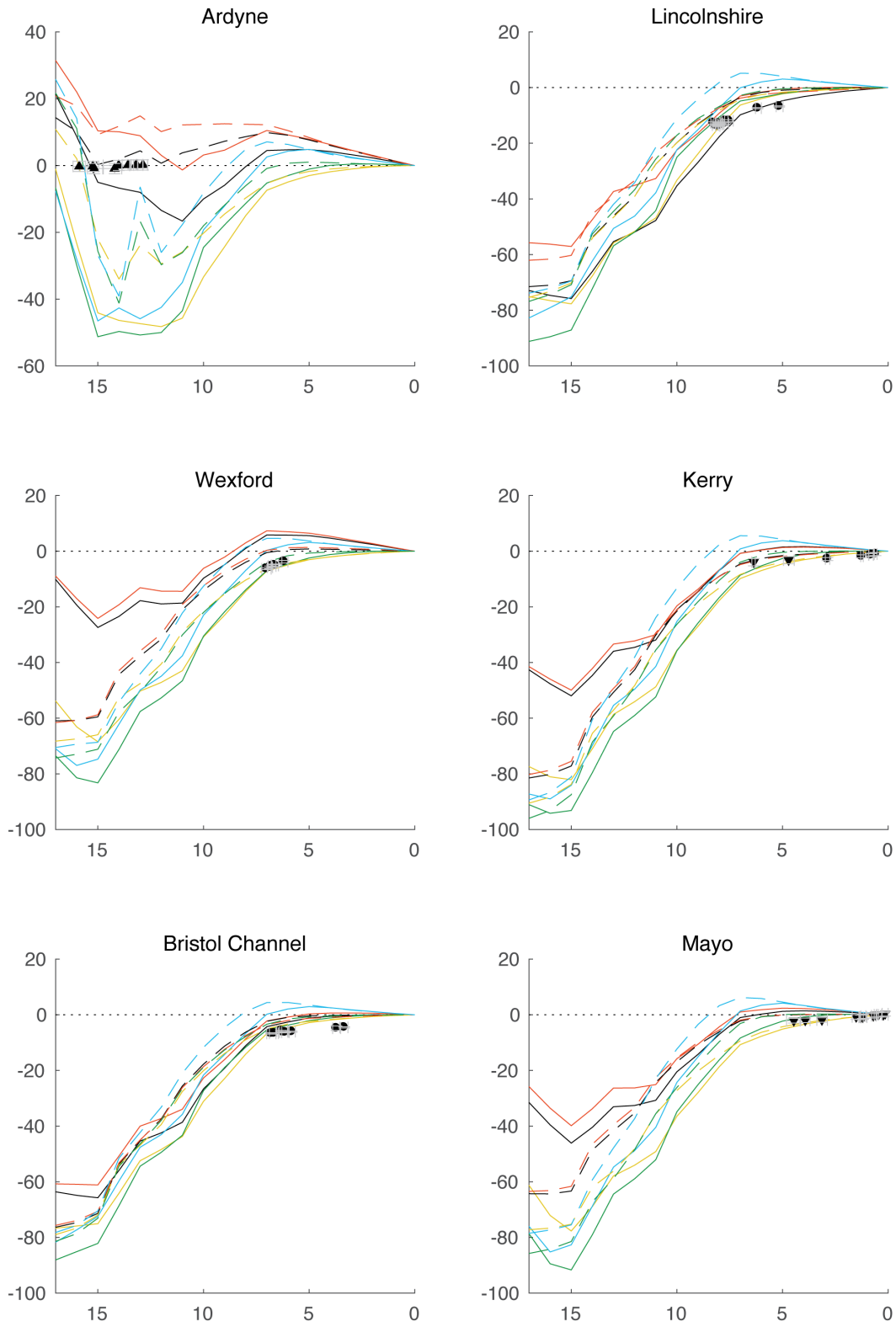
Figure B.1: RSL curves and observations for a selection of sites, for all model combinations. Time in ka BP on the x-axis and RSL in meters on the y-axis. Legend is included in figure B.4
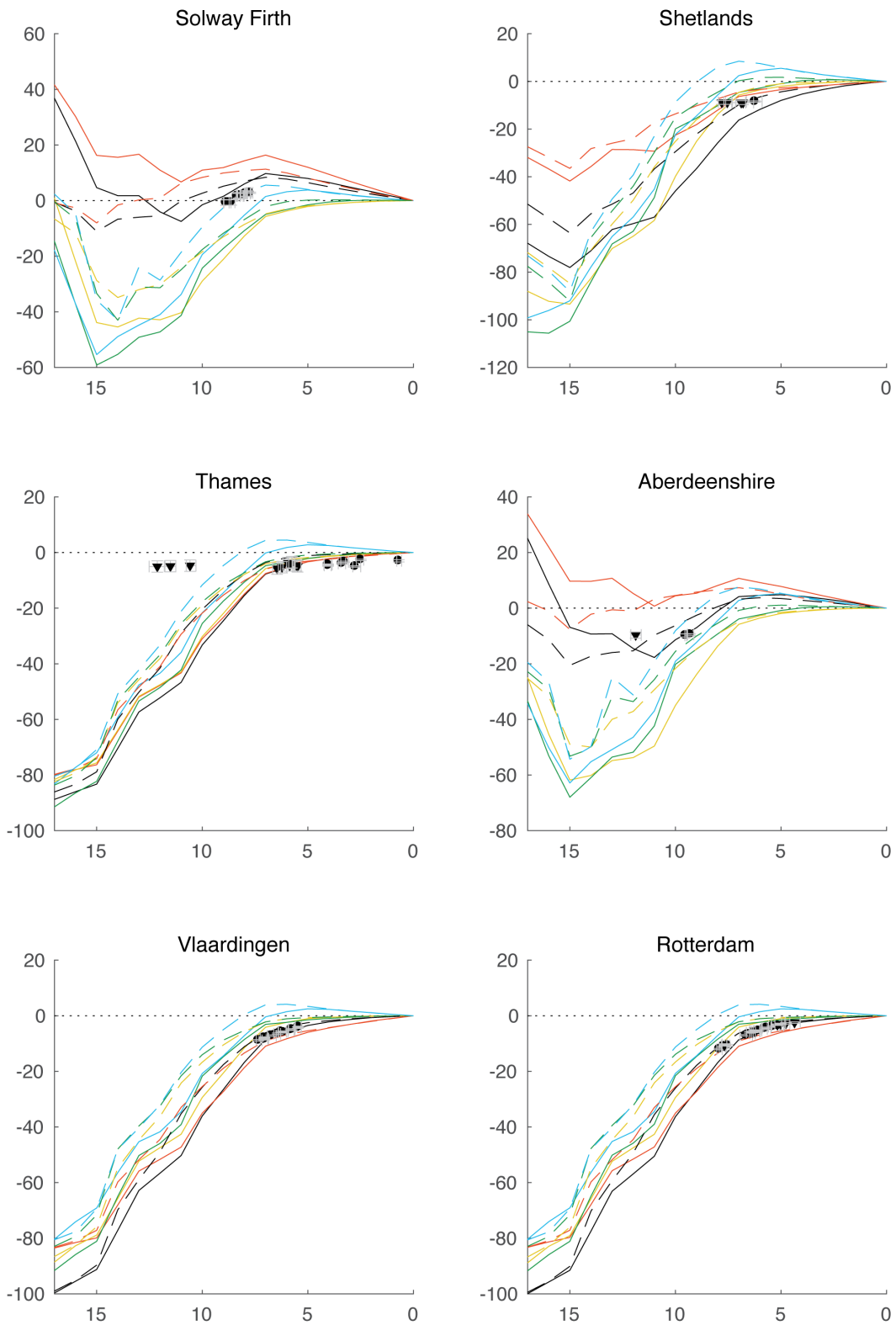
Figure B.2: RSL curves and observations for a selection of sites, for all model combinations. Time in ka BP on the x-axis and RSL in meters on the y-axis. Legend is included in figure B.4
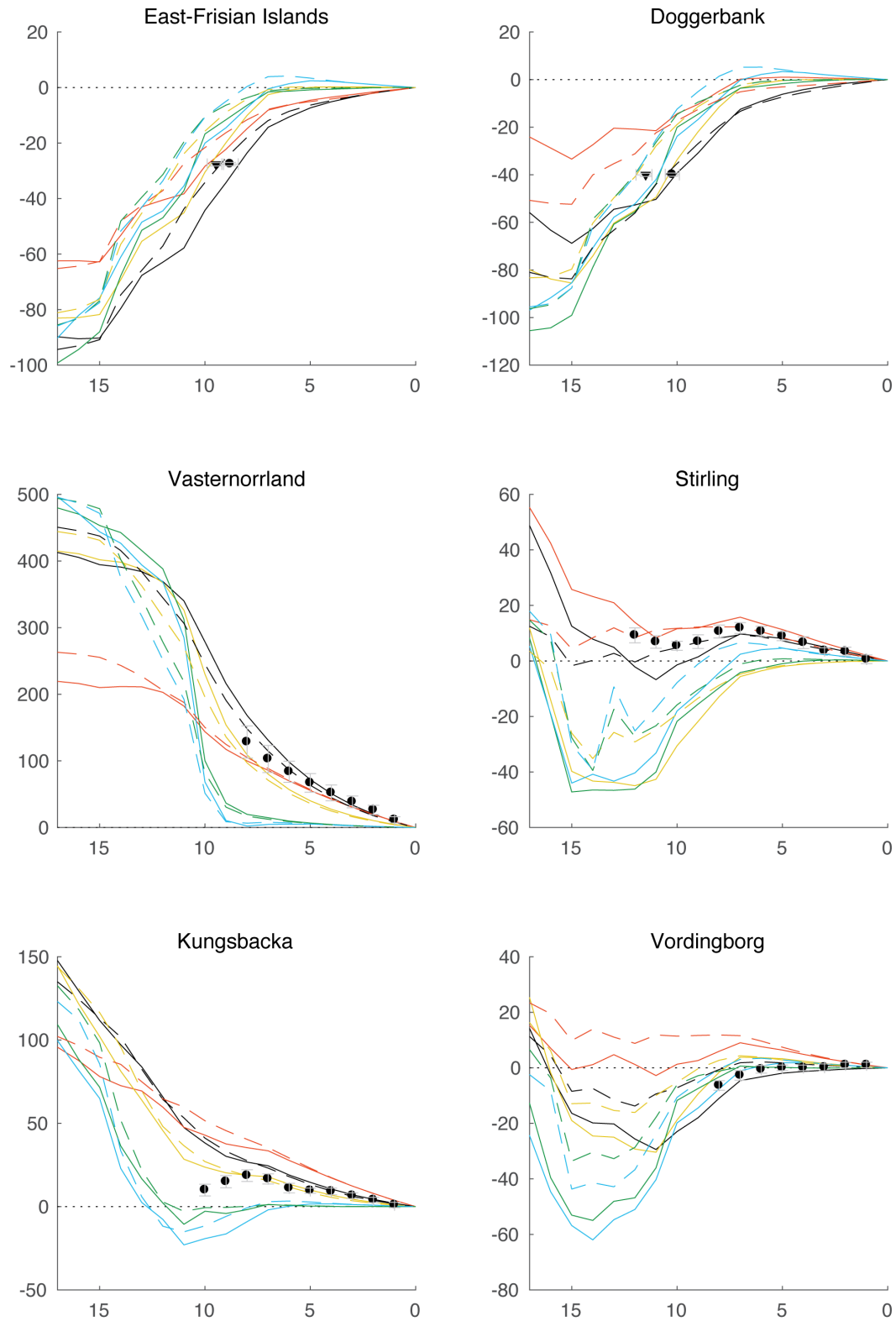
Figure B.3: RSL curves and observations for a selection of sites, for all model combinations. Time in ka BP on the x-axis and RSL in meters on the y-axis. Legend is included in figure B.4

Figure B.4: RSL curves and observations for a selection of sites, for all model combinations. Time in ka BP on the x-axis and RSL in meters on the y-axis.

Bibliography

Abaqus 3DS SIMULIA. Abaqus Analysis User's Guide 2016. `http://130.149.89.49:2080/v2016/books/usb/default.html`, July 2015a.

Abaqus 3DS SIMULIA. Abaqus User Subroutines Guide 2016. `http://130.149.89.49:2080/v2016/books/sub/default.html`, July 2015b.

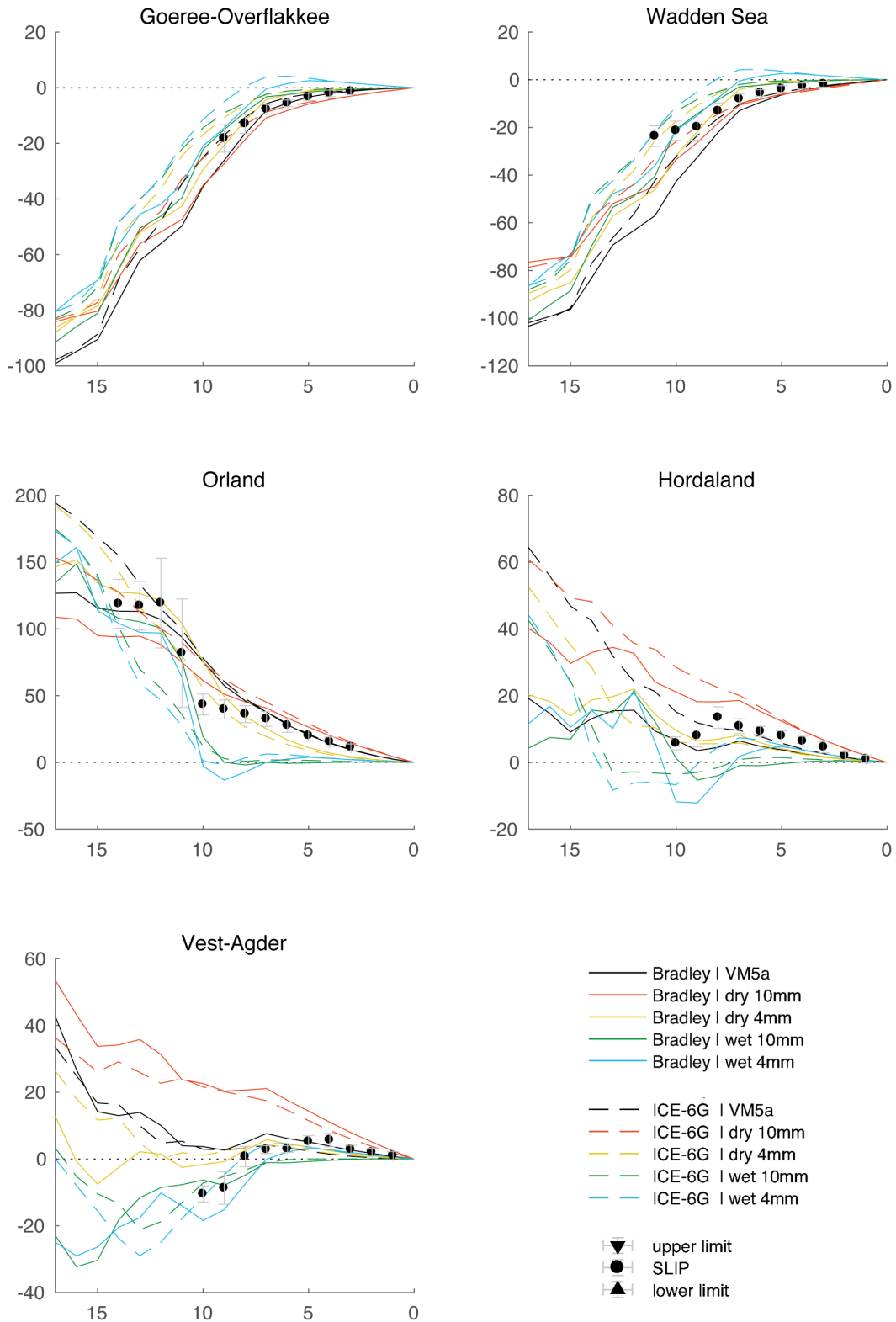Artemieva, I. M., Thybo, H., and Kaban, M. K. Deep Europe today: geophysical synthesis of the upper mantle structure and lithospheric processes over 3.5 Ga. *Geological Society, London, Memoirs*, 32(1):11–41, 2006. ISSN 0435-4052. doi: 10.1144/GSL.MEM.2006.032.01.02. URL `http://mem.lyellcollection.org/content/32/1/11`.

Barnes, H., Hutton, J., and Walters, K. *An Introduction to Rheology*. Elsevier Science & Technology, 1989. ISBN 9780080933696. URL `https://books.google.nl/books?id=VKj8BAAAQBAJ`.

Barnhoorn, A., van der Wal, W., Vermeersen, B. L. A., and Drury, M. R. Lateral, radial, and temporal variations in upper mantle viscosity and rheology under Scandinavia. *Geochemistry, Geophysics, Geosystems*, 12(1), 2011. doi: 10.1029/2010GC003290. URL `https://agupubs.onlinelibrary.wiley.com/doi/abs/10.1029/2010GC003290`.

Blank, B., van der Wal, W., Pappa, F., and Ebbing, J. A 3D Finite Element Model with Improved Spatial Resolution to Investigate the Effect of Varying Viscosity on Antarctica. *AGU Fall Meeting Abstracts*, Dec. 2017.

Bradley, S. L., Milne, G. A., Shennan, I., and Edwards, R. An improved glacial isostatic adjustment model for the british isles. *Journal of Quaternary Science*, 26(5):541–552, 2011. doi: 10.1002/jqs.1481. URL `https://onlinelibrary.wiley.com/doi/abs/10.1002/jqs.1481`.

Bradley, S. L., Ely, J., Clark, C., Edwards, R., Shennan, I., and Hindmarsh, R. C. A. Glacial Isostatic Adjustment of the British Isles and North West Europe. In *EGU General Assembly Conference Abstracts*, volume 20 of *EGU General Assembly Conference Abstracts*, page 9701, Apr. 2018.

Clark, C. D., Ely, J. C., Greenwood, S. L., Hughes, A. L. C., Meehan, R., Barr, I. D., Bateman, M. D., Bradwell, T., Doole, J., Evans, D. J. A., Jordan, C. J., Monteys, X., Pellicer, X. M., and Sheehy, M. Britice glacial map, version 2: a map and gis database of glacial landforms of the last british–irish ice sheet. *Boreas*, 47(1):11–e8, 2017. doi: 10.1111/bor.12273. URL `https://onlinelibrary.wiley.com/doi/abs/10.1111/bor.12273`.

Dannberg, J., Eilon, Z., Faul, U., Gassmöller, R., Moulik, P., and Myhill, R. The importance of grain size to mantle dynamics and seismological observations. *Geochemistry, Geophysics, Geosystems*, 18(8):3034–3061, 2017.

Dijkstra, A. H., Drury, M. R., and Frijhoff, R. M. Microstructures and lattice fabrics in the hilti mantle section (oman ophiolite): Evidence for shear localization and melt weakening in the crust–mantle transition zone? *Journal of Geophysical Research: Solid Earth*, 107(B11):ETG 2–1–ETG 2–18, 2002. doi: 10.1029/2001JB000458. URL `https://agupubs.onlinelibrary.wiley.com/doi/abs/10.1029/2001JB000458`.

Dixon, J. E., Dixon, T. H., Bell, D., and Malservisi, R. Lateral variation in upper mantle viscosity: role of water. *Earth and Planetary Science Letters*, 222(2):451–467, 2004.

Farrell, W. E. and Clark, J. A. On postglacial sea level. *Geophysical Journal of the Royal Astronomical Society*, 46(3):647–667, 1976. doi: 10.1111/j.1365-246X.1976.tb01252.x. URL `https://onlinelibrary.wiley.com/doi/abs/10.1111/j.1365-246X.1976.tb01252.x`.

Faul, U. H. and Jackson, I. The seismological signature of temperature and grain size variations in the upper mantle. *Earth and Planetary Science Letters*, 234(1-2):119–134, 2005.

Fokker, P. A., van Leijen, F. J., Orlic, B., van der Marel, H., and Hanssen, R. F. Subsidence in the dutch wadden sea. *Netherlands Journal of Geosciences*, 97(3):129–181, 2018.

Forno, G. D. and Gasperini, P. Modelling of mantle postglacial relaxation in axisymmetric geometry with a composite rheology and a glacial load interpolated by adjusted spherical harmonics analysis. *Geophysical Journal International*, 169(3):1301–1314, 2007. doi: 10.1111/j.1365-246X.2007.03347.x. URL `http://dx.doi.org/10.1111/j.1365-246X.2007.03347.x`.

Forno, G. D., Gasperini, P., and Boschi, E. Linear or nonlinear rheology in the mantle: a 3d finite-element approach to postglacial rebound modeling. *Journal of Geodynamics*, 39(2):183 – 195, 2005. ISSN 0264-3707. doi: https://doi.org/10.1016/j.jog.2004.08.008. URL `http://www.sciencedirect.com/science/article/pii/S0264370704001048`.

Fullea, J. WINTERC-3D. `https://sites.google.com/site/javierfullea/winterc-3d`, March 2019.

Gasperini, P., Dal Forno, G., and Boschi, E. Linear or non-linear rheology in the earth's mantle: the prevalence of power-law creep in the postglacial isostatic readjustment of laurentia. *Geophysical Journal International*, 157(3):1297–1302, 2004.

Gordon, R. B. Diffusion creep in the earth's mantle. *Journal of Geophysical Research*, 70(10):2413–2418, 1965. doi: 10.1029/JZ070i010p02413. URL `https://agupubs.onlinelibrary.wiley.com/doi/abs/10.1029/JZ070i010p02413`.

Grinsted, A., Jevrejeva, S., Riva, R., and Dahl-Jensen, D. Sea level rise projections for Northern Europe under RCP8.5. *Climate Research*, 64(1):15–23, 2015. ISSN 0936-577X. doi: 10.3354/cr01309.

Han, D. and Wahr, J. The viscoelastic relaxation of a realistically stratified earth, and a further analysis of postglacial rebound. *Geophysical Journal International*, 120(2):287–311, 1995. doi: 10.1111/j.1365-246X.1995.tb01819.x. URL `http://dx.doi.org/10.1111/j.1365-246X.1995.tb01819.x`.

Hawkesworth, C., Dhuime, B., Pietranik, A., Cawood, P., Kemp, A., and Storey, C. The generation and evolution of the continental crust. *Journal of the Geological Society*, 167(2):229–248, 2010. ISSN 0016-7649. doi: 10.1144/0016-76492009-072. URL `http://jgs.lyellcollection.org/content/167/2/229`.

Hijma, M., Engelhart, S. E., Törnqvist, T. E., Horton, B. P., Hu, P., and Hill, D. F. A protocol for a geological sea-level database. *Handbook of Sea-Level Research, edited by: Shennan, I., Long, AJ, and Horton, BP, Wiley Blackwell*, pages 536–553, 2015.

Hijma, M. P. and Cohen, K. M. Holocene sea-level database for the rhine-meuse delta, the netherlands: Implications for the pre-8.2 ka sea-level jump. *Quaternary Science Reviews*, 214:68 – 86, 2019. ISSN 0277-3791. doi: https://doi.org/10.1016/j.quascirev.2019.05.001. URL `http://www.sciencedirect.com/science/article/pii/S0277379117310156`.

Hirth, G. and Kohlstedt, D. Rheology of the upper mantle and the mantle wedge: A view from the experimentalists. *Washington DC American Geophysical Union Geophysical Monograph Series*, 138:83–105, 2003. doi: 10.1029/138GM06.

Hirth, G. and Kohlstedt, D. L. Water in the oceanic upper mantle: implications for rheology, melt extraction and the evolution of the lithosphere. *Earth and Planetary Science Letters*, 144(1-2):93–108, 1996.

Hughes, A. L. C., Gyllencreutz, R., Lohne, Ø. S., Mangerud, J., and Svendsen, J. I. The last eurasian ice sheets – a chronological database and time-slice reconstruction, dated-1. *Boreas*, 45(1):1–45, 2015. doi: 10.1111/bor.12142. URL `https://onlinelibrary.wiley.com/doi/abs/10.1111/bor.12142`.

Hunegnaw, A., Teferle, F. N., Bingley, R. M., and Hansen, D. N. Status of tiga activities at the british isles continuous gnss facility and the university of luxembourg. In Rizos, C. and Willis, P., editors, *IAG 150 Years*, pages 617–623, Cham, 2016. Springer International Publishing. ISBN 978-3-319-30895-1.

Hunegnaw, A., Teferle, F. N., Ebuy Abraha, K., Santamaría-Gómez, A., Gravelle, M., Wöppelman, G., Schöne, T., Deng, Z., Bingley, R., Hansen, D. N., Sanchez, L., Moore, M., and Jia, M. A New Global Vertical Land Movement Data Set from the TIGA Combined Solution. In *EGU General Assembly Conference Abstracts*, volume 19 of *EGU General Assembly Conference Abstracts*, page 18947, Apr. 2017.

International GNSS Service. Chronology of IGS Reference Frame Usage. `http://acc.igs.org/igs-frames.html`, October 2012. Accessed on 02/07/2019.

Ivins, E. R. and Sammis, C. G. On lateral viscosity contrast in the mantle and the rheology of low-frequency geodynamics. *Geophysical Journal International*, 123(2):305–322, 1995. doi: 10.1111/j.1365-246X.1995.tb06856.x. URL `http://dx.doi.org/10.1111/j.1365-246X.1995.tb06856.x`.

Karato, S. *Deformation of Earth Materials: An Introduction to the Rheology of Solid Earth*. Cambridge University Press, 2012. ISBN 9781139469562. URL `https://books.google.nl/books?id=rZC7osgnyyYC`.

Karato, S.-i. and Wu, P. Rheology of the upper mantle: A synthesis. *Science*, 260(5109):771–778, 1993. ISSN 0036-8075. doi: 10.1126/science.260.5109.771. URL `http://science.sciencemag.org/content/260/5109/771`.

Karato, S.-I., Paterson, M. S., and FitzGerald, J. D. Rheology of synthetic olivine aggregates: influence of grain size and water. *Journal of Geophysical Research: Solid Earth*, 91(B8):8151–8176, 1986.

Kaufmann, G. and Wu, P. Lateral asthenospheric viscosity variations and postglacial rebound: A case study for the barents sea. *Geophysical Research Letters*, 25(11):1963–1966, 1998. doi: 10.1029/98GL51505. URL `https://agupubs.onlinelibrary.wiley.com/doi/abs/10.1029/98GL51505`.

Kaufmann, G., Wu, P., and Wolf, D. Some effects of lateral heterogeneities in the upper mantle on postglacial land uplift close to continental margins. *Geophysical Journal International*, 128(1):175–187, 1997. doi: 10.1111/j.1365-246X.1997.tb04078.x. URL `https://onlinelibrary.wiley.com/doi/abs/10.1111/j.1365-246X.1997.tb04078.x`.

Kaufmann, G., Wu, P., and Li, G. Glacial isostatic adjustment in fennoscandia for a laterally heterogeneous earth. *Geophysical Journal International*, 143(1):262–273, 2000. doi: 10.1046/j.1365-246x.2000.00247.x. URL `http://dx.doi.org/10.1046/j.1365-246x.2000.00247.x`.

Kendall, R. A., Mitrovica, J. X., and Milne, G. A. On post-glacial sea level – ii. numerical formulation and comparative results on spherically symmetric models. *Geophysical Journal International*, 161(3):679–706, 2005. doi: 10.1111/j.1365-246X.2005.02553.x. URL `https://onlinelibrary.wiley.com/doi/abs/10.1111/j.1365-246X.2005.02553.x`.

Kierulf, H. P., Steffen, H., Simpson, M. J. R., Lidberg, M., Wu, P., and Wang, H. A gps velocity field for fennoscandia and a consistent comparison to glacial isostatic adjustment models. *Journal of Geophysical Research: Solid Earth*, 119(8):6613–6629, 2014. doi: 10.1002/2013JB010889. URL `https://agupubs.onlinelibrary.wiley.com/doi/abs/10.1002/2013JB010889`.

Kious, W. and Tilling, R. *This Dynamic Earth: The Story of Plate Tectonics*. U.S. Geological Survey, 1996. ISBN 9780788133183. URL `https://books.google.nl/books?id=T5mZVQeigpMC`.

Klemann, V. and Martinec, Z. Contribution of glacial-isostatic adjustment to the geocenter motion. *Tectonophysics*, 511(3):99 – 108, 2011. ISSN 0040-1951. doi: https://doi.org/10.1016/j.tecto.2009.08.031. URL `http://www.sciencedirect.com/science/article/pii/S0040195109004855`. Special Section on Observation and Modeling of Glacial Isostatic Adjustment.

Lambeck, K., Smither, C., and Johnston, P. Sea-level change, glacial rebound and mantle viscosity for northern europe. *Geophysical Journal International*, 134(1):102–144, 1998. doi: 10.1046/j.1365-246x.1998.00541.x. URL `http://dx.doi.org/10.1046/j.1365-246x.1998.00541.x`.

Le Brocq, A. M., Payne, A. J., and Vieli, A. An improved antarctic dataset for high resolution numerical ice sheet models (albmap v1). *Earth System Science Data*, 2(2):247–260, 2010. doi: 10.5194/essd-2-247-2010. URL `https://www.earth-syst-sci-data.net/2/247/2010/`.

Lidberg, M., Johansson, J. M., Scherneck, H.-G., and Milne, G. A. Recent results based on continuous gps observations of the gia process in fennoscandia from bifrost. *Journal of Geodynamics*, 50(1):8 – 18, 2010. ISSN 0264-3707. doi: https://doi.org/10.1016/j.jog.2009.11.010. URL `http://www.sciencedirect.com/science/article/pii/S0264370709001665`. Upper Mantle Dynamics and Quaternary Climate in Cratonic Areas (DynaQlim) mdash; Understanding the Glacial Isostatic Adjustment.

Malvern, L. E. *Introduction to the Mechanics of a Continuous Medium*. Number Monograph. 1969.

Mangerud, J., Gyllencreutz, R., Lohne, Ø., and Svendsen, J. I. Glacial history of norway. In *Developments in Quaternary Sciences*, volume 15, pages 279–298. Elsevier, 2011.

Martinec, Z. and Wolf, D. Inverting the Fennoscandian relaxation-time spectrum in terms of an axisymmetric viscosity distribution with a lithospheric root. *Journal of Geodynamics*, 39(2):143 – 163, 2005. ISSN 0264-3707. doi: https://doi.org/10.1016/j.jog.2004.08.007. URL `http://www.sciencedirect.com/science/article/pii/S0264370704001024`.

Maslin, M. In retrospect: Forty years of linking orbits to ice ages. *Nature*, 540(7632):208, 2016.

McDonough, W. and s. Sun, S. The composition of the earth. *Chemical Geology*, 120(3):223 – 253, 1995. ISSN 0009-2541. doi: https://doi.org/10.1016/0009-2541(94)00140-4. URL `http://www.sciencedirect.com/science/article/pii/0009254194001404`. Chemical Evolution of the Mantle.

Meissner, R. and Kern, H. *Earth's Structure, Continental Crust*, pages 138–144. Springer Netherlands, Dordrecht, 2011. ISBN 978-90-481-8702-7. doi: 10.1007/978-90-481-8702-7_30. URL `https://doi.org/10.1007/978-90-481-8702-7_30`.

Milne, G. A. and Mitrovica, J. X. Postglacial sea-level change on a rotating Earth. *Geophysical Journal International*, 133(1):1–19, 04 1998. ISSN 0956-540X. doi: 10.1046/j.1365-246X.1998.1331455.x. URL `https://doi.org/10.1046/j.1365-246X.1998.1331455.x`.

Mitrovica, J. and Forte, A. Radial profile of mantle viscosity: Results from the joint inversion of convection and postglacial rebound observables. *Journal of Geophysical Research: Solid Earth*, 102(B2):2751–2769, 1997. doi: 10.1029/96JB03175. URL `https://agupubs.onlinelibrary.wiley.com/doi/abs/10.1029/96JB03175`.

Mitrovica, J. X. Recent controversies in predicting post-glacial sea-level change. *Quaternary Science Reviews*, 22(2):127 – 133, 2003. ISSN 0277-3791. doi: https://doi.org/10.1016/S0277-3791(02)00225-1. URL `http://www.sciencedirect.com/science/article/pii/S0277379102002251`.

Mitrovica, J. X., Milne, G. A., and Davis, J. L. Glacial isostatic adjustment on a rotating earth. *Geophysical Journal International*, 147(3):562–578, 12 2001. ISSN 0956-540X. doi: 10.1046/j.1365-246x.2001.01550.x. URL `https://doi.org/10.1046/j.1365-246x.2001.01550.x`.

Montagner, J.-P. *Earth's Structure, Global*, pages 144–154. Springer Netherlands, Dordrecht, 2011. ISBN 978-90-481-8702-7. doi: 10.1007/978-90-481-8702-7_13. URL `https://doi.org/10.1007/978-90-481-8702-7_13`.

National Geophysical Data Center, NOAA. 2-minute Gridded Global Relief Data (ETOPO2) v2, 2006. `https://www.ngdc.noaa.gov/mgg/global/etopo2.html`, June 2006. Accessed on 17/05/2019.

Nita, B., Maurya, S., and Montagner, J.-P. Anisotropic tomography of the European lithospheric structure from surface wave studies. *Geochemistry, Geophysics, Geosystems*, 17(6):2015–2033, 2016.

Paulson, A. *Interference of the Earth's Mantle Viscosiyt from Post-glacial Rebound*. PhD thesis, 2006.

Paulson, A., Zhong, S., and Wahr, J. Modelling post-glacial rebound with lateral viscosity variations. *Geophysical Journal International*, 163(1):357–371, 2005. doi: 10.1111/j.1365-246X.2005.02645.x. URL `http://dx.doi.org/10.1111/j.1365-246X.2005.02645.x`.

Peltier, W. The impulse response of a maxwell earth. *Reviews of Geophysics*, 12(4):649–669, Nov 1974.

Peltier, W. R., Argus, D. F., and Drummond, R. Space geodesy constrains ice age terminal deglaciation: The global ice-6g_c (vm5a) model. *Journal of Geophysical Research: Solid Earth*, 120(1):450–487, 2015. doi: 10.1002/2014JB011176. URL `https://agupubs.onlinelibrary.wiley.com/doi/abs/10.1002/2014JB011176`.

Plant, J., Whittaker, A., Demetriades, A., De Vivo, B., and Lexa, J. The geological and tectonic framework of europe. *Geochemical Atlas of Europe. Part*, 1, 2003.

Prodehl, C., Kennett, B., Artemieva, I. M., and Thybo, H. 100 years of seismic research on the Moho. *Tectonophysics*, 609:9 – 44, 2013. ISSN 0040-1951. doi: https://doi.org/10.1016/j.tecto.2013.05.036. URL `http://www.sciencedirect.com/science/article/pii/S0040195113003508`. Moho: 100 years after Andrija Mohorovicic.

Ranalli, G. *Rheology of the Earth.* Springer Science & Business Media, 1995.

Renner, J., Evans, B., and Hirth, G. On the rheologically critical melt fraction. *Earth and Planetary Science Letters*, 181(4):585 – 594, 2000. ISSN 0012-821X. doi: https://doi.org/10.1016/S0012-821X(00)00222-3. URL `http://www.sciencedirect.com/science/article/pii/S0012821X00002223`.

Ritsema, J., van Heijst, H. J., and Woodhouse, J. H. Global transition zone tomography. *Journal of Geophysical Research: Solid Earth*, 109(B2), 2004. doi: 10.1029/2003JB002610. URL `https://agupubs.onlinelibrary.wiley.com/doi/abs/10.1029/2003JB002610`.

Ritsema, J., Deuss, A., van Heijst, H. J., and Woodhouse, J. H. S40rts: a degree-40 shear-velocity model for the mantle from new rayleigh wave dispersion, teleseismic traveltime and normal-mode splitting function measurements. *Geophysical Journal International*, 184(3):1223–1236, 2011. doi: 10.1111/j.1365-246X.2010.04884.x. URL `http://dx.doi.org/10.1111/j.1365-246X.2010.04884.x`.

Roy, K. *High-quality constraints on the glacial isostatic adjustment process over North America: The ICE-7G_-NA (VM7) model.* PhD thesis, 2017.

Roy, K. and Peltier, W. Glacial isostatic adjustment, relative sea level history and mantle viscosity: reconciling relative sea level model predictions for the U.S. East coast with geological constraints. *Geophysical Journal International*, 201(2):1156–1181, 2015. doi: 10.1093/gji/ggv066. URL `+http://dx.doi.org/10.1093/gji/ggv066`.

Roy, K. and Peltier, W. Space-geodetic and water level gauge constraints on continental uplift and tilting over North America: regional convergence of the ICE-6G_C (VM5a/VM6) models. *Geophysical Journal International*, 210(2):1115–1142, 2017. doi: 10.1093/gji/ggx156. URL `http://dx.doi.org/10.1093/gji/ggx156`.

Roy, K. and Peltier, W. Relative sea level in the Western Mediterranean basin: A regional test of the ICE-7G_NA (VM7) model and a constraint on late Holocene Antarctic deglaciation. *Quaternary Science Reviews*, 183: 76–87, 2018.

Rychert, C. A. and Shearer, P. M. A global view of the lithosphere-asthenosphere boundary. *Science*, 324(5926): 495–498, 2009. ISSN 0036-8075. doi: 10.1126/science.1169754. URL `http://science.sciencemag.org/content/324/5926/495`.

Shennan, I., Bradley, S. L., and Edwards, R. Relative sea-level changes and crustal movements in britain and ireland since the last glacial maximum. *Quaternary Science Reviews*, 188:143 – 159, 2018. ISSN 0277-3791. doi: https://doi.org/10.1016/j.quascirev.2018.03.031. URL `http://www.sciencedirect.com/science/article/pii/S0277379118300040`.

Steffen, H. and Kaufmann, G. Glacial isostatic adjustment of Scandinavia and northwestern Europe and the radial viscosity structure of the Earth's mantle. *Geophysical Journal International*, 163(2):801–812, 2005. doi: 10.1111/j.1365-246X.2005.02740.x. URL `http://dx.doi.org/10.1111/j.1365-246X.2005.02740.x`.

Steffen, H. and Wu, P. Glacial isostatic adjustment in fennoscandia—a review of data and modeling. *Journal of Geodynamics*, 52(3):169 – 204, 2011. ISSN 0264-3707. doi: https://doi.org/10.1016/j.jog.2011.03.002. URL `http://www.sciencedirect.com/science/article/pii/S0264370711000445`.

Steffen, H., Kaufmann, G., and Wu, P. Three-dimensional finite-element modeling of the glacial isostatic adjustment in fennoscandia. *Earth and Planetary Science Letters*, 250(1):358 – 375, 2006. ISSN 0012-821X. doi: https://doi.org/10.1016/j.epsl.2006.08.003. URL `http://www.sciencedirect.com/science/article/pii/S0012821X06005747`.

Trampert, J., Vacher, P., and Vlaar, N. Sensitivies of seismic velocities to temperature, pressure and composition in the lower mantle. *Physics of the Earth and Planetary Interiors*, 124(3-4):255–267, 2001.

Tushingham, A. and Peltier, W. Ice-3g: A new global model of late pleistocene deglaciation based upon geo-
physical predictions of post-glacial relative sea level change. *Journal of Geophysical Research: Solid Earth*,
96(B3):4497–4523, 1991. doi: 10.1029/90JB01583. URL `https://agupubs.onlinelibrary.wiley.com/
doi/abs/10.1029/90JB01583`.

Tushingham, A. M. and Peltier, W. Validation of the ICE-3G Model of Würm-Wisconsin Deglaciation using a
global data base of relative sea level histories. *Journal of Geophysical Research: Solid Earth*, 97(B3):3285–
3304, 1992.

van der Wal, W. Contributions of space gravimetry to postglacial rebound modeling with different rheologies.
Doktora Tezi, University of Calgary, Department of Geomatics Engineering, Calgary, Alberta, 2009.

van der Wal, W., Wu, P., Wang, H., and Sideris, M. G. Sea levels and uplift rate from composite rheology in
glacial isostatic adjustment modeling. *Journal of Geodynamics*, 50(1):38 – 48, 2010. ISSN 0264-3707. doi:
https://doi.org/10.1016/j.jog.2010.01.006. URL `http://www.sciencedirect.com/science/article/
pii/S0264370710000190`.

van der Wal, W., Kurtenbach, E., Kusche, J., and Vermeersen, B. Radial and tangential gravity rates from
grace in areas of glacial isostatic adjustment. *Geophysical Journal International*, 187(2):797–812, 2011. doi:
10.1111/j.1365-246X.2011.05206.x. URL `http://dx.doi.org/10.1111/j.1365-246X.2011.05206.x`.

van der Wal, W., Barnhoorn, A., Stocchi, P., Gradmann, S., Wu, P., Drury, M., and Vermeersen, B. Glacial iso-
static adjustment model with composite 3-d earth rheology for fennoscandia. *Geophysical Journal Inter-
national*, 194(1):61–77, 2013. doi: 10.1093/gji/ggt099. URL `http://dx.doi.org/10.1093/gji/ggt099`.

van der Wal, W., Whitehouse, P. L., and Schrama, E. J. Effect of GIA models with 3D composite mantle viscosity
on GRACE mass balance estimates for Antarctica. *Earth and Planetary Science Letters*, 414:134 – 143, 2015.
ISSN 0012-821X. doi: https://doi.org/10.1016/j.epsl.2015.01.001. URL `http://www.sciencedirect.
com/science/article/pii/S0012821X15000059`.

Vermeersen, B. L., Slangen, A. B., Gerkema, T., Baart, F., Cohen, K. M., Dangendorf, S., Duran-Matute, M.,
Frederikse, T., Grinsted, A., Hijma, M. P., and et al. Sea-level change in the dutch wadden sea. *Netherlands
Journal of Geosciences*, 97(3):79–127, 2018. doi: 10.1017/njg.2018.7.

Vink, A., Steffen, H., Reinhardt, L., and Kaufmann, G. Holocene relative sea-level change, isostatic subsidence
and the radial viscosity structure of the mantle of northwest europe (belgium, the netherlands, germany,
southern north sea). *Quaternary Science Reviews*, 26(25):3249 – 3275, 2007. ISSN 0277-3791. doi: https:
//doi.org/10.1016/j.quascirev.2007.07.014. URL `http://www.sciencedirect.com/science/article/
pii/S0277379107002053`.

Wang, H. and Wu, P. Effects of lateral variations in lithospheric thickness and mantle viscosity on glacially
induced relative sea levels and long wavelength gravity field in a spherical, self-gravitating Maxwell
Earth. *Earth and Planetary Science Letters*, 249(3):368 – 383, 2006. ISSN 0012-821X. doi: https:
//doi.org/10.1016/j.epsl.2006.07.011. URL `http://www.sciencedirect.com/science/article/pii/
S0012821X06005024`.

Weerdesteijn, M. The implementation of glaciation-induced rotational behavior of the Earth in a numerical
model. Master's thesis, 2019.

Whitehouse, P. Glacial isostatic adjustment and sea-level change. *State of the art report. Svensk Kärnbränsle-
hantering AB, Swedish Nuclear Fuel and Waste Management Co., Stockholm*, page 105, 2009.

Whitehouse, P., Latychev, K., Milne, G. A., Mitrovica, J. X., and Kendall, R. Impact of 3-d earth structure
on fennoscandian glacial isostatic adjustment: Implications for space-geodetic estimates of present-day
crustal deformations. *Geophysical Research Letters*, 33(13), 2006. doi: 10.1029/2006GL026568. URL `https:
//agupubs.onlinelibrary.wiley.com/doi/abs/10.1029/2006GL026568`.

Whitehouse, P. L. Glacial isostatic adjustment modelling: historical perspectives, recent advances, and future
directions. *Earth Surface Dynamics*, 6(2):401–429, 2018.

Whitehouse, P. L., Bentley, M. J., Milne, G. A., King, M. A., and Thomas, I. D. A new glacial isostatic adjustment model for antarctica: calibrated and tested using observations of relative sea-level change and present-day uplift rates. *Geophysical Journal International*, 190(3):1464–1482, 9 2012. ISSN 1365-246X. doi: 10.1111/j.1365-246X.2012.05557.x. URL `https://doi.org/10.1111/j.1365-246X.2012.05557.x`.

W.R. Peltier. Paleo-topographic datasets. `https://www.atmosp.physics.utoronto.ca/~peltier/data.php`, October 2018. Accessed on 18/05/2019.

Wu, P. Modelling postglacial sea levels with power-law rheology and a realistic ice model in the absence of ambient tectonic stress. *Geophysical Journal International*, 139(3):691–702, 12 1999. ISSN 0956-540X. doi: 10.1046/j.1365-246x.1999.00965.x. URL `https://doi.org/10.1046/j.1365-246x.1999.00965.x`.

Wu, P. Using commercial finite element packages for the study of earth deformations, sea levels and the state of stress. *Geophysical Journal International*, 158(2):401–408, 2004. doi: 10.1111/j.1365-246X.2004.02338.x. URL `http://dx.doi.org/10.1111/j.1365-246X.2004.02338.x`.

Wu, P. and Peltier, W. R. Viscous gravitational relaxation. *Geophysical Journal of the Royal Astronomical Society*, 70(2):435–485, Aug 1982. doi: 10.1111/j.1365-246X.1982.tb04976.x. URL `https://onlinelibrary.wiley.com/doi/abs/10.1111/j.1365-246X.1982.tb04976.x`.

Wu, P. and Peltier, W. R. Pleistocene deglaciation and the Earth's rotation: a new analysis. *Geophysical Journal International*, 76(3):753–791, 03 1984. ISSN 0956-540X. doi: 10.1111/j.1365-246X.1984.tb01920.x. URL `https://doi.org/10.1111/j.1365-246X.1984.tb01920.x`.

Wu, P. and van der Wal, W. Postglacial sealevels on a spherical, self-gravitating viscoelastic earth: effects of lateral viscosity variations in the upper mantle on the inference of viscosity contrasts in the lower mantle. *Earth and Planetary Science Letters*, 211(1):57 – 68, 2003. ISSN 0012-821X. doi: https://doi.org/10.1016/S0012-821X(03)00199-7. URL `http://www.sciencedirect.com/science/article/pii/S0012821X03001997`.

Wu, P. and Wang, H. Postglacial isostatic adjustment in a self-gravitating spherical earth with power-law rheology. *Journal of Geodynamics*, 46(3):118 – 130, 2008. ISSN 0264-3707. doi: https://doi.org/10.1016/j.jog.2008.03.008. URL `http://www.sciencedirect.com/science/article/pii/S0264370708000239`. Glacial Isostatic Adjustment: New Developments and Applications in Global Change, Hydrology, Sea Level, Cryosphere, and Geodynamics.

Wu, X., Collilieux, X., Altamimi, Z., Vermeersen, B. L. A., Gross, R. S., and Fukumori, I. Accuracy of the international terrestrial reference frame origin and earth expansion. *Geophysical Research Letters*, 38(13), 2011. doi: 10.1029/2011GL047450. URL `https://agupubs.onlinelibrary.wiley.com/doi/abs/10.1029/2011GL047450`.

Yoshino, T. and Katsura, T. Electrical conductivity of mantle minerals: Role of water in conductivity anomalies. *Annual Review of Earth and Planetary Sciences*, 41(1):605–628, 2013. doi: 10.1146/annurev-earth-050212-124022. URL `https://doi.org/10.1146/annurev-earth-050212-124022`.

Zhu, H., Bozdağ, E., and Tromp, J. Seismic structure of the european upper mantle based on adjoint tomography. *Geophysical Journal International*, 201(1):18–52, 2015. doi: 10.1093/gji/ggu492. URL `http://dx.doi.org/10.1093/gji/ggu492`.